UNIVERSITY OF TECHNOLOGY SYDNEY
Faculty of Engineering and Information Technology

Gearshift Analysis for an Electric Vehicle with a Novel Synchronizer Mechanism

by

Wenwei Mo

A Thesis Submitted
in Partial Fulfillment of the
Requirements for the Degree

Doctor of Philosophy

Sydney, Australia

2020

Certificate of Authorship/Originality

I, Wenwei Mo, certify that the work in this thesis has not previously been submitted for a degree nor has it been submitted as part of requirements for a degree except as fully acknowledged within the text.

I also certify that the thesis has been written by me. Any help that I have received in my research work and the preparation of the thesis itself has been acknowledged. In addition, I certify that all information sources and literature used are indicated in the thesis. This research is supported by the Australian Government Research Training Program.

Production Note:
Signature of Student: Signature removed prior to publication.

Date: 23 July 2020

Acknowledgements

Firstly, I would like to take this opportunity to express my sincere gratitude to my principal supervisor Professor Nong Zhang and co-supervisor Dr. Paul Walker, for their patience, continuous support, constructive suggestions, immense knowledge and invaluable experience.

I would also like to thank my colleagues: Dr. Mohamed Awadallah, Dr. Yuhong Fang, Dr. Jinglai Wu, Dr. Haitao Yang, Dr. Jiejunyi Liang, Dr. Jiageng Ruan, Yang Tian, Boyi Xiao, Shengxiong Sun, Shilei Zhou, and all other friends at the School of Mechanical and Mechatronic Engineering, and Yujiao Wu at the School of Biomedical Engineering and Lang Chen at the School of Electrical and Data Engineering in UTS, and workshop managers, Mr. Laurence Stonard, and Mr. Chris Chapman, for their support and assistance.

I am also grateful to Professor Deyuan Li and Professor Xiong Liu, for their help, support and suggestions.

My sincere thanks also go to my parents, elder sister, and younger brother, for their encouragement and financial support.

Last but not least, I would like to acknowledge the financial support for this project, provided jointly by the University of Technology Sydney (UTS) and the China Scholarship Council (CSC).

Wenwei Mo

Sydney, Australia, 2020.

List of Publications

A proportion of Chapters 1 to 2 and a substantial proportion of Chapters 3 to 6 including Appendix A and C have been published as journal papers in Mechanical Systems and Signal Processing and Mechanism and Machine Theory.

Journals

1. **Wenwei Mo**, Paul D. Walker, Yuhong Fang, Jinglai Wu, Jiageng Ruan, and Nong Zhang, “A novel shift control concept for multi-speed electric vehicles”, *Mechanical Systems and Signal Processing*, 112 (2018):171-193. DOI: https://doi.org/10.1016/j.ymssp.2018.04.017

2. **Wenwei Mo**, Paul D. Walker, and Nong Zhang,“Dynamic analysis and control for an electric vehicle with harpoon-shift synchronizer”, *Mechanism and Machine Theory*, 133 (2019): 750-766. DOI: https://doi.org/10.1016/j.mechmachtheory.2018.11.018.

3. Yang Tian, Haitao Yang, **Wenwei Mo**, Shilei Zhou, Nong Zhang, and Paul D. Walker, “Optimal coordinating gearshift control of a two-speed transmission for battery electric vehicles”, *Mechanical Systems and Signal Processing*, 136 (2020): 106521. DOI: https://doi.org/10.1016/j.ymssp.2019.106521

4. **Wenwei Mo**, Jinglai Wu, Paul D. Walker, and Nong Zhang, “Shift characteristics of a bilateral Harpoon-shift synchronizer for electric vehicles equipped with CLAMT”, *Mechanical Systems and Signal Processing*, accepted.

Conference Proceedings

1. **Wenwei Mo**, Paul D. Walker, and Nong Zhang, “Dynamics of Dry-Clutch Engagement for Powertrain Systems with AMTs”, *Proceeding: 2017 International Conference on Advanced VehiclePowertrains (ICAVP’ 2017).*

Contents

List of Figures

List of Tables

Abbreviation

MT	Manual transmission
AT	Automatic transmission
AMT	Automated manual transmission
CVT	Continuously variable transmission
DCT	Dual clutch transmission
CLAMT	Clutchless automated manual transmission
EV	Electric vehicle
MSEV	Multispeed electric vehicle
EM	Electric motor
ICE	Internal combustion engine
ECU	Electronic control unit
TCU	Transmission control unit
PSC	Power sharing control
UST	Uninterrupted shift transmission
MCS	Multi-mode controllable shifter
COWC	Controllable one-way clutch
ACL	Assist clutch
PMP	Pontryagin's minimum principle
DOF	Degree of freedom

DAC	Digital to analog converter
ADC	Analog to digital converter
DI	Digital input
DO	Digital output
PC	Personal computer
LCD	Liquid-crystal display

Notations

T_m	Motor output torque
T_{gin}	Torque of gearbox input shaft
T_{slout}	Torque of gearbox output shaft
T_{dout}	Differential drive torque
T_{hv}	Torque transmitted by the tire to vehicle
T_{load}	Load torque
T_{rg}	Torque transmitted by the torque springs
T_{pre}	Torque due to spring pre-compression
T_{sg}	Collision torque between sleeve and dog gear
T_{sr}	Collision torque between sleeve and guide ring
F_t	Tangential force acting on the chamfer surface
F_a	Axial shifting force acting on the sleeve
F'	Reaction force
J_m	Motor inertia
J_{dout}	Equivalent inertia of final drive
J_h	Equivalent inertia of Wheel hubs
J_v	Equivalent inertia of vehicle and tires
J'_s	Equivalent inertia of sleeve and sleeve hub
J'_{gin}	Equivalent inertia of input shaft

J'_{r_i}	Guide ring inertia of i-th gear
m_v	Vehicle mass
m_s	Sleeve mass
γ_1	The 1^{st} gear ratio
γ_2	The 2^{nd} gear ratio
γ_3	The 3^{rd} gear ratio
γ_d	Final ratio
r_w	tire radius
N	The number of sleeve prongs
k_1	Equivalent stiffness of gearbox input shaft
k_2	Equivalent stiffness of gearbox output shaft
k_3	Equivalent stiffness of half shafts
k_4	Equivalent stiffness of tires
k_{sg}	Equivalent stiffness of collision between sleeve and dog gear
k_{sr}	Equivalent stiffness of collision between sleeve and guide ring
c_1	Damping 1
c_2	Damping 2
c_3	Damping 3
c_4	tire damping
c_m	Viscous damping
c_t	Viscous damping
c_{x_i}	Viscous damping ($i = 1, 2, 3$)
c_{sg}	Equivalent damping of collision between sleeve and dog gear

c_{sr}	Equivalent damping of collision between sleeve and guide ring
c_{rg}	Viscous damping
n	Nonlinear exponent factor
μ_s	Chamfer friction
μ'_s	Chamfer friction
μ_{sg}	Dynamic friction
θ	Angular displacement
$\dot{\theta}$	Angular velocity
$\ddot{\theta}$	Angular acceleration
x_s	Axial displacement of sleeve
$\dot{x_s}$	Axial velocity of sleeve
x_{max}	Maximum displacement
D	Variable
S_i	Variable $(i = 1, ..., 4)$
$\varDelta L$	Design parameter
θ_i	Design parameter $(i = 1, ..., 5)$
θ'	Design parameter
θ_{clr}	Parameter $(\theta_{clr} = \theta_1 - 2\theta')$
$\mathcal{L}$	Gear change signal
T_s	Torque
L_{bar}	Length of bar
G	Weight
θ_{bar}	Turning angular displacement of the bar due to the weight

q_{sg}	Relative penetration depth between sleeve and dog gear
q_{sr}	Relative penetration depth between sleeve and guide ring
$\dot{q}_{sg}$	Relative normal contact speed between sleeve and dog gear
$\dot{q}_{sr}$	Relative normal contact speed between sleeve and guide ring
R_{out}	Outside radius of the guide ring and dog gear
R_m	Mean contact radius between sleeve and guide ring tooth chamfer
β	Chamfer angle of bilateral Harpoon shift
β_1	Chamfer angle of the guide block of unilateral Harpoon shift
β_2	Chamfer angle of the external groove of unilateral Harpoon shift
$\varDelta x$	Distance from guide ring's tooth tip to a certain point on its chamfer
$\varDelta x_2$	Distance from dog gear's tooth tip to a certain point on its chamfer

Abstract

Multi-speed clutchless automated manual transmission (CLAMT) can offer many benefits for electric vehicles (EVs). It improves the driving efficiency and transmission performance compared to single-speed EVs. Currently, most multi-speed transmissions use conventional cone-type synchronizers for speed synchronization. However, these friction elements are a major source of inefficiency in multi-ratio gearboxes. Friction losses and heat dissipation can significantly influence transmission performance. In addition, frictional wear has a considerable impact on the service life and shifting performance of traditional synchronizers.

To overcome these drawbacks, the concept of unilateral Harpoon-shift synchronizer is introduced in the study. It aims to improve the gearboxes' efficiency and riding comfort, meanwhile, simplify the shift control logic for EVs with the multi-gear transmissions. A detailed dynamic model of the unilateral Harpoon shift is built to study the engaging performance of the proposed synchronizer. Besides, to investigate the powertrain transients, an original dynamic model of the CLAMT power-train system which integrates the Harpoon shift model is developed in the study. Also, to guarantee a smooth gear change, torque and speed profiles are designed using a modified step function for the torque control and active speed synchronization of the electric motor (EM) in EVs. Up- and down-shift simulation results verify the effectiveness of the proposed models as well as control logic.

Furthermore, to reduce the jerk during gear shifts, the Harpoon-shift torque spring stiffness in each gear is optimized via quantitative analysis. Also, the impacts of rotating inertia and speed difference on the vehicle jerks are quantitatively investigated. In addition, an experiment is conducted to study the engaging performance of the unilateral Harpoon shift and prove the effectiveness of the dynamic models.

To improve the performance of the unilateral Harpoon shift, a new concept of bilateral Harpoon shift is proposed for the multi-speed EVs equipped with CLAMTs. Then a detailed and original multi-body model of the bilateral Harpoon shift is established, aiming to capture the synchronizer's transient behavior during the engagement. In the model, the engaging process is defined as six stages, and it can cover the interacting cases between the engaging-related parts, including guide ring, sleeve, and dog gear. Then the model is integrated into the established model of the powertrain system to analyze the gearshift vibrations, allowing to investigate the engaging performance of the bilateral Harpoon shift based on the shifting shocks. Based on the integrated model, gearshift simulations are conducted and the impacts of the torque spring stiffness and tooth chamfer angle on the shifting shocks are comprehensively analyzed, and the two significant parameters are then optimized. Furthermore, comparisons are performed to demonstrate the superiority of the proposed torque profile over its counterpart based on the modified bump function. Results show that the proposed Harpoon shift can achieve high-quality gear change for EVs and meanwhile overcome the friction-related drawbacks of traditional synchronizers. Besides, the Harpoon shift greatly simplifies the shift control strategy due to its special engaging mechanism.

Chapter 1

Introduction

The application of multi-speed transmissions in electric vehicles (EVs) continues to grow as a result of improved performance and driving efficiency in comparison to single speed EVs [1–3]. Traditionally, shifting and gear selection is performed with the use of friction clutches, a result of both limited controllability and high inertia of combustion engines. These friction elements are a major source of inefficiency in multi-speed gearboxes [4–6]. As electric motors are significantly more controllable than their conventional counterparts, as evidenced by paper such as [7–9], reliance on inefficient friction elements can be reduced, and even eliminated. This has resulted in the development of shift control strategies that rely on motor control rather than friction based strategies [10–12]. However, as shown in [13] these strategies cannot entirely eliminate the need for torsional vibration absorption during clutch lockup.

As established by a number of comprehensive studies on integral control of multi-speed electric vehicle (MSEV) platforms [8, 14–16], and in particular those with clutchless automated manual transmissions (CLAMT) [8, 14, 17, 18], the need for friction clutches for speed synchronization in EV shift control is reducing. Whilst these are still necessary for AT [15] and DCT [16] based platforms, CLAMTs can, in theory, achieve functional control without the use of friction clutches [7, 9].

To minimize losses, the design of synchronization mechanisms is critical in applications substantially affected by system efficiency, i.e. electric vehicles [19]. Energy in an open synchroniser clutch is consumed as viscous drag. In papers such as [4, 5] it is demonstrated to have a significant impact on powertrain operating efficiency. This is undesirable for multi-speed electric vehicle platforms that need to minimize any power losses [20]. The use of dog clutches alone, however, has limitations with "clash" type failures that occur when there is a high relative speed during engagement [1, 6, 21, 22].

This thesis presents the concept of a novel Harpoon-shift synchronizer mechanism for EVs equipped with multi-gear CLAMT, aiming to improve shifting quality and efficiency. Meanwhile, it overcomes some of the biggest issues of conventional counterparts, including friction losses and wear. The knowledge contributions of the thesis lie in the following aspects:

(1) Modeling of two types of Harpoon-shift synchronizer, i.e., unilateral and bilateral Harpoon shift.

(2) Modeling and shift control of an EV powertrain system equipped with multi-gear CLAMTs, which integrates the model of Harpoon shift.

(3) Physical testing is conducted to study the engaging transient response of the synchronizer.

(4) Quantitative analysis of the impacts of key parameters on the engaging performance of Harpoon shift.

1.1 Project Statement

Detailed dynamic models of unilateral and bilateral Harpoon shift synchronizers are developed and integrated into a model of an EV multi-speed CLAMT powertrain system to investigate its shifting transient characteristics. In addition, an experiment is set up to estimate the synchronizer engaging performance.

1.2 Project Objectives

1. Dynamic modeling of two types of Harpoon-shift synchronizer, including unilateral and bilateral Harpoon shift.
2. Experiment to study the shift characteristics and verify the effectiveness of Harpoon-shift model.
3. Dynamic modeling of an EV multi-speed CLAMT powertrain system with an integrated model of Harpoon shift.
4. Gear shift control design for EVs equipped with multi-speed CLAMTs to improve the shifting quality.
5. Investigating the effects of rotating inertia and speed difference on the shifting quality.
6. Analyzing the impacts of the chamfer angle and torque spring of Harpoon-shift synchronizer on the shifting shocks.

1.3 Project Scope

1. Dynamic modeling of multi-speed CLAMT equipped powertrain and Harpoon-shift synchronizer based on multi-body dynamics.

2. Numerical simulations to investigate the shift transient characteristics of Harpoon shift.

3. Experiment for the evaluation of Harpoon shift engaging performance.

1.4 Outline of This Thesis

This thesis is structured as follows:

Chapter 2

Background information regarding the electric vehicles as well as the subsystems of the powertrain system, including friction clutch, transmissions, and synchronizer, are introduced in the chapter. Then, a comprehensive literature investigation about the dynamic modeling of the powertrain system and synchronizer mechanism, shifting control strategy is conducted. Both the merits and disadvantages of the research are discussed briefly.

Chapter 3

The shortcomings of traditional cone-clutch synchronizers are identified in this chapter. In order to overcome the issues of the conventional synchronizer, the concept of unilateral Harpoon-shift synchronizer is introduced. Then, the configuration and working principle of the unilateral Harpoon shift are thoroughly illustrated, to emphasizes its advantages over the traditional counterparts.

Chapter 4

In this chapter, a detailed and original dynamic model of unilateral Harpoon-shift synchronizer is established to study its transient behavior during the engagement. Besides, a power-train model of an EV equipped with three-speed CLAMTs is developed, which integrates the Harpoon-shift model. Through this integrated powertrain model, the subsystem influence of the synchronizer mechanism on the whole system transient characteristics during gear shift can be figured out.

Chapter 5

A gearshift strategy for a multi-speed CLAMT of EV is developed in this chapter. The torque profiles for motor torque reduction and restoration phases and the speed profile for the phase of motor active speed synchronization are designed based on a modified step function, to guarantee a smooth gear shift.

Chapter 6

On the basis of the unilateral Harpoon-shift synchronizer model and the EV multi-speed CLAMT equipped powertrain model developed in Chapter 4 and the shifting control strategies proposed in Chapter 5, the simulated transient responses of the CLAMT powertrain are presented in this chapter, which consists of four parts. Firstly, up- and down-shift simulation results verify the effectiveness of the powertrain model as well as control logic. Then, torque spring stiffness of each gear is optimized via quantitative analysis. Next, a continuous gearshift simulation using the optimized spring stiffness is performed. Finally, the impacts of rotating inertia and speed difference on the vehicle jerks are quantitatively investigated.

Chapter 7

This chapter presents the configuration of a testing rig developed for studying the engaging performance of the unilateral Harpoon shift. A torque sensor is carefully calibrated to measure the torque responses during the engaging process. The control unit of the testing bench is based on the dSPACE's flexible prototyping systems. The experimental results are analyzed comprehensively to investigate the engaging transient characteristics of the unilateral Harpoon-shift synchronizer mechanism.

Chapter 8

In this chapter, a novel concept of bilateral Harpoon shift synchronizer is proposed for the EVs equipped with multi-speed CLAMTs. It avoids the shortcomings of the unilateral Harpoon-shift synchronizer as presented at the beginning of this chapter and overcomes the traditional synchronizers' shortcomings. Furthermore, the working principle and the function of each component are illustrated in detail.

Chapter 9

A detailed and original multi-body model of the bilateral Harpoon-shift synchronizer is developed to capture its transient behavior during engagement. In the model, the engaging process is defined as six stages, and it can cover the interacting ways between the engaging-related parts. A speed profile is designed for motor speed adjusting. Additionally, comparisons are performed to demonstrate the superiority of the proposed torque profiles over its counterpart based on a modified bump function. Then the impacts of spring stiffness and tooth chamfer angle is quantitatively analyzed and then these two important parameters are optimized to reduce the shifting shocks.

Chapter 10

This chapter presents the conclusions of this thesis and highlights the potential research works for further investigations.

It should be noted that a proportion of the chapter has been published as journal papers in [1, 23].

Chapter 2

Background and Literature Review

2.1 Introduction

Synchronizer is a significant part of multi-speed transmissions, with the function of eliminating the speed difference between the target gear and shaft within a short time and preventing premature lock by blocking the axial movement of sleeve [23–25]. Thus, it plays an important role in achieving a high-quality shifting and consequently improving the vehicle riding comfort [26]. Currently, traditional cone clutch synchronizers are widely used in electric vehicles equipped with clutchless automated manual transmissions (CLAMTs). Nevertheless, friction losses, heat dissipation, and wear will be inevitable for this type of synchronizer, which has significant influences on the gearshift quality and efficiency of transmission. The requirements of minimizing the energy losses and improving the gear change quality and gearbox efficiency for EVs necessitate an innovation in synchronizer.

In this chapter, background information about the subsystems of the powertrain is introduced. Then the literature survey is performed to explore the state-of-the-art for the design of the synchronization mechanism, the dynamic modeling of synchronizer and CLAMTs, and the shifting control strategies.

2.2 Background Information

2.2.1 Electric vehicles

An electric vehicle is propelled by one or more electric motors supplied directly from the battery [15, 17, 27, 28]. Compared with the conventional vehicles, there are several advantages for EVs, such as no gas required, high efficiency, zero emissions and low noise, etc [8]. Since EVs do not run on fuels, the wide usage of EVs will provide a solution for the scarcity of fossil-fuel resources and the environmental issues. Nevertheless, one of the weakest points of EVs is the battery system [29]. Long distance driving is a challenge for EVs because of the limited electrical energy in the energy-storage devices and the lack of charging infrastructure [15, 23, 30].

2.2.2 Friction clutch

In traditional vehicles, the clutches are utilized to engage the engine to the drivetrain gradually, to avoid undesired shocks and jerks [31–35]. Especially, automotive dry-clutch system in traditional automated manual transmission (AMT) vehicles is controlled electronically to separate and engage engine power for smooth gear shift, due to the high inertia of internal combustion engine (ICE) [36–39].

Currently, there are two types of clutch, i.e. dry clutch and wet clutch [40–42]. For the MTs and AMTs, the launch device is generally a dry clutch, while in ATs and CVTs, this may be a wet clutch or hydraulic torque converter [32].

Diaphragm spring (i.e. Belleville spring) [43] and cushion spring are two important parts in the clutch system. When the cushion spring is not compressed, the clutch is disengaged (i.e. open). Whilst it is completely compressed, the clutch is engaged (i.e. closed) [44], and the engine torque can be fully transmitted through the clutch to the transmission. During dry-clutch engagement, the cushion spring is partly compressed, dry clutch torque due to friction is generated and transmitted to the input shaft of transmission [45]. Factors affecting the torque transmission includes contact pressure, sliding speed, temperature and wear [46–50]. Furthermore, due to the nonlinear load–deflection characteristics of diaphragm spring and cushion spring, clutch engagement control has a crucial influence on the clutch-torque transmissibility characteristic [51–54], which significantly affects the driving comfort [55, 56].

2.2.3 Transmissions

The function of the transmission is to transfer power from the engine to the drive shaft and finally to the wheels [57]. In addition, it can change the speed and torque through the gear ratio. Currently, transmissions available in commercial market can be classified into five main types: manual transmission (MT), automatic transmission (AT), automated manual transmission (AMT), dual clutch transmission (DCT), and continuously variable transmission (CVT) [24, 58, 59].

MT is also known as “standard” transmission, a driver has to use both a gear selector and a clutch to change gear manually. There are several advantages for the MT, including high efficiency, low cost, and low weight [8, 60]. Particularly, the MT have the highest efficiency among any type of transmissions, with an overall efficiency of 96.2% [61]. Nevertheless, the main weakness of the MT is the torque interruption when the transmission is between gears [62]. The engine is disconnected from the gearbox as the clutch is disengaged during shifting, leading to the interruption of power flow and consequently the shifting shock.

Classic AT is composed of a torque converter and planetary gears [63–65]. The output of the torque converter is connected to the planetary gear input. The hydrodynamic torque converter is applied to amplify the drive torque at vehicle launch. Furthermore, it functions as a damping element to absorb torsional oscillations [66]. It can significantly influence the vehicle transient characteristics during gear change as well as vehicle launching [67]. The planetary gearing set is utilized to perform gear change that is automatically controlled by an electronic control unit (ECU) via a hydraulic system [68], which provides more convenience for driving. However, there are still shortcomings in ATs, including the considerable power losses due to the low efficiency of torque converter and the complex overall structure [36, 58].

AMT generally consists of a multi-gear transmission and a dry clutch, both equipped with electromechanical or electro-hydraulic actuators [44, 57, 69]. Thus, AMT is basically a MT and inherits the merits of MT such as high efficiency (same as MT) and low cost, and provides operation convenience similar to conventional AT [8, 61, 70–72]. However, AMTs also have shortcomings, such as torque interruption during gear shift process, resulting in the undesired shifting jerk [73–77], and excessive wear of clutch friction plates [78, 79]. Therefore, the clutch control in the AMT system plays a key role for the riding comfort during standing start and gear change of conventional vehicles [42, 80–82]. During the gearshift in AMTs, the actuator is driven by a transmission control unit (TCU) [58, 83, 84] to control the clutch engagement.

The DCT architecture is based on the AMTs' configuration, but the former uses dual clutches and gear shafts to transfer the engine power [85]. The two clutches can quickly switch between gear shafts when the actual gear shift is required [86]. Generally, DCTs equipped with electrohydraulic transmission control module [87]. Through removing the inefficient torque converter, the fuel efficiency and performance of the DCTs are dramatically improved [87, 88], when compared to CVTs and planetary-type ATs [87]. Nevertheless, as the clutch-to-clutch gear change is conducted too fast, it is more likely to cause substantial shifting shocks to the powertrain systems, owing to the absence of the smoothing effect of torque converter [85]. The coordinated control of the ICE throttle and the two clutch actuators plays a crucial role in achieving a smooth and fast gear shifting for DCTs [85, 89–91].

A CVT, also known as a shiftless transmission, is an automatic transmission that allows seamless gear change with numerous range of ratios [92, 93]. CVTs usually utilize belt and pulleys, instead of steel gears used in conventional transmission, as ratio change mechanism [94]. The primary advantage of CVTs is that it allows the engine to rotate in the most fuel-efficient way [61, 95]. However, conventional CVTs have several disadvantages, such as limited torque capacity, low transmission efficiency and complex mechanical systems. The CVTs have yet to replace conventional transmissions because of their larger size, higher cost, and/or lack of durability [96].

2.2.4 Synchronizer

Synchronizer is an important component in multi-speed transmissions. It is used to connect two separate rotating parts with positive interlocking through the spline meshing of engaging-related components [97].

Transmissions with multiple ratios, such as MTs, DCTs and AMTs, utilize the synchronizer mechanism to achieve a smooth gear shift [98, 99]. Conventional synchronizers use cone torque, generated by the friction under the action of axial shifting force, to eliminate the speed difference between the rotating parts to be engaged [100–103]. Furthermore, synchronizer mechanism should be carefully designed to block the sleeve axial movement during speed synchronization, which helps to reduce the shifting effort and prevent premature lock [104–107]. Unreasonably design parameters may lead to the failure of blocking the sleeve before the speed synchronization completes [108]. In this case, tooth crash will be inevitable when the sleeve engages the clutch gear directly, resulting in a greater jerk or even damage of the tooth splines [109]. Therefore, synchronizers play a crucial role in improving the shifting quality, riding comfort and driving safety and extending the service life of transmissions [110–113].

However, there are still shortcomings for the traditional cone-clutch synchronizers, including friction losses, heat dissipation and wear, which significantly affect the synchronizer performance and efficiency [114–117].

2.2.5 Synchronizing process of cone-clutch synchronizers

The synchronizing process of conventional synchronizer mechanism can be divided into eight phases [22, 118–120], as follows:

1. First free fly.

   The shift sleeve move axially towards the clutch gear under the axial shifting force [98]. During this phase, the required actuating force is low since there is almost no significant mechanical resistance [22, 119].

2. Start of speed synchronization.

   The axial force increase and the blocking ring approaches the gear cone. The oil between the cone surfaces of the gear cone and blocking ring is compressed and the oil film pressure begins to increase [98]. Frictional torque also increases and then rotate the ring within available clearance. In this phase, there is a spline contact between the blocking ring and sleeve [22].

3. Speed synchronization.

   The sleeve stops axial movement in this phase. The speed discrepancy between the target gear and sleeve reduces gradually to zero due to the cone friction [23, 119].

4. Turning the blocking ring.

   When the speed discrepancy is eliminated, the blocking ring is stuck on the cone. And the sleeve rotates these two parts when the spline chamfers of the ring and the sleeve are in contact [119, 121].

5. Second free fly.

   The sleeve slides axially until its teeth contact with the target gear tooth chamfer. In this stage, the rotating speed the sleeve and the gear are almost identical [22].

6. Start of the second bump.

   The axial force increases significantly to separate the blocking ring stuck on the gear cone. The second bump phenomenon happens during this phase [22].

7. Turning the target gear.

   When the blocking ring is separated from the gear, the sleeve rotates the target gear and move forwards [121, 122]. It should be noted that the double bump also exists in this phase.

8. Final free fly.

   When the target gear is rotated, the sleeve moves forwards. Finally it reaches the fully engaged position and the engagement is complete [122].

2.3 Literature Review

In order to solve the issues of nonrenewable fuel shortage and environmental degradation [23, 123], electric vehicles have attracted worldwide attention due to their unique advantages, such as high efficiency, energy saving, low or zero emission and low noise [8, 23], when compared to conventional cars with an internal combustion engine (ICE) as the main power source. However, one of the challenges for EVs is that the energy density of electric batteries is much less than that of fossil fuels, which dramatically limits the drive range of EVs [15, 23]. Therefore, energy saving and fuel efficiency improvement have been the research focuses for EVs.

However, since the electric motor (EM) of EVs has extraordinary low-speed control characteristics as well as different work modes, including free mode, torque mode, and speed mode [124], the clutch equipped in AMT vehicles can be removed [125, 126]. These merits of EM greatly benefit gear shifting control. As a result, the clutchless automated manual transmissions (CLAMTs) are increasingly used in EVs [74].

Currently, most commercial EVs are equipped with single-ratio transmissions due to their low manufacturing cost, compact volume and simple configuration [17, 23, 28, 127, 128]. However, an obvious drawback of this kind of transmission lies in the compromise between dynamic performance (i.e. grade climbing, maximum speed, and acceleration) and efficiency (drive range) [15, 17, 19, 20, 23]. Since single-speed transmission cannot ensure the motor works in high efficiency range for most driving conditions [11, 23, 129], application of multiple speed transmissions in EVs has received increasing attentions [2, 11, 16, 130, 131].

In particular, research in [12, 17, 123, 132, 133] have proved that multi-speed CLAMT has the potential to improve the overall efficiency and drivability of EVs. Nevertheless, one of the challenges of multi-gear CLAMTs is the poor gear-shift quality as a result of torque interruption [8, 12]. In order to reduce the torque hole and consequently improve shifting quality, research attentions mainly focus on the following aspects:

2.3.1 Advanced gear shift control strategies

A robust optimal speed synchronization control logic was proposed in [125, 134], aiming to satisfy the requirement of high-precision speed synchronization for the CLAMTs to achieve high quality shifting. Yu et al. [36] put forward gear shift control strategy for CLAMT, which includes model parameters identification, speed synchronization control and motion control of actuator. Wang et al. [75] proposed a position and force switching control scheme for AMT gear engagement to reduce the shifting shocks which has significant influence on the synchronizer lifetime.

In addition, a seamless gear-shift strategy for 3-speed CLAMT is designed in [9], which controls the gearshift actuators independently and simultaneously. As the outgoing gear starts to disengage the current gear, the oncoming gear begins the speed synchronization. As a result, the cone frictional torque of oncoming gear can supply a few driving torque to the output shaft during shifting, which can reduce both torque interruption and shift time.

Walker et al. [16] replaced the internal combustion engine (ICE) with a motor for a two-speed dual clutch transmission (DCT) of electric vehicles. They also put forward a series of power-on and power-off shift control strategies and verified the effectiveness of the proposed strategies for gearshift control in EVs through simulation and experiment.

2.3.2 Innovative transmission configurations

Liang et al. [18] put forward a novel dual input clutchless AMT system equipped with two motors for EVs, in order to develop a transmission capable of maximizing energy efficiency, reducing emissions, and achieving acceptable drivability. They established a mathematical model of the proposed system to investigate its transient dynamics during shifting. Simulation results validated the effectiveness of the proposed powertrain. Furthermore, based on the established model presented above, they proposed a real-time power sharing control (PSC) strategy to address the issue regarding power distribution between the two motors [17], to achieve high overall efficiency and maintain adequate drivability. Also, in order to eliminate the torque hole during gear change process, they developed a shift control strategy based on a modified bump function to coordinate the speed and torque change of the motors.

A novel transmission concept is proposed by Zhao et al. [13], named the uninterrupted shift transmission (UST) which can offer an uninterrupted torque during shifting. The key characteristics of UST is based on a multi-mode controllable shifter (MCS) which is actually a special type of bidirectionally controllable one-way clutch (COWC). In addition, they developed an UST mathematical model and synergetic control logic. Results from simulation and tests demonstrate that the control strategy of motor torque and clutch torque intervention during shift process can greatly reduce the jerk. However, the proposed UST cannot completely eliminate the need for friction clutch to accomplish speed matching between the motor and the clutch driven plate, which will inevitably cause energy loss due to frictional work.

Kuroiwa et al. [135] presented an original torque-assist automated manual transmission (AMT), with an assist clutch (ACL) replacing the fifth gear synchronizer in conventional AMTs. Comparison of up-shift performance between the ACL-AMT and conventional AMT as well as automatic transmission (AT) demonstrates that the proposed ACL-AMT is capable of achieving the seamless shifting of an AT and the fuel economy of a manual transmission (MT). Then Galvagno et al. [57] built a detailed dynamic model of the ACL-AMT to study and quantify the power contributions for different engine and ACL interventions. Simulations showed that the torque gap is considerably alleviated during shifting phase.

Mousavi et al. [15] developed a compact two-speed clutchless seamless dual brake transmission for electric vehicles. It is composed of a double-stage planetary gear set with common sun gear and ring gear. It can achieve a fast and smooth gearshift by controlling the speed of the ring gear and sun gear using two friction braking mechanisms. They also proposed a shifting control strategy on the basis of the Pontryagin's Minimum Principle (PMP) to eliminate torque hole. Nevertheless, the brakes applied in the system also involve friction work and energy dissipation.

2.3.3 Improvement of synchronizer performance

Synchronizer is an important component of transmission and plays a significant role in engaging performance [21, 27, 122, 136, 137]. Extensive studies have been performed on improving the engaging performance of the traditional synchronizer with cone clutch.

Lovas et al. [22] defined eight main phases to describe the traditional synchronizer behavior during gear change process. Then, they built a numerical model to study the synchronizer performance.

A thermal-structural coupling model was developed in [138] to study the influence of friction coefficient and friction heat on the shifting control accuracy and shift quality. Furthermore, experiment was also established to verify the model.

Chen et al. [109] applied hybrid system modeling techniques and multi-body dynamics to analyze the engaging process of conventional synchronizer equipped in AMTs. The model helps to figure out the effects of the shift force and the relative position between sleeve and clutch gear on the engaging performance.

Li et al. [122] established a detailed parameterized dynamic model of adouble-cone synchronizer. Based on the model, four parameters are chosen to investigate the sensitivity. Simulation results show that the friction coefficient of cone clutch can greatly influence the shifting force and synchronization duration, and the blocker angle (i.e., chamfer angle) has a significant impact on the gearshift performance. While the cone angle and the stiffness of the pressure springs have a little influence on the smoothness of gear change.

A concept of double indexing was put forward in [98]. Rather than through increasing the gear shift lever ratio or using a multi-cone synchronizer, the double indexing synchronizer is capable of increasing the conventional synchronizer capacity by 30%, with only a small modification to the traditional single-cone counterparts.

Fang et al. [139–142] proposed a novel concept of synchronizer mechanism for EVs, named 'Harpoon-shift' consisting of a dog clutch and a torsional shock absorber. Different from the conventional synchronizers which rely on the friction torque of cone clutch to finish speed synchronization [21, 22, 109, 143], the Harpoon-shift applies flexible components, i.e. torque springs, to eliminate the residual speed difference between the target gear and shaft. This thus overcomes the shortcomings of traditional synchronizers, such as energy loss due to friction work and excessive wear of the friction components [122, 136]. Based on the concept of Harpoon-shift aforementioned, a detailed mathematical model of the Harpoon-shift is developed in [1] to investigate its transient characteristics. Additionally, an experiment based on a full-scale prototype of Harpoon-shift was developed to verify the effectiveness of the model.

Nevertheless, there are still some limitations in these studies associated with the conventional synchronization mechanisms, although a great number of related literature can be found.

1. Most studies mainly concentrate on the conventional synchronizer with cone clutch. And the gear shift mainly relies on the friction elements. Therefore, friction losses, wear as well as heat dissipation are inevitable, leading to the substantial energy losses and transmission performance declination for multi-speed EVs.
2. The powertrain model does not integrate a detailed model of synchronizer. It is necessary to include the influences of the subsystems involving the gear shifting, since they can significantly affect the system transient characteristics.
3. Some hypotheses applied in these studies lack the experiment validation. Thus, it is hard to evaluate their actual effects.

2.4 Assumptions of Current Research

The assumptions used in this study are the followings:

1. The two branches of driveline system, i,e., the right and left driveshafts and wheels, are collapsed in one branch to reduce the overall degrees of freedom (DOFs) of the powertrain model, based on the assumption that the two branches are perfectly symmetric.
2. The backlash and nonlinear mesh in gear sets are ignored in the powertrain model.
3. The tire model is simplified based on the assumption that the tire belt is in perfect contact with road and no slip happens. This model only considers the rotation motion.
4. A detailed motor model is not developed in the study, and the mean torque model is used instead.
5. The actuator model is not built in the study. Instead, an axial force is utilized to represent the force supplied by the actuator mechanism.
6. The influences of temperature and efficiency loss in the powertrain system are not taken into consideration in the study.

2.5 Summary

Synchronizer mechanism plays an important role in improving transmission performance and gear shift quality. The objectives of this project focus on improving the synchronizer engaging performance and investigating its influences on the powertrain system during shifting for multi-speed EVs. Furthermore, a literature survey is performed in this chapter to present the current technologies and methodologies applied in the design, dynamic modeling and control of the powertrain system and synchronizer EVs. In addition, the issues and limitations existing in the techniques are identified. It is worth pointing out that a proportion of the chapter has been published in [23].

Chapter 3

Concept of Unilateral Harpoon Shift

3.1 Introduction

In order to overcome the drawbacks of traditional synchronizer with cone clutch, such as friction losses and wear [23], the concept of unilateral harpoon shift is presented in this chapter. It is designed to eliminate any speed difference within the engaging gear set and to minimize transients during the gear shift process [1]. Ultimately, it provides a means to select and engage gears without the use of friction clutches. This mechanism relies on the relative speed difference between the sleeve hub and target gear and must ensure the hub is faster than the target gear to achieve engagement. The main components for the Harpoon Shift mechanism and their functions are introduced in the chapter.

3.2 Concept of Unilateral Harpoon Shift

A conventional synchronizer mechanism requires (i) matching speed between a freewheeling gear and shaft by using a cone clutch [144, 145], (ii) physically interlocking the gear to the shaft by using a dog clutch, and (iii) seeking no premature engagement leading to the damage of mechanical parts via the design of dog and cone clutches [6, 21].

Most conventional synchronizers apply frictional cone clutch to realize the speed alignment [146–148]. Generally, the synchronizing process of this kind of synchronizer is complicated due to a large number of subsystems involved during actuation as well as the control of axial actuating force in each phase of engagement.

However, for electric vehicles, the electric motor can eliminate most of the speed difference due to the more controllable characteristics of the motor, thanks to its much smaller rotating inertia compared to the internal combustion engines (ICE) and distinguished low-speed control capability [23]. This significantly reduces the need for friction clutches. Nevertheless, the removal of synchronizers in a multi-speed transmission, i.e. accomplishing the speed alignment by the motor only and engaging two rotating parts by the dog clutch alone, would expose the risk of 'clash' (also called 'kick tooth') type failures if there is a high relative speed between the engaging-related components. Typically this is caused by the sensor fault or precision as it has a significant influence on the performance of the traction motor speed control as well as the actuator axial displacement control during the gearshift process [70].

Based on the considerations presented above, the synchronizer mechanism is still retained in this study and our research focuses on the transients of the CLAMT equipped electric vehicles during gear shifting. The synchronizing process consists of two phases: active speed synchronization by adjusting the motor speed and mechanical speed synchronization by the synchronizer [8]. The driving motor synchronizes the dog gear speed toward the threshold in the first phase and the synchronizer mechanically eliminates the residual speed difference in the second phase.

In order to overcome the issues of conventional synchronizers with cone clutch, including the energy dissipation due to friction and abrasion of the friction components, a new synchronizer is presented in this research, namely unilateral Harpoon shift which is initially developed in [1, 139, 142] and designed as an alternative to the traditional synchronizers. Unlike its traditional counterparts, Harpoon shift depends on the speed discrepancy between the sleeve hub and the gear to be engaged to finish engagement.

The Harpoon-shift mechanism consists of a dog gear connected with constant mesh gear (i.e., target gear), sleeve, hub, guide ring, torque springs, and shaft, as shown in Fig. 3.1 [1, 142]. The constant mesh gear is rigidly fixed on the dog gear and thus they have the same angular speed. In addition, they are supported by a needle bearing, allowing them to freewheel with respective to the output shaft. The Harpoon-shift interlocking can be realized through the angled chamfers on the external groove of dog gear and the sleeve prongs, or by the locking of the shifting actuator, to match the speed of hub and output shaft [1].

The guide ring is installed between the sleeve and dog gear, and the torque springs elastically connect the guide ring and dog gear. When the guide ring is in the initial position, it blocks the dog gear external grooves to prevent premature locking. As the torque springs are compressed due to the speed difference, torque will be transmitted through the springs to accelerate the dog gear rapidly. In this way, the speed difference between the target gear and shaft can be eliminated before the locked-up phase starts. This will greatly reduce the shifting jerk.

The schematic diagram of the unilateral Harpoon shift is similar to that of the bilateral version (proposed in Chapter 8) to a certain degree, since both of the two novel synchronizers apply the torque spring to absorb shifting shock (see Fig. 8.2(b)).

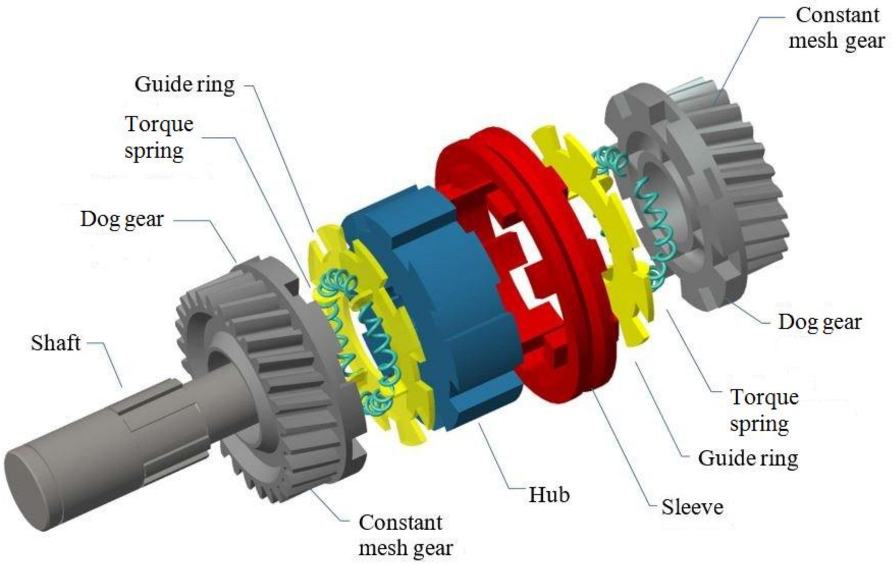

Figure 3.1 : Exploded view of Harpoon-shift

The sleeve has internal splines and it mechanically connects the output shaft in the rotational direction via the hub with external splines. Thus the sleeve can only slide axially between the engaged position and the neutral position under the actuating force provided by the shift mechanism [1].

The functions of the main components for the unilateral Harpoon shift mechanism are as follows [1]:

- Constant mesh gear: these are common gears in lay-shaft type transmissions. Typically, the gears are supported on the primary shaft with a needle bearing to allow relative rotation when freewheeling and secured against the axial movement to the shaft.

- Dog gear: matches the speed of the gear with the speed of the Harpoon-shift hub and output shaft. The external groove interlocks with the internal prong of the Harpoon-shift sleeve. Internal circular grooves retain the torque springs.
- Torque spring: one end contacting the step of the dog gear and the other side remains in contact with the guide ring. Typically, the guide ring compresses the spring, providing a torque to counteract residual relative speed between the hub and constant mesh gear before the sleeve completes engagement.
- Guide ring: this ring has chamfers on one side to guide the sleeve to insert the synchronizer groove smoothly. Once the sleeve has mated with the guide ring, relative motion between sleeve and dog gear will compress the spring. To do so, tabs on the other side for ring engage the torque spring.
- Harpoon-shift sleeve: this could be engaged by using an actuator via the gearshift fork. It has internal splines that are in constant mesh with the Harpoon-shift hub external splines, so it can only move axially from the neutral position to an engaged position. The main function of the prongs is to engage with the guide ring during speed matching and interlock with the dog gear when engaged.
- Harpoon-shift hub: is mounted on the rotating shaft via a spline. Shaft: it has an external spline that constantly meshes with the internal splines of the Harpoon-shift hub and supports the idle constant mesh gears through bearings.

In comparison with the traditional synchronizers, the key characteristics of Harpoon shift are shown as follows [23]:

- Unlike conventional synchronizers, Harpoon shift utilizes the flexible components (torque springs) to eliminate speed difference. This solves the issues of energy loss and wear due to friction.
- Harpoon-shift significantly simplifies the actuating complexity during the engagement as it uses a mechanical limiting mechanism to control the sleeve axial movement throughout the engaging phase, including the frontal faces of guide ring and dog gear as well as the external groove bottom [1]. Therefore it can apply open-loop control rather than the closed-loop control to realize the engagement.
- Harpoon-shift needs only a low actuation force to finish engagement. In this study, the shifting force is only 38 N, in comparison to the traditional synchronizers which use 500 N to 1000 N.

Besides the advantages mentioned above, the manufacturing cost of the proposed Harpoon shift would be less than that of traditional synchronizers since the frictional cones are removed in the Harpoon-shift synchronizer. Generally, the frictional cones require closer manufacturing tolerances and hence entail higher manufacturing costs [149]. While the reliability of the proposed synchronizer is not considered in the research.

It should be noted that in order to achieve a successful engagement, the hub of Harpoon shift must be faster than the target gear, thus this kind of synchronizer is called unilateral Harpoon shift [23]. The working principle of Harpoon shift is to apply the kinetic energy stored in the inertia to compress the torque spring and turn the guide ring into an open position where the sleeve can engage the dog gear. Therefore, the torque spring stiffness has a significant influence on the engagement performance of Harpoon-shift, and this will be investigated in Chapter 6.

As shown in Fig. 3.2 [1, 23], the Harpoon shift is simplified to four main working parts to clearly show the operating process, including the dog gear, guide ring, sleeve, and torque springs which are not displayed as they are installed in the inner groove of dog gear. It is worth noting that the sleeve prong has a round corner, and there is line contact between the sleeve prong and the guide ring or dog gear, which can overcome the issue of excessive wear.

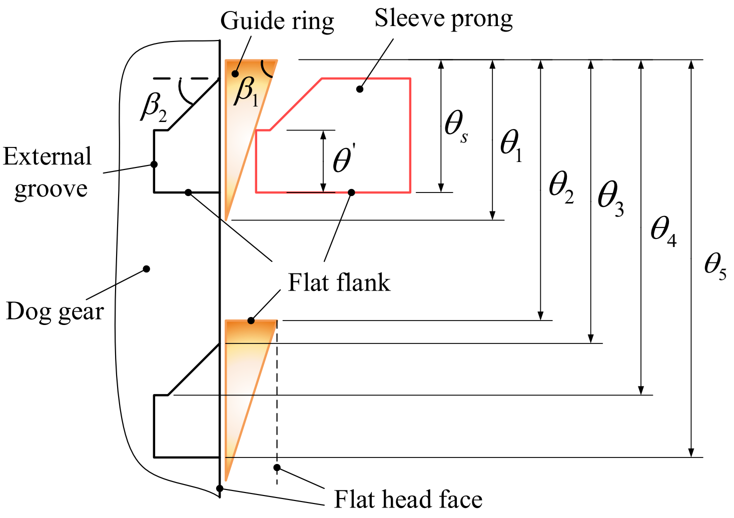

Figure 3.2 : Angular parameters and working components of Harpoon shift

3.3 Summary

The concept of unilateral Harpoon-shift synchronizer is introduced in this chapter. Different from the conventional synchronizers which utilize friction elements to eliminate the speed difference between the sleeve and target gear, the Harpoon shift relies upon the speed difference to rotate the guide ring into an open position and complete the engagement. It can overcome one of the biggest issues of the traditional synchronizer, i.e., friction losses. It should be noted that a substantial proportion of the chapter has been published in [1, 23].

Chapter 4

Dynamic Modeling of Unilateral Harpoon Shift and Powertrain System with CLAMT

4.1 Introduction

In this chapter, in order to investigate the dynamic behavior of an EV powertrain system equipped with multi-ratio CLAMT during gear shifting, an original multi-body model of the powertrain system is developed. In addition, to take the influences of the synchronizer subsystem on the powertrain transient characteristics, a detailed dynamic model of unilateral Harpoon-shift synchronizer is developed to figure out its transient characteristics.

4.2 Dynamic Modeling of an EV Powertrain with a Multi-Speed CLAMT

In this section, a multi-speed EV CLAMT powertrain system equipped with Harpoon shift is modeled as a multi-body model as shown in Fig. 4.1 [23]. The motor directly connects the input shaft of a multi-speed transmission. The output side of transmission components includes final drive gear and differential, half shafts, wheel hubs, and vehicle equivalent inertia [18, 150]. In this study, four spring-dampers are used in the model to represent the flexibilities of the input shaft and output shaft of the transmission, half shafts, and tires [23]. T_m denotes the motor output torque, while T_{gin}, T_{slout}, T_{dout} represent the torques transferred by the transmission input shaft, output shaft and drive shaft. T_{hv} is the torque transmitted by the tire to the vehicle.

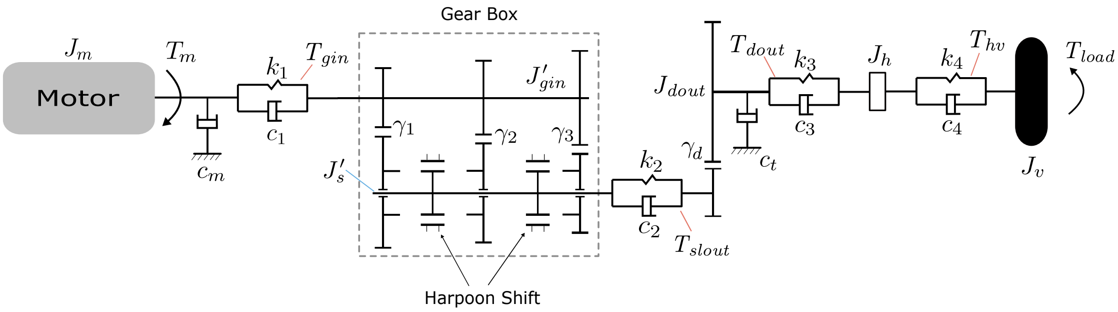

Figure 4.1 : Model of an EV powertrain system with multi-speed CLAMT

Particularly, based on the assumption that the tire belt is regarded as a gear in perfect coupling with the road and thus there is no slip between the belt and road surface [23, 151], the tire sidewall, which flexibly connects the wheel rim and belt, is represented by a linear torsional spring-damper with fixed stiffness and damping (i.e., k_4 and c_4) rather than a complex non-linear model. This simplified model only considers the rotation motion, while the longitudinal and vertical motions of the tire are not taken into account in this study. More details about the tire model can be found in [151].

To reduce the computing cost, the two branches (the right and left half shafts and the wheels) are collapsed in one based on an assumption that they are symmetric [23]. The differential equations describing the rotating motion of the DOFs of transmission input and output sides are shown below, while the dynamics model of Harpoon shift is presented in the following section.

$$J_m\ddot{\theta}_m = T_m - k_1(\theta_m - \theta_{gin}) - c_1(\dot{\theta}_m - \dot{\theta}_{gin}) - c_m\dot{\theta}_m \tag{4.1}$$

$$\begin{aligned} J_{dout}\ddot{\theta}_{dout} = {} & \gamma_d[k_2(\theta_s - \theta_{dout}\gamma_d) + c_2(\dot{\theta}_s - \dot{\theta}_{dout}\gamma_d)] - k_3(\theta_{dout} - \theta_h) \\ & - c_3(\dot{\theta}_{dout} - \dot{\theta}_h) - c_t\dot{\theta}_{dout} \end{aligned} \tag{4.2}$$

$$J_h\ddot{\theta}_h = k_3(\theta_{dout} - \theta_h) + c_3(\dot{\theta}_{dout} - \dot{\theta}_h) - k_4(\theta_h - \theta_v) - c_4(\dot{\theta}_h - \dot{\theta}_v) \tag{4.3}$$

$$J_v\ddot{\theta}_v = k_4(\theta_h - \theta_v) + c_4(\dot{\theta}_h - \dot{\theta}_v) - T_{load} \tag{4.4}$$

where J_m is the motor inertia, J_{dout} is the equivalent inertia associated with the fixed final drive ratio, J_h is the equivalent inertia of wheel hubs, J_v is the vehicle equivalent inertia, which includes the tire inertia. c_n and k_n $(n = 1, 2, 3)$ represent the damping and stiffness coefficients of each shaft, c_4 and k_4 are the tire damping and stiffness, c_m and c_t denote the viscous damping coefficients. θ represents angular displacement, and its two time derivatives denote rotating velocity and acceleration. γ_d represents the final ratio. T_{load} denotes the load torque including the climbing resistance, rolling resistance and aerodynamic drag, which can be calculated by

$$T_{load} = \left[m_v g\sin(\phi) + f_r m_v g + \frac{1}{2}C_d A_F \rho_{air}(r_w\dot{\theta}_v)^2\right] r_w \tag{4.5}$$

in the above equation, $\phi, f_r, m_v, g, \rho_{air}, C_d, A_F$ and r_w are incline angle of road, rolling resistant coefficient, vehicle mass, gravitational acceleration, air density, drag coefficient, vehicle front area and effective wheel radius [152], respectively. In this study, $\phi = 0°$.

In the model, the shaft damping coefficients are constant. The value of each damping coefficient can be estimated since it has a relationship with the damping ratio and shaft stiffness coefficient as presented in [153]. These damping coefficients could also affect the torsional vibration of the drive train system, which has an impact on the gearshift control effect. Therefore, the values of these coefficients should be reasonable.

In addition, the shifting force F_a is constant during the engagement, and it can be estimated through an experiment using a pneumatic cylinder as the actuator, and the required actuation force is supplied by the compressed air with nominal pressure.

4.3 Modeling of Unilateral Harpoon Shift

The engaging process of unilateral Harpoon shift can be outlined in seven phases according to the axial displacement of the sleeve and the relative position between sleeve prongs and guide ring as well as dog gear [23]:

Phase 1 ($0 \leqslant \theta_s < \theta'$): Fig. 4.2 [1] displays the first phase of engagements. The sleeve moves axially toward the dog gear under the axial shifting force F_a. In this study, the shifting force is constant throughout the entire engaging phase and its value is 38 N. The axial movement of the sleeve is blocked when its prongs contact the guide ring front face, indicating that the engagement enters the next phase. It should be noted that under certain conditions, the prongs can directly touch the chamfer surface of guide ring or the dog gear flat head face instead of the guide ring front face, which means the actuation enters phase 2 or 3. The motions can be described by the following formula:

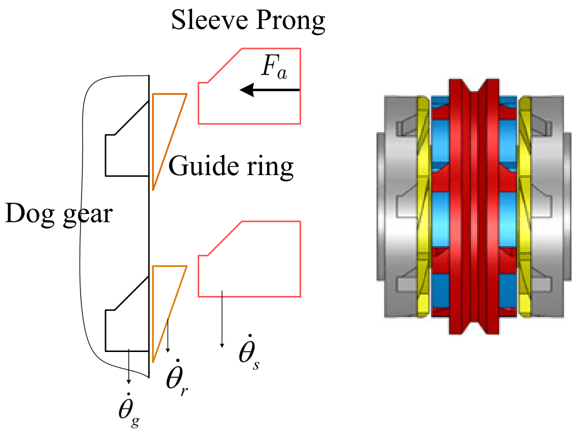

Figure 4.2 : Engaging process of unilateral Harpoon shift: phase 1

$$J_s'\ddot{\theta}_s = -k_2(\theta_s - \theta_{dout}\gamma_d) - c_2(\dot{\theta}_s - \dot{\theta}_{dout}\gamma_d) \tag{4.6}$$

$$J_{gin}'\ddot{\theta}_{gin} = k_1(\theta_m - \theta_{gin}) + c_1(\dot{\theta}_m - \dot{\theta}_{gin}) + T_{spring} \tag{4.7}$$

$$J_{r_i}\ddot{\theta}_{r_i} = -k_{rg_i}(\theta_{r_i} - \theta_{g_i}) - c_{rg_i}(\dot{\theta}_{r_i} - \dot{\theta}_{g_i}) - T_{p_i0} \tag{4.8}$$

$$m_s\ddot{x}_s = F_a - c_{x_1}\dot{x}_s \tag{4.9}$$

where

$$T_{spring} = \sum_{k=1}^{3}\frac{1}{\gamma_k}[k_{rg_k}(\theta_{r_k} - \theta_{g_k}) + c_{rg_k}(\dot{\theta}_{r_k} - \dot{\theta}_{g_k}) + T_{p_k0}] \tag{4.10}$$

$$\theta_{g_i} = \theta_{gin}/\gamma_i, \dot{\theta}_{g_i} = \dot{\theta}_{gin}/\gamma_i \tag{4.11}$$

in the above equations, J_s' is an equivalent inertia including the sleeve and hub inertia. J_{gin}' is the equivalent inertia on the input shaft, including the inertia of input shaft and all gear pairs of the transmission. J_{r_i} is the guide ring inertia. m_s is the sleeve mass. θ_s, θ_{gin}, and θ_{r_i} represent the angular displacements of sleeve, input shaft and guide ring of i-th gear to be engaged, respectively, and their two time derivatives denote rotating velocities and accelerations. x_s and $\dot{x}_s$ are the axial displacement and speed of the sleeve. c_{x_1} is the viscous damping when sleeve moves in the axial direction. θ_{g_i} and $\dot{\theta}_{g_i}(i = 1, 2$ or $3)$are the angular displacement and speed of the target gear, respectively. γ_i represents the i-th gear ratio. $T_{p_{i0}}$ is the torque generated by the pre-compression of the torque springs of i-th gear, here $T_{p_{i0}} = k_{rg_i}\theta_{rg_0}$, where θ_{rg_0} is the pre-compression radian of the torque springs.

Phase 2 ($\theta' \leqslant \theta_s < \theta_1 + \theta'$): During this phase, the sleeve prong slides along the chamfer of guide ring which still blocks the external groove of dog gear to prevent premature locking, as shown in Fig. 4.3 [1]. There is friction on the contact surface between the prong and guide ring. This phase ends when the prong touches the dog gear flat head face. The dynamic equations are shown as follows:

$$J'_s\ddot{\theta}_s = -k_2(\theta_s - \theta_{dout}\gamma_d) - c_2(\dot{\theta}_s - \dot{\theta}_{dout}\gamma_d) + (F_a - c_{x_1}\dot{x}_s)R_m\frac{1 - \mu_s \tan\beta_1}{\tan\beta_1 + \mu_s} \tag{4.12}$$

$$J'_{gin}\ddot{\theta}_{gin} = k_1(\theta_m - \theta_{gin}) + c_1(\dot{\theta}_m - \dot{\theta}_{gin}) + T_{spring} \tag{4.13}$$

$$J_{r_i}\ddot{\theta}_{r_i} = -k_{rg_i}(\theta_{r_i} - \theta_{g_i}) - c_{rg_i}(\dot{\theta}_{r_i} - \dot{\theta}_{g_i}) - (F_a - c_{x_1}\dot{x}_s)R_m\frac{1 - \mu_s \tan\beta_1}{\tan\beta_1 + \mu_s} - T_{p_{i0}} \tag{4.14}$$

where R_m is the mean contact radius between the sleeve prongs and guide ring blocks. Since axial and tangential velocities are connected on the chamfers of guide ring [22], the DOF describing sleeve axial motion is constrained (i.e. not independent) during this phase. Hence, its axial acceleration can be obtained from the tangential acceleration:

$$\ddot{x}_s = (\ddot{\theta}_s - \ddot{\theta}_{r_i})R_{out}\cot\beta_1 \tag{4.15}$$

where R_{out} is the outside radius of the guide ring and dog gear.

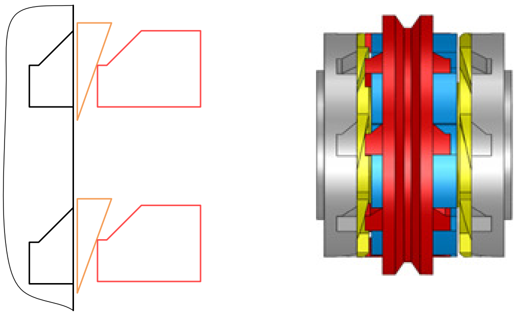

Figure 4.3 : Engaging process of unilateral Harpoon shift: phase 2

Phase 3 ($\theta_1 + \theta' \leqslant \theta_s < \theta_2$): Fig. 4.4 [1] displays the third phase. During this phase, the prongs slide on the dog gear flat head face, thus its axial movement is blocked, i.e. $\dot{x}_s = 0$ and $\ddot{x}_s = 0$. This special structural design is deliberately used to prevent the prong engaging the dog gear before the speed discrepancy is eliminated. This phase ends when the sleeve prong flank contacts the next prong flat flank of the guide ring. There is friction on the contact surface between the prongs and dog gear. The motion equations regarding this phase are expressed as

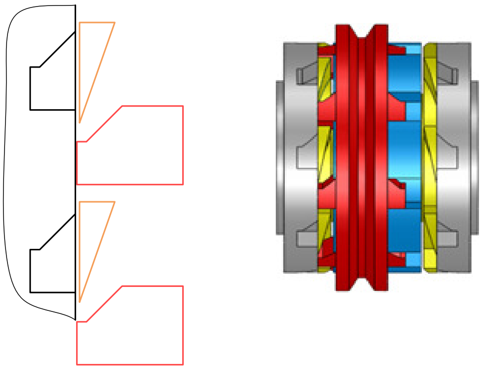

Figure 4.4 : Engaging process of unilateral Harpoon shift: phase 3

$$J'_s\ddot{\theta}_s = -k_2(\theta_s - \theta_{dout}\gamma_d) - c_2(\dot{\theta}_s - \dot{\theta}_{dout}\gamma_d) - \mu_{sg}(F_a - c_{x_1}\dot{x}_s)R_m \tag{4.16}$$

$$J'_{gin}\ddot{\theta}_{gin} = k_1(\theta_m - \theta_{gin}) + c_1(\dot{\theta}_m - \dot{\theta}_{gin}) + T_{spring} + \frac{1}{\gamma_i}\mu_{sg}(F_a - c_{x_1}\dot{x}_s)R_m \tag{4.17}$$

$$J_{r_i}\ddot{\theta}_{r_i} = -k_{rg_i}(\theta_{r_i} - \theta_{g_i}) - c_{rg_i}(\dot{\theta}_{r_i} - \dot{\theta}_{g_i}) - T_{pi0} \tag{4.18}$$

Phase 4 ($\theta_2 \leqslant \theta_s < \theta_3 + \theta'$): As shown in Fig. 4.5 [1], there is a collision between the sleeve prong and guide ring. As illustrated in Section 3.1, the precondition for Harpoon shift to successfully accomplish engagement is that the sleeve rotating speed must be faster than that of the dog gear, thus the prong starts to open the guide ring and compress the torque springs due to the relative rotation of the two rotating parts. Therefore, the driven parts, including the dog gear and constant mesh gear, are accelerated rapidly by the torque transmitted via the springs, which helps to eliminate the speed difference and consequently reduces the shifting jerk of the vehicle. displays the third phase. During this phase, the prongs still slide on the dog gear flat head face, thus $\dot{x}_s = 0$ and $\ddot{x}_s = 0$.

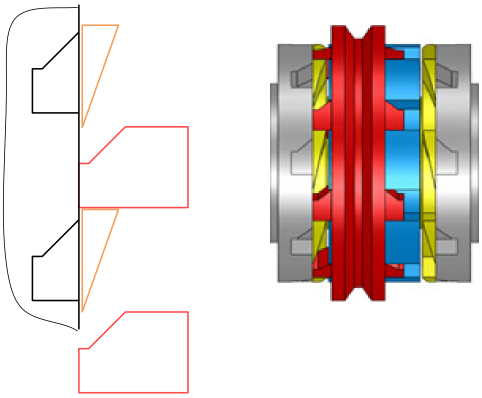

Figure 4.5 : Engaging process of unilateral Harpoon shift: phase 4

In this study, the impact function [122, 154, 155] is employed to calculate the contact force due to the collision. Detailed introduction of the function can be found in Appendix A. The equations of motion regarding this phase are the follows:

$$J_s'\ddot{\theta}_s = -k_2(\theta_s - \theta_{dout}\gamma_d) - c_2(\dot{\theta}_s - \dot{\theta}_{dout}\gamma_d) - \mu_{sg}(F_a - c_{x_1}\dot{x}_s)R_m - T_{sr_i} \tag{4.19}$$

$$J_{gin}'\ddot{\theta}_{gin} = k_1(\theta_m - \theta_{gin}) + c_1(\dot{\theta}_m - \dot{\theta}_{gin}) + T_{spring} + \frac{1}{\gamma_i}\mu_{sg}(F_a - c_{x_1}\dot{x}_s)R_m \tag{4.20}$$

$$J_{r_i}\ddot{\theta}_{r_i} = -k_{rg_i}(\theta_{r_i} - \theta_{g_i}) - c_{rg_i}(\dot{\theta}_{r_i} - \dot{\theta}_{g_i}) - T_{pi0} + T_{sr_i} \tag{4.21}$$

where T_{sr_i} is the torque due to the collision between the guide ring and sleeve, and computed by the impact function [1, 23, 155]:

$$T_{sr_i} = k_{sr}(\theta_s - \theta_{r_i} - n_{s_i}\frac{2\pi}{N} - \theta_2)^n + c_{sr}(\dot{\theta}_s - \dot{\theta}_{r_i}) \tag{4.22}$$

where k_{sr} and c_{sr} are the equivalent stiffness and damping coefficient of collision. N is the number of sleeve prongs. n_{s_i} is a coefficient related to the relative angular displacement between the sleeve and guide ring as well as dog gear, and determines which flat flank of guide ring block or external groove of dog gear will collide with the sleeve prong. $n(= 1.5)$ is nonlinear exponent factor.

Phase 5 ($\theta_3 + \theta' \leqslant \theta_s < \theta_4 + \theta'$): As shown in Fig. 4.6 [1], the prong slides on the chamfer surface of dog gear, and simultaneously rotates the guide ring. It should be noted that the collision between the sleeve prong and guide ring, which starts in the previous phase, will last throughout this and next phase. The motion equations for the DoFs of Harpoon shift can be written as follows:

$$\begin{aligned} J_s'\ddot{\theta}_s &= -k_2(\theta_s - \theta_{dout}\gamma_d) - c_2(\dot{\theta}_s - \dot{\theta}_{dout}\gamma_d) - T_{sr_i} \\ &+ [F_a - (c_{x_1} + c_{x_2})\dot{x}_s]R_m\frac{1 - \mu_s' \tan\beta_2}{\tan\beta_2 + \mu_s'} \end{aligned} \tag{4.23}$$

$$\begin{aligned} J'_{gin}\ddot{\theta}_{gin} &= k_1(\theta_m - \theta_{gin}) + c_1(\dot{\theta}_m - \dot{\theta}_{gin}) + T_{spring} \\ &\quad - \frac{1}{\gamma_i}[F_a - (c_{x_1} + c_{x_2})\dot{x}_s]R_m \frac{1 - \mu'_s \tan\beta_2}{\tan\beta_2 + \mu'_s} \end{aligned} \tag{4.24}$$

$$J_{r_i}\ddot{\theta}_{r_i} = -k_{rg_i}(\theta_{r_i} - \theta_{g_i}) - c_{rg_i}(\dot{\theta}_{r_i} - \dot{\theta}_{g_i}) - T_{pi0} + T_{sr_i} \tag{4.25}$$

where c_{x_2} is the viscous damping.

Similar to the second phase, the sleeve tangential and axial speed are connected on the dog gear chamfer surface, thus its axial acceleration can be calculated by

$$\ddot{x}_s = (\ddot{\theta}_s - \ddot{\theta}_{g_i})R_{out}\cot\beta_2 \tag{4.26}$$

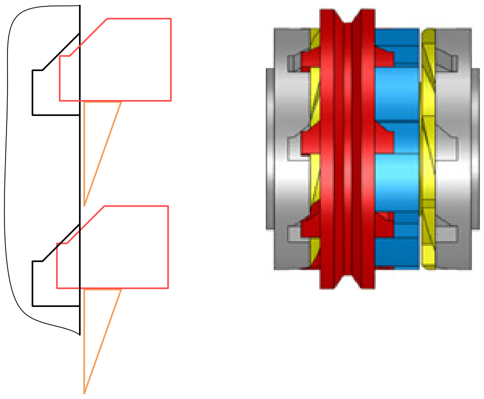

Figure 4.6 : Engaging process of unilateral Harpoon shift: phase 5

Phase 6 ($\theta_4 + \theta' \leqslant \theta_s$ & $\dot{\theta}_{g_i} < \dot{\theta}_s$): Fig. 4.7 [1] demonstrates the sixth phase. Under the shifting force F_a, the sleeve prong continues its axial movement until it contacts the external groove bottom. Simultaneously, the flat flank of prong collide with that of the dog gear external groove. Thus, two collisions occur during this phase: 1) between the prong and guide ring, which started in Phase 4; 2) between the prong and dog gear, and the impact function [1, 23, 155] is used to calculate the collision torques. The dynamics equations are as follows:

$$J_s'\ddot{\theta}_s = -k_2(\theta_s - \theta_{dout}\gamma_d) - c_2(\dot{\theta}_s - \dot{\theta}_{dout}\gamma_d) - T_{sr_i} - T_{sg_i} \tag{4.27}$$

$$J_{gin}'\ddot{\theta}_{gin} = k_1(\theta_m - \theta_{gin}) + c_1(\dot{\theta}_m - \dot{\theta}_{gin}) + T_{spring} + \frac{1}{\gamma_i}T_{sg_i} \tag{4.28}$$

$$J_{r_i}\ddot{\theta}_{r_i} = -k_{rg_i}(\theta_{r_i} - \theta_{g_i}) - c_{rg_i}(\dot{\theta}_{r_i} - \dot{\theta}_{g_i}) - T_{pi0} + T_{sr_i} \tag{4.29}$$

$$m_s\ddot{x}_s = F_a - (c_{x_1} + c_{x_2} + c_{x_3})\dot{x}_s \tag{4.30}$$

where c_{x_3} is the viscous damping. T_{sg_i} is the collision torque between the sleeve and dog gear and can be computed by the impact function [1, 23, 155]:

$$T_{sg_i} = k_{sg}(\theta_s - \theta_{g_i} - n_{s_i}\frac{2\pi}{N} - \theta_5)^n + c_{sg}(\dot{\theta}_s - \dot{\theta}_{g_i}) \tag{4.31}$$

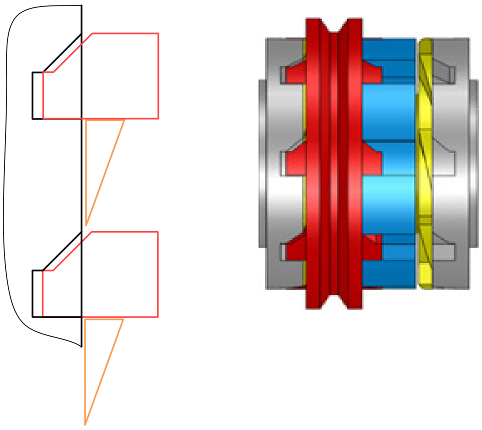

Figure 4.7 : Engaging process of unilateral Harpoon shift: phase 6

Phase 7 ($\theta_5 < \theta_s(\theta_5 \approx \theta_s)$ & $\dot{\theta}_s = \dot{\theta}_{r_i} = \dot{\theta}_{g_i}$): Fig. 4.8 [1] displays the final phase (i.e. locked up phase). The prong touches the external groove bottom, indicating that the sleeve is in the engaged position and physically interlocks with the dog gear, thus $\dot{x}_s = 0$ and $\ddot{x}_s = 0$. During this phase, the dog gear, guide ring, and sleeve rotate at the same speed ($\dot{\theta}_s = \dot{\theta}_{r_i} = \dot{\theta}_{g_i}$). The dynamic equations are expressed as:

$$(J_s' + J_{r_i} + J_{gin}' i_{g_i}^2)\ddot{\theta}_s = [k_1(\theta_m - \theta_{gin}) + c_1(\dot{\theta}_m - \dot{\theta}_{gin})]\gamma_i - k_2(\theta_s - \theta_{dout}\gamma_d) - c_2(\dot{\theta}_s - \dot{\theta}_{dout}\gamma_d) \tag{4.32}$$

For the remaining guide rings, which does not belong to the target gear selected, their motions can be obtained by

$$J_{r_j}\ddot{\theta}_{r_j} = -k_{rg_j}(\theta_{r_j} - \theta_{g_j}) - c_{rg_j}(\dot{\theta}_{r_j} - \dot{\theta}_{g_j}) - T_{pj0}, (j \neq i) \tag{4.33}$$

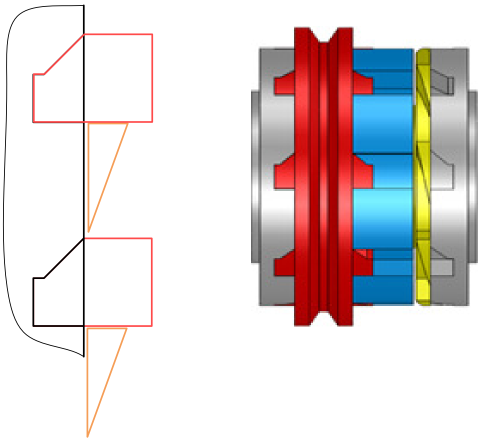

Figure 4.8 : Engaging process of unilateral Harpoon shift: phase 7

4.4 Shifting Quality

In order to quantitatively evaluate the gear shifting quality, jerk is defined as the change rate of vehicle longitudinal acceleration as follows:

$$j = \frac{d^2\nu}{dt^2} = r_w \frac{d^2\dot{\theta}_v}{dt^2} \tag{4.34}$$

where ν is vehicle longitudinal speed, and t is time. As the jerk increases, the vehicle ride comfort becomes worse for passengers [119]. Hence, the recommended value of Germany is $|j| \leqslant 10$ m/s^3 [119].

4.5 Summary

In this chapter, an original dynamic model of an electric vehicle's powertrain system equipped with multi-gear CLAMT is developed to investigate the system's transient characteristics. In this model, the flexibilities of the input and output shafts of the transmission, half shafts and tires are represented by linear spring-dampers. Additionally, a detailed and original dynamic model of unilateral Harpoon-shift synchronizer is established. Harpoon-shift model is then integrated into the powertrain model to study the engaging performance of the synchronizer in terms of shifting jerks of vehicle. It should be pointed out that a substantial proportion of the chapter has been published in [1, 23].

Chapter 5

Gearshift Control of CLAMT

5.1 Introduction

To reduce the shifting shocks and improve driving comfort, a control algorithm is developed in this chapter. Particularly, both the torque and speed profiles are designed based on the modified step function due to its smooth characteristics, for the electric motor to track during shifting.

5.2 Gearshift Control Strategy

The gear shifting strategy for the clutchless AMT mainly includes five steps as follows [23]:

- Motor torque reduction. The motor torque reduces to zero during this stage as shown in Fig. 5.1 [23].
- Synchronizer disengagement. When the motor torque is set to zero, the sleeve of Harpoon shift moves axially from the engaged position to the neutral position under the actuation force F_a.
- Motor speed control. During this stage, the motor actively adjusts the dog gear speed until the speed difference between the shaft and target gear speed reaches the threshold for the Harpoon shift to accomplish engagement successfully. A

speed profile utilizing the step function is designed for the motor to track through a closed-loop control.

- Synchronizer engagement. When the speed difference reaches the threshold, the motor torque is set to zero and then the actuator pushes the sleeve towards the target gear. During the engaging phase of Harpoon shift, the torque springs, which connecting the dog gear and guide ring flexibly, are compressed to transfer the torque through the springs. Thus the dog gear is accelerated quickly and the speed difference reduces dramatically, which helps to decline the shifting shock when sleeve engages the sleeve hub and the dog gear. This process is different from the conventional cone-clutch synchronizer which relies on the friction force to finish the speed alignment.

- Motor torque restoration. After the engagement of Harpoon shift, the drive motor increases its torque to the demand level (see Fig. 5.1.).

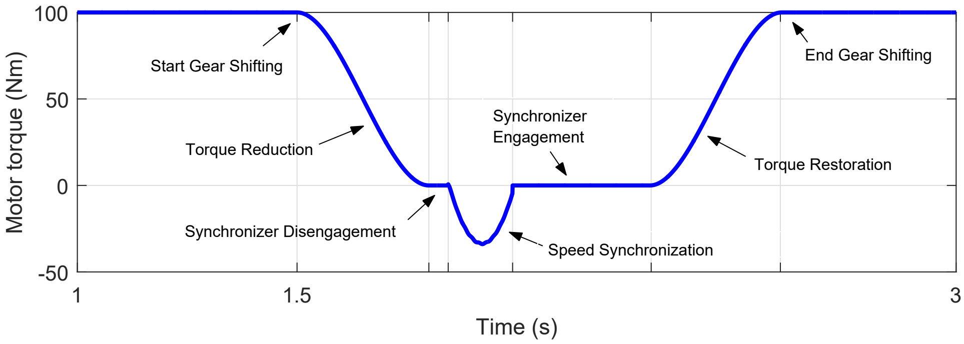

Figure 5.1 : Shifting control of motor torque

From Fig. 5.1, it can be found that the whole shifting duration mainly consists of five parts as mentioned above and the duration is longer than 1 second. However, in the simulation model, the control parameters of the motor torque (or speed) control duration can be modified. Reducing the motor control duration can shorten the overall shifting time. However, if the duration of the torque control phase is too short, the jerk during the phase would increase. Therefore, it is important to find the right compromise between the duration and shifting shock [1].

5.3 Motor Torque Control

The step function (see Appendix A) applied in the impact function presented in the Phase 4 of Section 4.3, is a cubic function and has smooth characteristics [23] . Therefore, in order to achieve a smooth gear changing, specific torque profiles for the torque reduction and reinstatement are proposed based on the step function, as follows

$$T_{mref} = \begin{cases} T \cdot (1 - Step(t, t_{q_0}, t_{q_1}, h_0, h_1)), & \text{Torque reduction} \\ T \cdot Step(t, t_{q_0}, t_{q_1}, h_0, h_1), & \text{Torque re-instatement} \end{cases} \tag{5.1}$$

where $T(= 100$ Nm$)$ is the desired torque, t is the time, t_{q_0} is the time at initiation of the motor torque control, t_{q_1} is the desired duration of torque reduction or re-instatement phase. Here, t_{q_1} is set at 0.3 s.

5.4 Motor Speed Control

This phase is also called active speed synchronization/adjusting. In order to achieve the target speed smoothly, a speed profile ($\dot{\theta}_{g_{iref}}$) based on the step function aforesaid is defined for the motor to track [23], as follows:

$$\dot{\theta}_{g_{iref}} = \begin{cases} \dot{\theta}_{g_{i0}} + (\dot{\theta}_s - \mathit{\Delta}\dot{\theta} - \dot{\theta}_{g_{i0}}) \cdot Step(t, t'_{q0}, t'_{q1}, h_0, h_1), & \text{Downshift} \\ \dot{\theta}_{g_{i0}} + (\dot{\theta}_s - \mathit{\Delta}\dot{\theta} - \dot{\theta}_{g_{i0}}) \cdot (1 - Step(t, t'_{q0}, t'_{q1}, h_0, h_1)), & \text{Upshift} \end{cases} \tag{5.2}$$

where $\mathit{\Delta}\dot{\theta}$ is the speed threshold for the Harpoon shift to start the engagement process. t'_{q0} is the time at initiation of the motor speed control, and t'_{q1} is the desired duration, within which the dog gear speed should be adjusted to the target speed, i.e. $\dot{\theta}_s - \mathit{\Delta}\dot{\theta}$. In this research, t'_{q1} is set at 0.15 s. $\dot{\theta}_{g_{i0}}$ is the dog gear speed of the i-th gear when the motor starts to actively adjust the target gear speed, here $\dot{\theta}_{g_{i0}} = \dot{\theta}_{gin}(t = t'_{q0})/\gamma_i$.

A control algorithm based on PI control is proposed as shown schematically in Fig. 5.2 [23]. The motor adjusts the dog gear speed smoothly according to the speed profile defined by Eq. 5.2 until the speed difference between the target gear and sleeve arrives at the speed threshold $\Delta\dot{\theta}$.

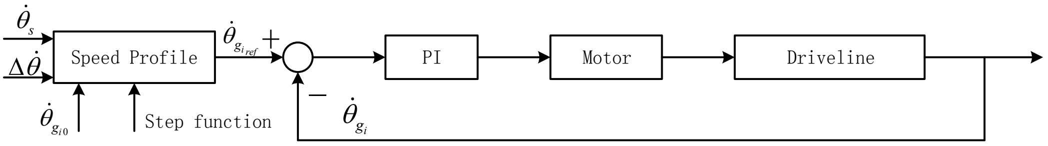

Figure 5.2 : PI control algorithm for adjusting dog gear speed

5.5 Summary

A control strategy for the EV multi-speed CLAMT equipped with unilateral Harpoon-shift synchronizer is proposed in this chapter. In order to achieve a smooth gear change, both the torque and speed trajectories are designed based on a modified step function for the motor torque reduction and recovery control and active speed adjustment during gear shifting. It is worth pointing out that a substantial proportion of this chapter has been published in [1, 23].

Chapter 6

Transient Simulations of an EV Powertrain with Unilateral Harpoon Shift

6.1 Introduction

In this chapter, a simulation model is established using Simulink and Matlab, according to the proposed control strategy and the dynamic models developed in the previous chapters, including the unilateral Harpoon-shift synchronizer mechanism and the powertrain system with a multi-speed CLAMT. Gearshift simulations are performed under different working conditions. The numerical simulation model is used to investigate the powertrain system torsional vibrations during gear change and analyze the impacts of design parameters on the system transients.

6.2 Gearshift Simulation

The simulation model is established in Simulink environment to investigate the powertrain system transient dynamics during gear shifting, and the key parameters of the powertrain model are shown in Table 10.1 [23] (see Appendix C). The numerical solver of ODE45 is applied in the simulation, and the maximum time step is 2×10^{-5} [23]. The solver uses a variable step Runge-Kutta method to numerically solve ordinary differential equations (ODEs) starting from an initial state. During the simulation, the angular speeds and displacements of these DoFs can be obtained at each time step by solving the equations. And these values at the end of each phase can be transmitted to the next phase as its initial state.

Fig. 6.1 [23] displays the speed responses of the upshift and downshift of Harpoon-shift components. As mentioned previously, the precondition for Harpoon shift to engage successfully is that the sleeve speed must be faster than the dog gear speed. Thus, for the case of upshift from the 1st to 2nd gear shown in Fig. 6.1(a), the motor must reduce the target gear (i.e. dog gear 2) speed until it is less than the sleeve speed and the speed difference between the target gear and sleeve satisfies the threshold condition. Then Harpoon shift starts the engagement process. As illustrated in Section 4.3, the torque is transferred to the dog gear when the torque springs are compressed during engaging phases 4 and 5. Therefore, the dog gear 2 is accelerated and its angular speed increases quickly. In this way, the speed difference reduces significantly [23].

It should be noted that if the speed difference cannot be eliminated completely during phases 4 and 5, there will be a collision between the dog gear 2 and sleeve prongs during phase 6 due to the remaining speed discrepancy. When the dog gear 2 speed matches the sleeve speed, the engaging process enters phase 7 (locked-up stage). the speeds of sleeve, guide ring and dog gear 2 are identical in this phase. After the engagement, torsional vibrations may occur due to the acceleration discrepancy between the dog gear 2 and sleeve when Harpoon shift is locked-up [23].

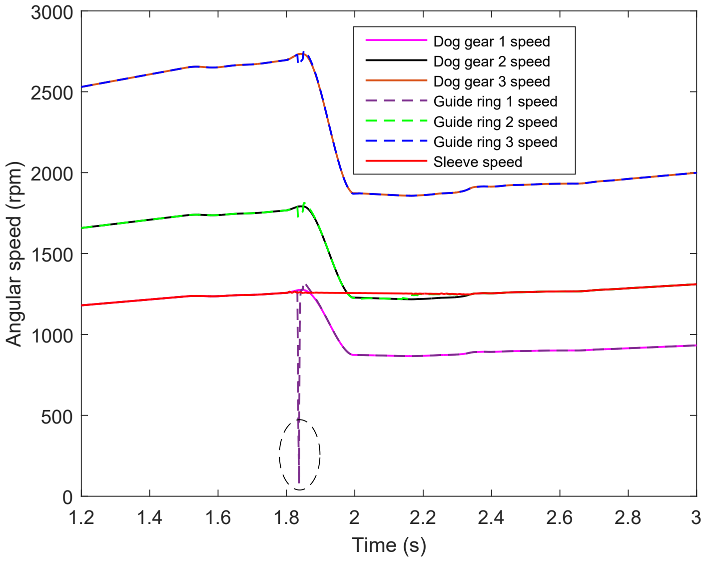

(a) 1st to 2nd gear upshift

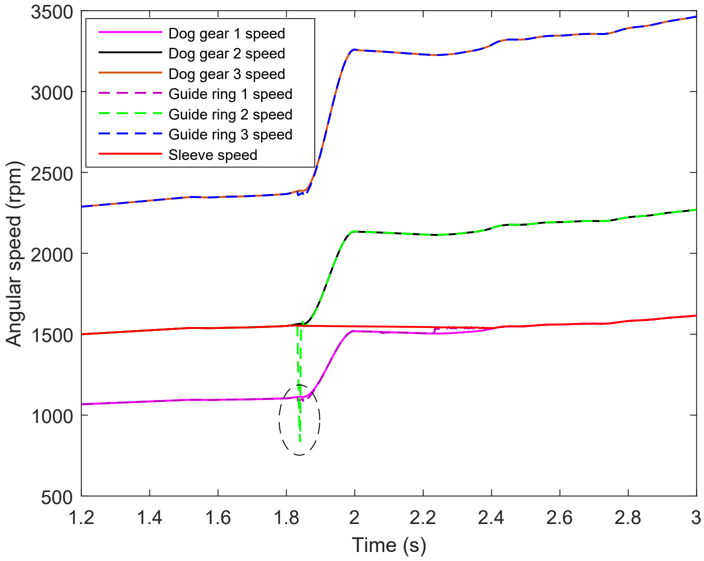

(b) 2nd to 1st gear downshift

Figure 6.1 : Angular speeds of Harpoon-shift rotational DOFs during shifting

As marked in both Fig. 6.1(a) and Fig. 6.1(b), it is interesting to find that the guide ring speed decreases suddenly and then increases quickly before the motor speed control phase starts [23]. This is because when the engaging process finishes, the elastic energy stored in the compressed torque spring will be kept until the next gearshift happens. If next gear shifting starts, the sleeve will move axially from the engaged position to the neutral position, and meanwhile, the guide ring will rotate back to its initial position under the restoring force of the compressed torque spring [1], as shown in Fig. 6.2 [23]. When the guide ring touches the limiting mechanism, i.e. the dog gear inner groove, these two parts will rotate at the same speed as they are fixed together under the spring force due to the pre-compression of the torque springs. In this case, the guide ring covers the dog gear external grooves to prevent premature locking if this gear is chosen again.

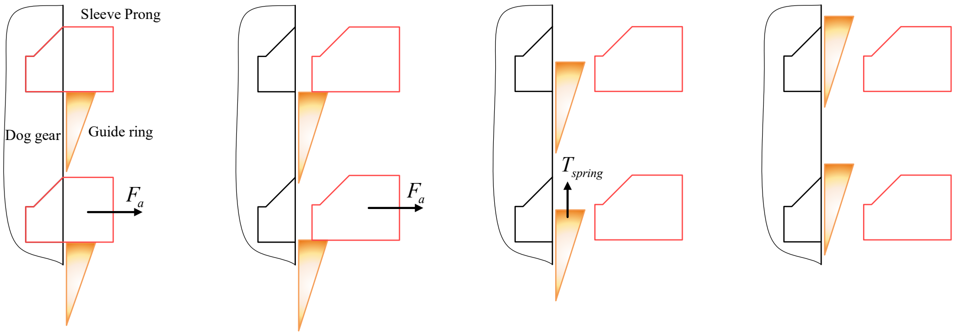

Figure 6.2 : Position of guide ring during disengagement

6.3 Impact of Torque Spring Stiffness

In this section, the study concentrates on investigating the effects of the torque spring stiffness on the torque peak during the engagement. Based on the dynamic model verified by the experiment developed in the next chapter, a range of values of the torque stiffness is chosen to investigate their impacts on the shifting shocks. Finally, the optimized stiffness is obtained according to the torque peak via quantitative analysis based on simulations.

To reduce the jerk during gear shifting, the torque spring stiffness needs to be optimized [23]. In particular, each gear ratio is different for the multi-speed electric vehicles, thus the spring stiffness for each gear should be optimized respectively as the equivalent inertia of the powertrain upstream of the target gear is different [1].

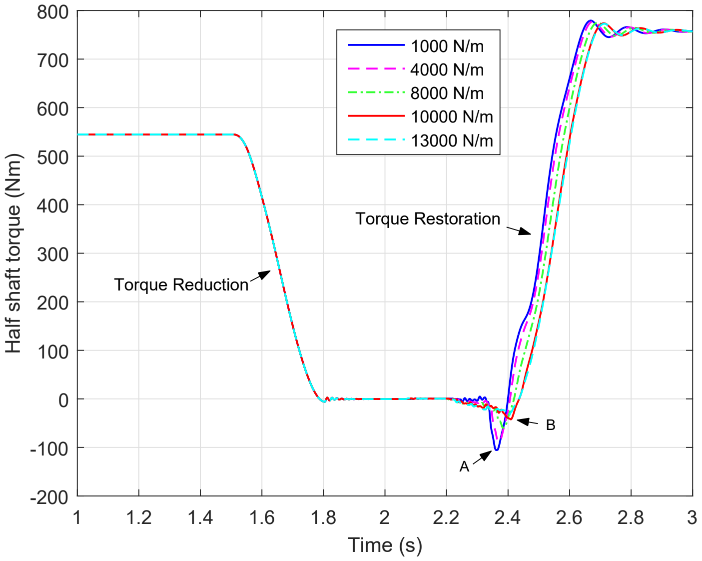

Figure 6.3 : Torque responses of gear shifting from the 2nd to 1st gear under various spring stiffnesses

Fig. 6.3 [23] displays the torque responses of half shaft during gear change from the 2nd to 1st gear under various spring stiffness which has different capacity in transferring the speed difference between the target gear and sleeve into elastic energy used for accelerating the dog gear. If the spring stiffness is too low, the dog gear is accelerated too slowly during the phase 4 and 5 of engagement, leading to large collision torque and shifting shock [23]. For example, in the case of $k_s = 1000$ N/m, the absolute value of torque peak at the engagement point (point A in Fig.

6.3) is 105.5 Nm since the spring stiffness is too low. On the other hand, if the spring stiffness is too high, the dog gear will be accelerated too fast, which may result in the failure of engagement. For instance, the maximum spring stiffness of the 1st gear for Harpoon shift to successfully finish engagement in the simulation is 13000 N/m. Considering that there is no significant difference in terms of torque peak at the engagement point when k_s are 10000 N/m and 13000 N/m, and the absolute value of torque peak is approximately 40 Nm (point B in Fig. 6.3), $k_s = 10000$ N/m is chosen as the optimized spring stiffness for the 1st gear because the spring with lower stiffness can guarantee successful engagement whilst $k_s = 13000$ N/m is the critical value (i.e. the maximum value). From Fig. 6.3, it can also be found that as the spring stiffness increases, the position of point A moves to point B, indicating that engaging duration increases.

Table 6.1 [23] shows that the optimized spring stiffness can greatly reduce the jerk during Harpoon-shift engagement of each gear. This helps to improve the shifting quality but compromises on the engagement duration. For example, the absolute value of jerk at the engagement point during the downshift from the 2nd to 1st gear greatly reduces (from 13.09 m/s^3 to 1.86 m/s^3), while the engaging duration increases from 366.02 s to 408.60 s. In addition, it can be found that the value of optimized spring stiffness increases as the equivalent rotating inertia (related to gear ratio) of the powertrain upstream of target gear increases, and the two have a nonlinear relationship.

Table 6.1 : Comparison of jerk and engaging duration in each gear with optimized and non-optimized spring stiffness

Gear	Gear ratio	Equivalent rotating inertia (kg m^2)	Spring stiffness k_s (N/m)		Engagement duration (ms)		The absolute value of Jerk at the engagement point (m/s^3)	
			Non-optimized	Optimized	Non-optimized	Optimized	Non-optimized	Optimized
1^{st}	2.08	0.175976	1000	10000	366.02	408.60	13.09	1.86
2^{nd}	1.48	0.089094	1000	4000	305.16	343.12	8.76	1.69
3^{rd}	0.97	0.038271	1000	2500	274.68	323.14	7.06	1.76

6.4 Transient Simulations of Multiple Gearshifts

As presented in the previous section, the value of the optimized stiffness for each gear has been obtained through quantitative analysis (see Table 6.1). Then, based on the optimized torque springs, upshift and downshift operations are performed in this section, aiming to investigate the torque response and vehicle jerk during gearshift.

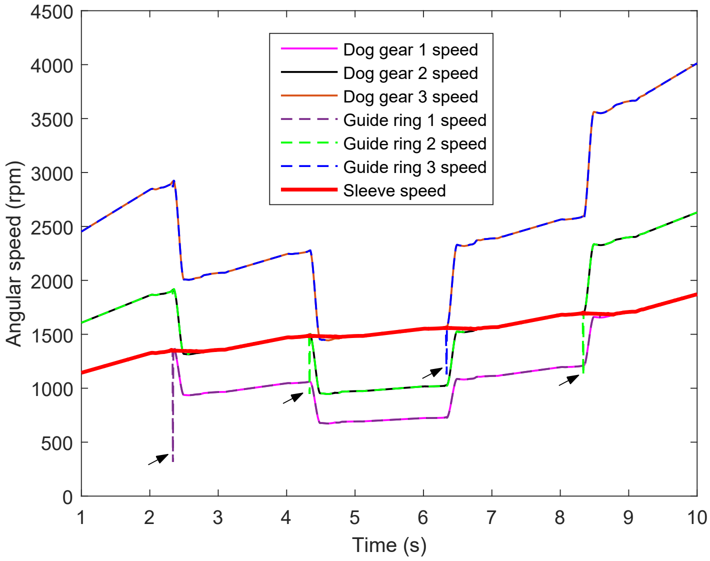

Figure 6.4 : Speeds of Harpoon-shift components with optimized torque spring for the gearshift operation

Fig. 6.4 [23] displays the angular speeds of Harpoon-shift components with the optimized torque spring stiffness. It should be noted that there is a sudden decrement in the guide ring speed during all gear shifting, marked by the arrows in Fig. 6.4. As demonstrated in Fig. 6.2, the torque generated by the restoring force from the torque spring compressed in the current gear rotates the guide ring backward during the sleeve disengagement. Fig. 6.5 [23] shows the gear shifting control signal.

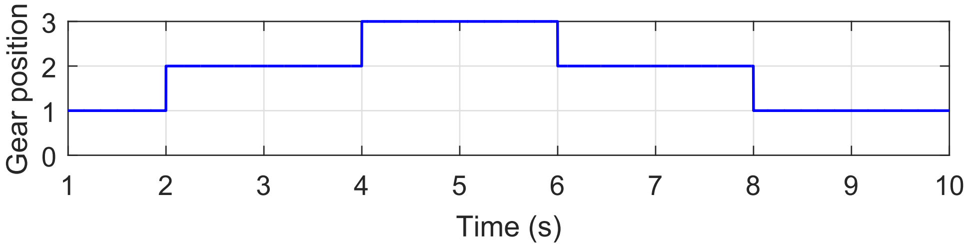

Figure 6.5 : Gear shifting control signal

The comparison of torque responses of Harpoon shift with the non-optimized and optimized spring stiffness is shown in Fig. 6.6 [23]. The non-optimized spring stiffness for each gear is set at 1000 Nm/rad, while the value of the optimized spring stiffness of each gear is different. As shown in Fig. 6.6 and Table 6.2 [23], the torque peaks and the jerks of Harpoon shift with optimized spring stiffness at the engaging point in all gear shifting obviously decrease. This indicates that the stiffness of torque spring plays a significant role in gearshift performance.

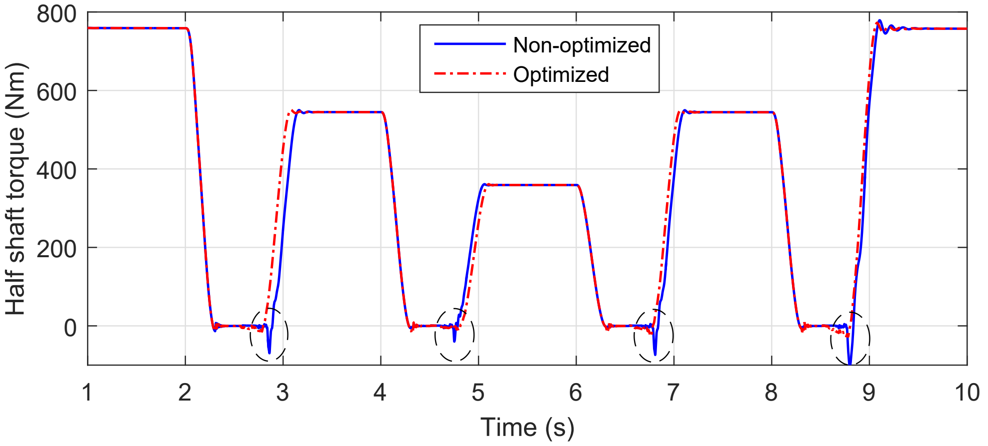

Figure 6.6 : Torque responses of half shaft under different torque spring stiffness for gearshift operations

Table 6.2 : Jerks and torque peaks at the engaging point of each gear shift

Gear shifting	Absolute value of the maximum jerk (m/s^3)		Absolute value of Torque peak (Nm)	
	Non-optimized	Optimized	Non-optimized	Optimized
1st → 2nd	9.66	1.39	69.77	14.92
2nd → 3rd	6.71	1.29	40.05	10.36
3rd → 2nd	10.47	1.80	74.01	26.85
2nd → 1st	12.76	1.44	103.3	28.26

Fig. 6.7 [23] depicts the change of motor torque during gearshift. The maximum output torque of the motor is set at 100 Nm. Fig. 6.8 [23] shows the sleeve axial displacement of each gear during shifting. It is worth pointing out that sometimes the axial movement of sleeve is blocked by the axial limiting mechanism, i.e. the front faces of guide ring and dog gear, which correspond to the position of 5 and 10 mm respectively and that sometimes the prong directly touches the guide ring chamfer surface or the dog gear flat head face. This is determined by the relative position between the guide ring and sleeve. For instance, in all the cases of the upshift and downshift shown in Fig. 6.8, the sleeve does not stop at the position of 5 mm but only stops at 10 mm, indicating that the sleeve prong slips on the chamfer surface. When the sleeve prong touches the external groove bottom of dog gear, it reaches the maximum displacement (18 mm), indicating that Harpoon shift is locked up.

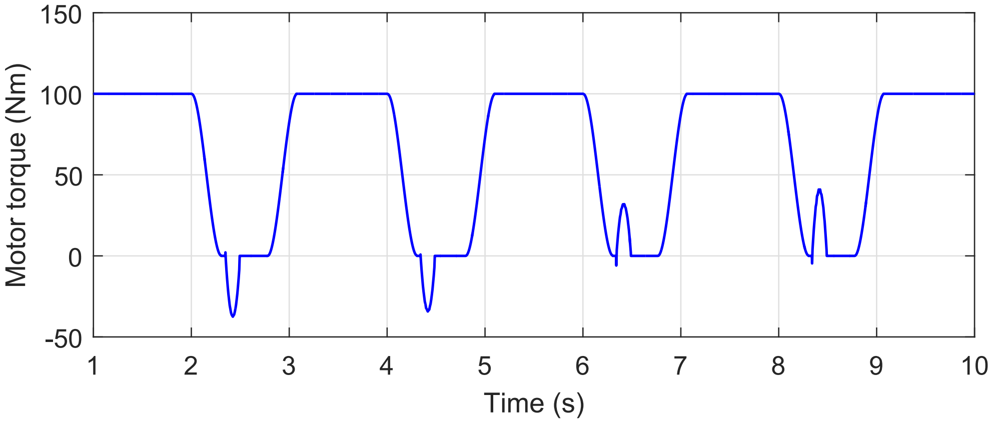

Figure 6.7 : Motor torque for the gearshift operation

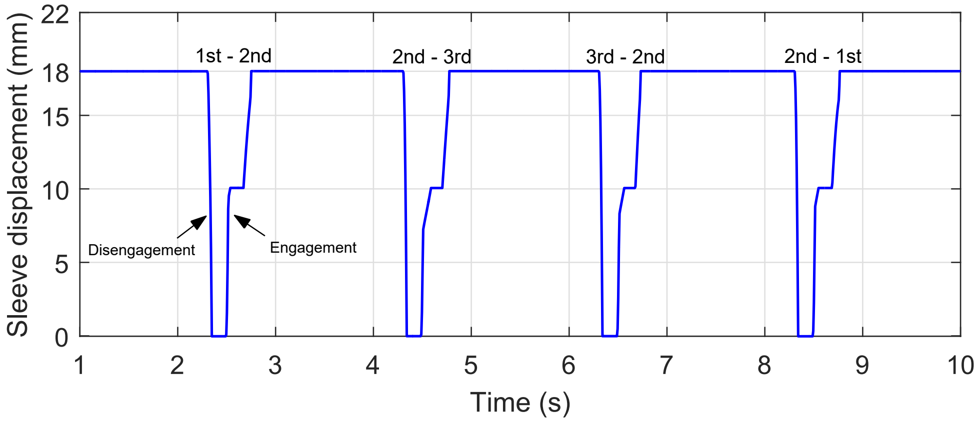

Figure 6.8 : Sleeve axial displacement for the gearshift operation

6.5 Influences of Rotating Inertia and Speed Difference on Gear Shifting Performance

On the basis of the integrated powertrain model built in Chapter 4, research in this section focuses on the influence of rotating inertia and speed difference on the shifting jerk. In order to quantify the impact of these factors on the jerk, the torque restoration is abandoned in the simulation, i.e., the motor torque remains zero after the engagement, because torque restoration also generates jerk [23].

6.5.1 Impact of inertia

This study focuses on the influence of rotating inertia on the jerk during gear shift. The rotating inertia of the drive motor increases from 0.04 to 0.25 kg m^2. The rotating speed of the sleeve is 1550 rpm (i.e. $\dot{\theta}_s$=1550 rpm) and the speed difference between the target gear and sleeve is 30 rpm. The torque transient responses of half shaft during gear shifting from the 2$^{\text{nd}}$ to 1$^{\text{st}}$ gear are shown in Fig. 6.9(a) [23]. As the motor inertia increases, the torque vibration after engagement increases significantly, and the shifting jerk increases as well (see Fig. 6.9(b)) [23]. Table 6.3 [23] displays the engaging duration, maximum jerk, and torque peak after engagement under different motor inertia.

Table 6.3 : Engagement duration, Maximum jerk and torque peak under different motor inertia

Inertia J_m (kg m^2)	Duration of engagement (ms)	Maximum jerk (m/s^3)	Torque peak (Nm)
0.04	404.16	5.17	41.27
0.10	474.40	5.94	72.50
0.15	505.94	6.29	91.40
0.20	524.76	6.69	106.59
0.25	543.52	6.90	118.56

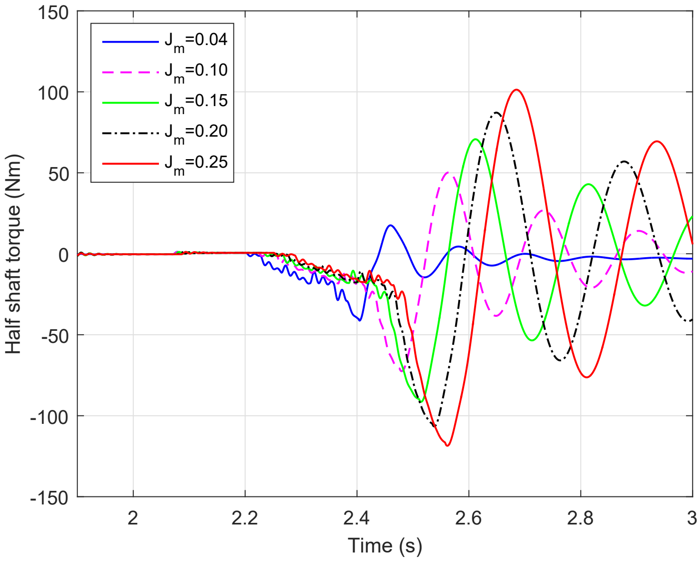

(a) Torque responses of half shaft

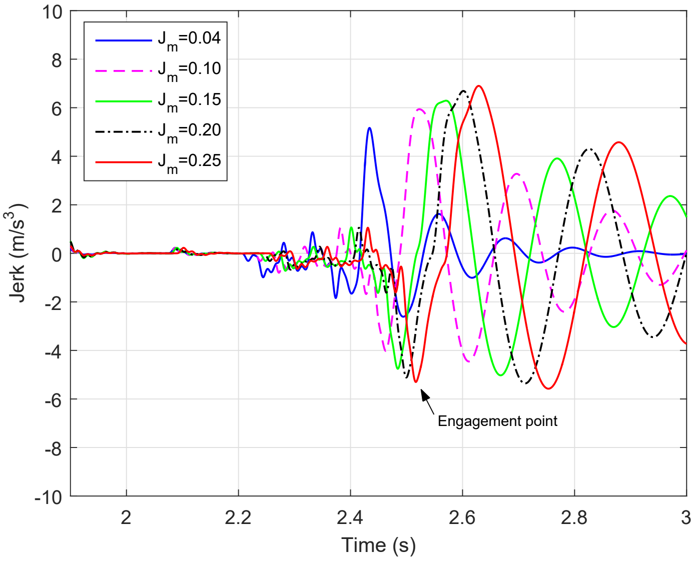

(b) Jerks of vehicle

Figure 6.9 : Torques and jerks during downshift from the 2^{nd} to 1^{st} gear under various motor inertia

Based on the simulation results, a conclusion can be summarized that the equivalent inertia of the powertrain upstream (i.e., from the motor to the target gear) has a significant influence on the shifting shock. To improve the shifting quality, this equivalent inertia should be reduced. Especially, the driving motor should be compact and simultaneously meet the power or torque requirements for the EVs.

6.5.2 Impact of speed difference

The impact of speed difference on the shifting jerk is investigated in this section. The rotating speed of sleeve is 1550 rpm (i.e. $\dot{\theta}_s$=1550 rpm) and the speed differences between the target gear and sleeve are 30, 40, 50 and 60 rpm. The half shaft torque response and shifting jerk under various speed differences are presented in Fig. 6.10 [23]. When the speed difference increases, both the torque vibrational amplitude and the jerk greatly increase; however, the duration of engagement reduces dramatically. This indicates that the speed difference also plays an important role in the gear shifting jerk [23]. Table 6.4 [23] displays the engagement duration, jerk, and torque peak after engagement under various speed differences.

Table 6.4 : Engagement duration, Maximum jerk and torque peak under different speed differences

Speed difference $\Delta\dot{\theta}$ (rpm)	Duration of engagement (ms)	Maximum jerk (m/s^3)	Torque peak (Nm)
30	404.16	5.17	41.27
40	308.64	8.94	75.04
50	243.28	12.44	105.59
60	197.88	15.54	134.35

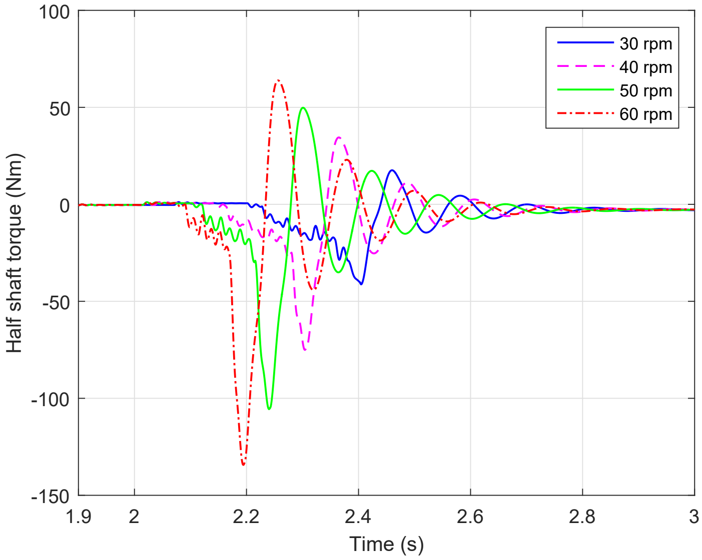

(a) Torque responses of half shaft

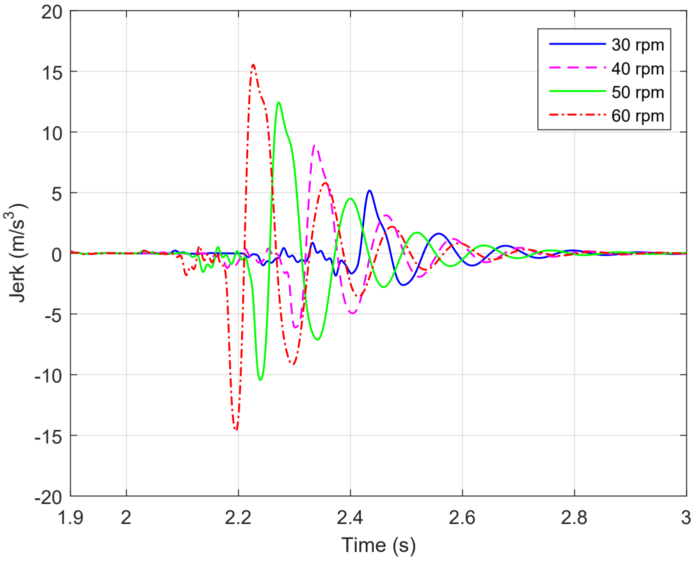

(b) Jerks of vehicle

Figure 6.10 : Torques and jerks during downshift from the 2nd to 1st gear under various speed differences

6.6 Summary

Gear shifting simulations are conducted to study the transient dynamics during Harpoon-shift engagement. Simulation results demonstrate the effectiveness of the integrated model and the control method. Then, based on the proposed model, the torque spring stiffness is optimized to reduce shifting jerk. In addition, the model is adopted to quantitatively study the influence of inertia and speed difference on the torsional vibration of EV driveline systems during the gear shift. Simulation results indicate that in order to improve shifting quality, the torque spring stiffness of Harpoon shift should be respectively optimized according to the powertrain upstream equivalent inertia of the target gear. Additionally, the speed threshold for Harpoon-shift synchronizer to successfully accomplish engagement should be selected carefully. Furthermore, the simulation results demonstrate one of the merits of the proposed Harpoon shift: the shift force during actuation is very small and does not vary with target gear speed, which is desirable for electric vehicles. It should be pointed out that a substantial proportion of the chapter has been published in [23].

Chapter 7

Experiment Development and Results Analysis of Unilateral Harpoon Shift

7.1 Introduction

In this chapter, a testing bench is set up based on a full-scale Harpoon-shift synchronizer. It is used to investigate the transient characteristics of the unilateral Harpoon shift synchronizer and verify the effectiveness of the dynamic model established previously.

7.2 Experiment Development

As shown in Fig. 7.1, the mechanical system of the testing bench is mainly composed of motor, unilateral Harpoon-shift prototype, brake system, and actuator. Considering the Harpoon-shift synchronizer only requires a small shifting force for engagement, a pneumatic cylinder is used as the actuator mechanism in the test, to provide the axial force on the sleeve. Furthermore, a pneumatic valve is employed to control the engaging or disengaging action of Harpoon-shift synchronizer mechanism.

The motor output torque is transmitted to the input shaft of the prototype via a flexible coupling. A torque sensor is utilized to measure the torque response of the Harpoon-shift output shaft, with one side connected with the Harpoon-shift output shaft through a rigid coupling and the other side connected with the input shaft of

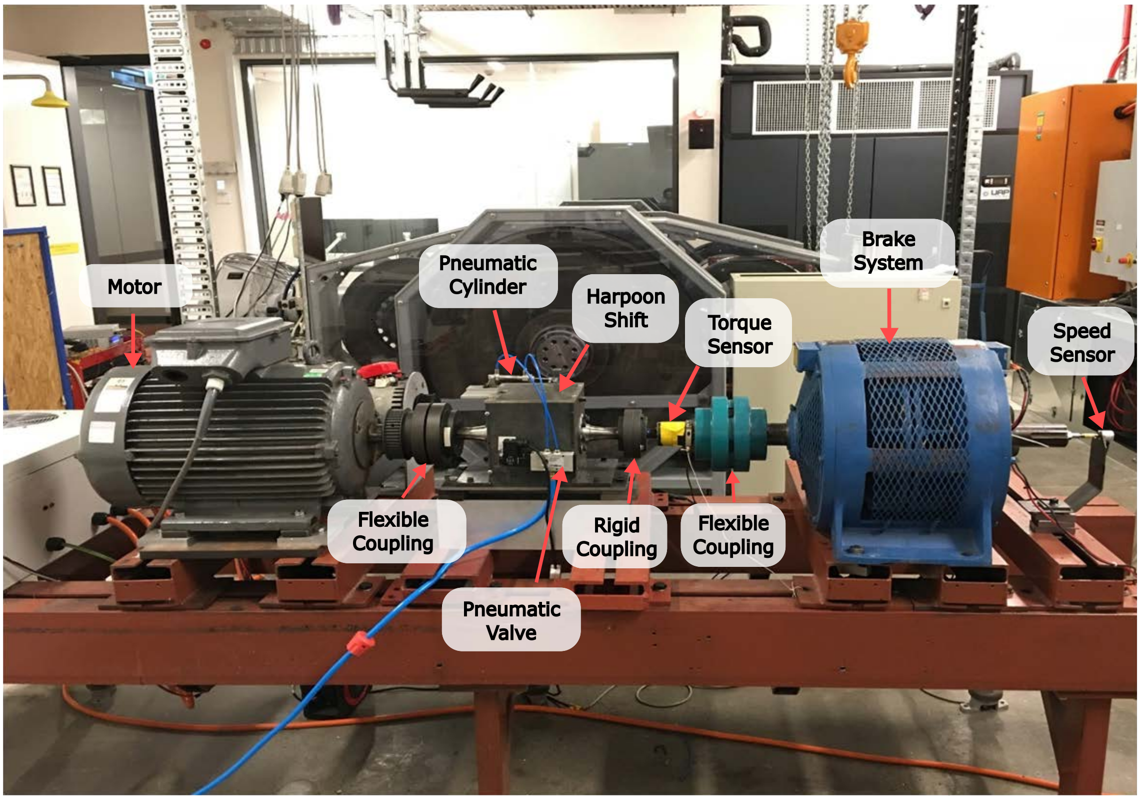

(a) Testing bench of Harpoon-shift synchronizer

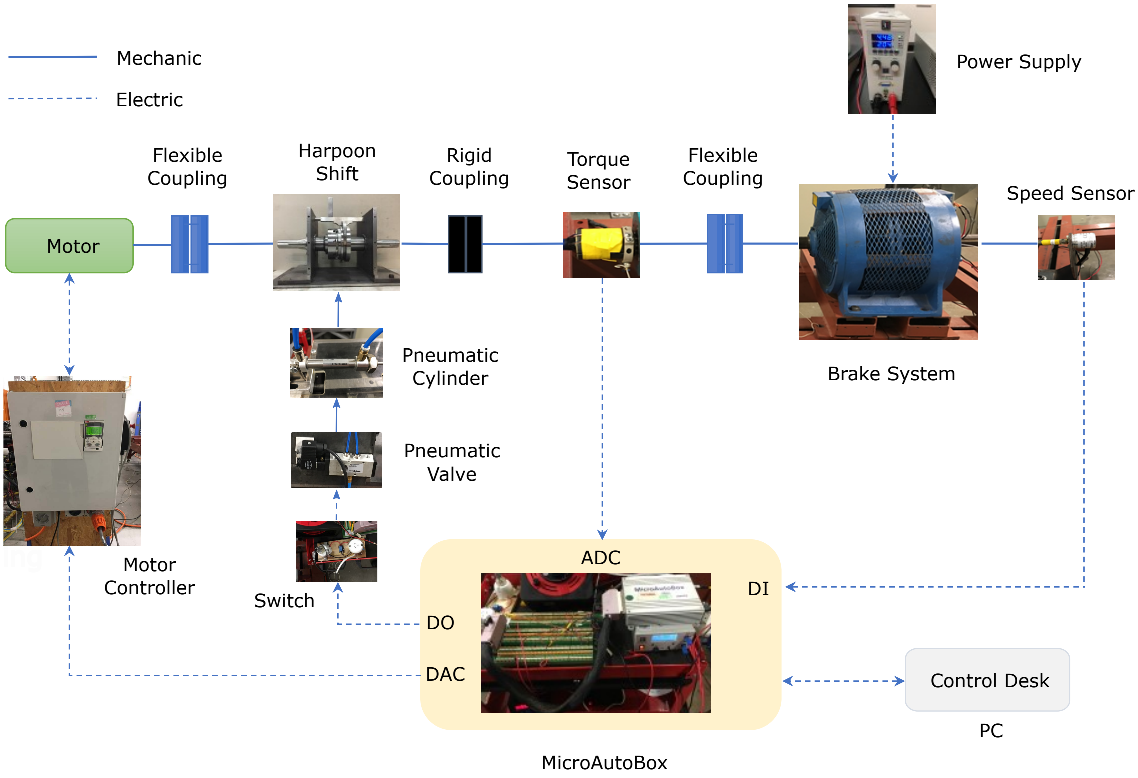

(b) The schematic of testing bench

Figure 7.1 : Testing bench and schematic

the brake system (Eaton Dynamatic) through a flexible coupling (see, Fig. 7.1(a)). In addition, a speed sensor (Kübler encoder: 05.2400.1122.1024), installed on the output shaft of the brake system, is applied to record the speed response during the engagement.

As shown in Fig. 7.1(b), A motor controller is used to regulate the motor rotating speed, which is managed by the MicroAutoBox through a digital to analog converter (DAC). Simultaneously, the MicroAutoBox also electronically manages the switch through digital output (DO) and records the signals from the torque and speed sensor through the analog to digital converter (ADC) and digital input (DI). Then the testing data can be transmitted to the software ControlDesk installed on a personal computer (PC). In addition, the switch controls the pneumatic valve operating mode for the engagement or disengagement of the pneumatic cylinder.

The motor controller can adjust the motor rotating speed dynamically according to the error between the target speed and the actual speed measured by the speed sensor, to guarantee that the engagement is conducted under the desired rotating speed.

It is worth pointing out that a large shifting force is required for the conventional synchronizer to open the guide ring stuck on the gear cone. The force is generally provided by the complicated hydraulic subsystem. Therefore, there may be oscillation for the force due to the complicated control of the subsystem. However, for the proposed Harpoon shift, the shift force will be more stable owing to its simplified control. Furthermore, the torque spring in the proposed synchronizer can absorb the shifting shock to a certain extent. Hence, the torque on the shaft would not be significantly affected even if there is an oscillation on the shifting force. This is one of the advantages of the Harpoon shift over the traditional synchronizer.

7.2.1 Torque sensors calibration

In the experiment, a wireless torque sensor is installed between the output shaft of Harpoon-shift synchronizer and the input shaft of the brake system, to investigate the engaging performance of the synchronizer.

The testing data is transmitted from the signal sender fixed on the rotating shaft to a stationary receiver, as shown in Fig. 7.2(a), while the ATi 2000 series is used to transmit and display the testing data [156]. In addition, energy is provided to the rotating sensor through induction power [156, 157]. The configuration of ATi 2000 series radio telemetry system is shown in Fig. 7.3.

A strain gage in the torque sensor is adhered to the shaft surface to measure the torque, which is not visible in Fig. 7.2. Calibration of the torque sensor should be performed carefully before implementation [157].

As shown in Fig. 7.4, the length of the bar is 0.79 m. A weight is hung on the end of the bar while the other end is rigidly connected with one side of the shaft. Then the torque generated by the weight can be calculated, i.e. $T_s = G \cdot L_{bar} \cdot \cos\theta_{bar}$, where G is the weight, L_{bar} is the length of the bar, θ_{bar} is the turning angular displacement of the bar due to the weight [157]. Fig. 7.5 displays the schematic of torque sensor calibration.

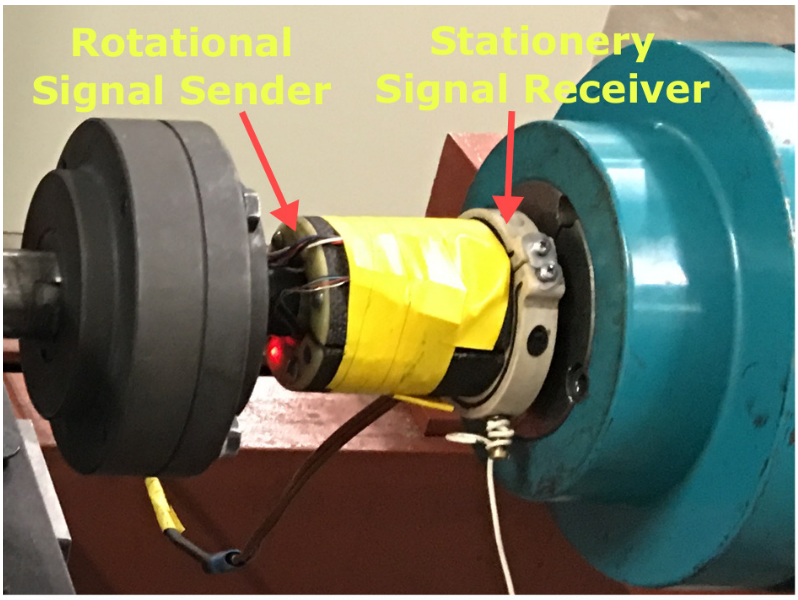

(a) Wireless torque sensor

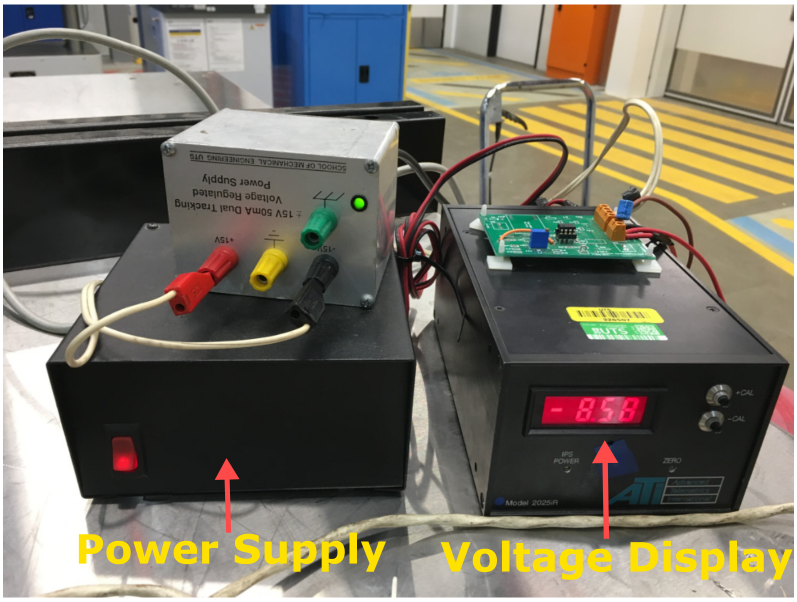

(b) ATi 2025iR digital receiver with backlit LCD

Figure 7.2 : ATi's wireless torque sensing system

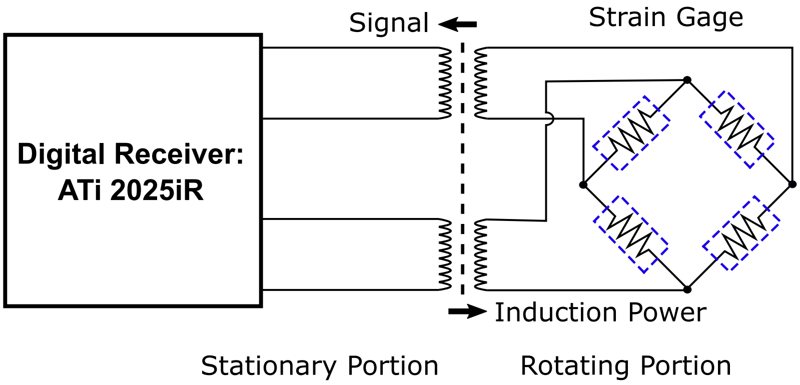

Figure 7.3 : Configuration of ATi 2000 series radio telemetry system

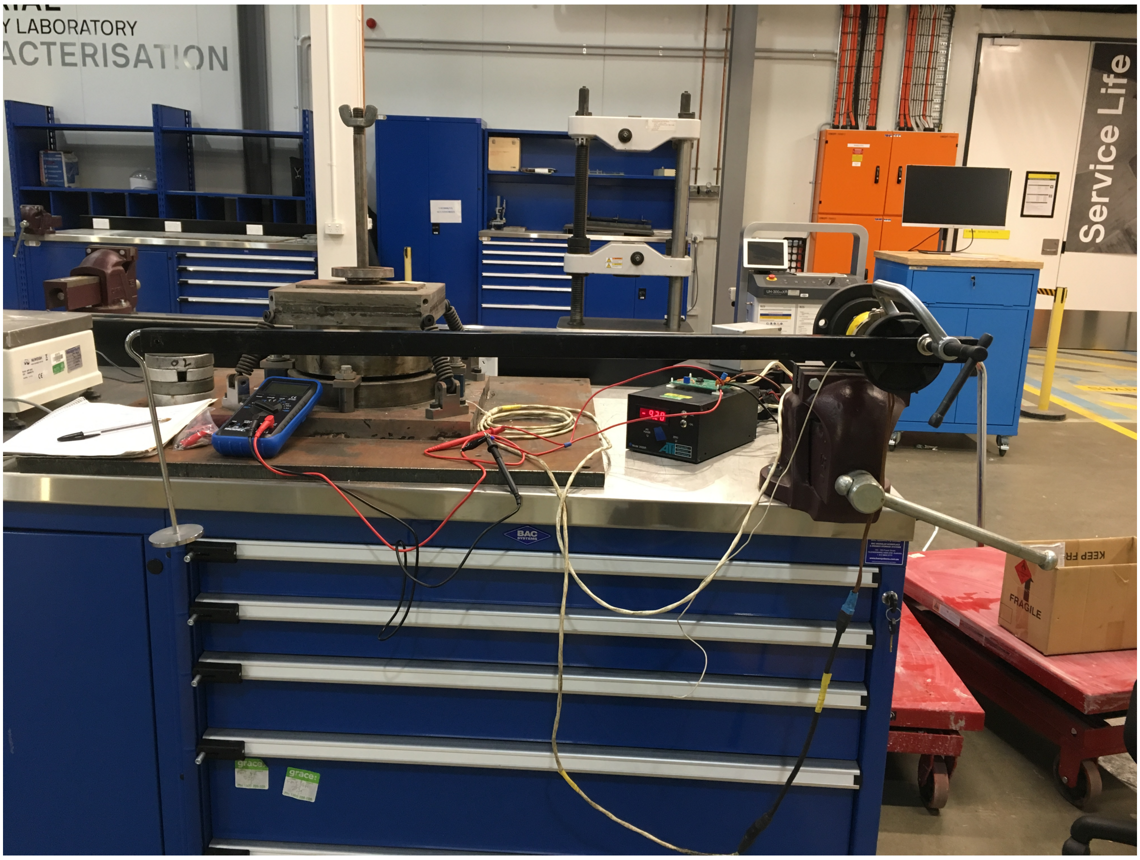

Figure 7.4 : The calibration of torque sensor

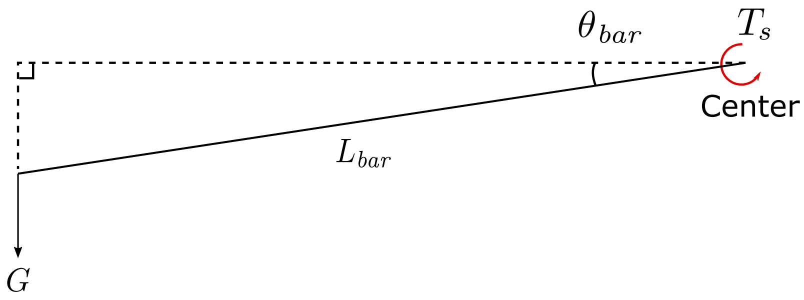

Figure 7.5 : The schematic of torque sensor calibration

The relationship between the voltage and actual torque is displayed in Fig. 7.6, and the raw calibration data is shown in Table 7.1.

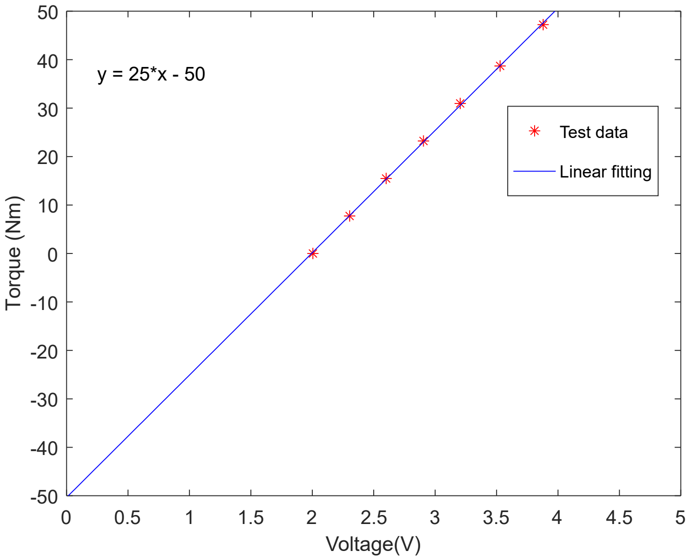

Figure 7.6 : Torque-voltage characteristic of torque sensor

7.2.2 dSPACE control system

The control system of the testing bench for the unilateral Harpoon shift synchronizer is developed through the dSPACE, which includes ControlDesk and MicroAutoBox.

Table 7.1 : Calibration data of torque sensor

Mass (kg)	Torque (Nm)	Voltage (V)
0	0	2.005
1	7.7420	2.304
2	15.4840	2.601
3	23.2260	2.905
4	30.9680	3.204
5	38.7100	3.529
6.1	47.2262	3.879

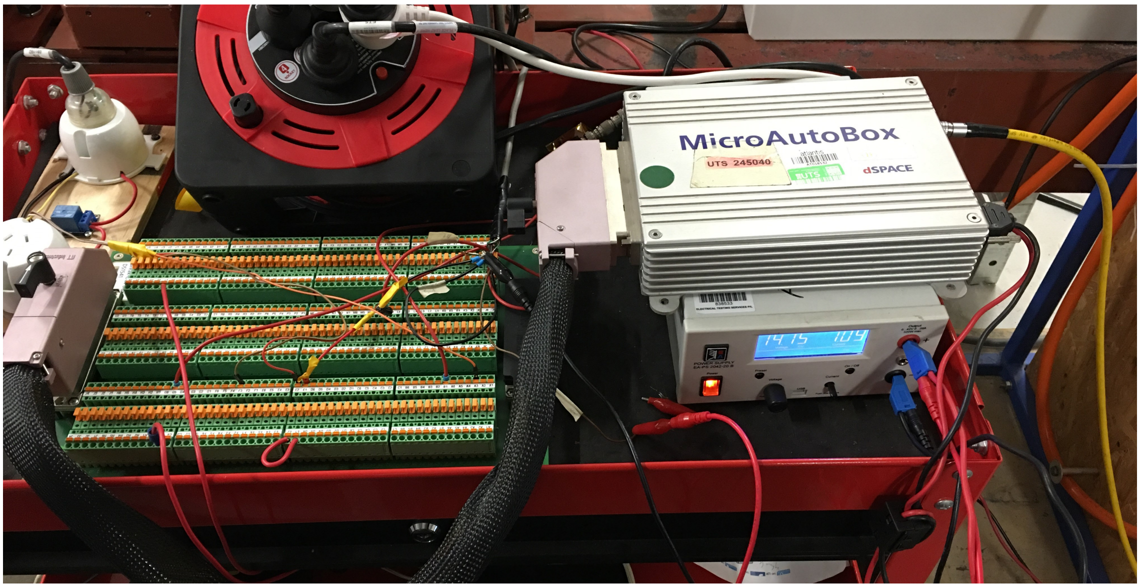

Figure 7.7 : MicroAutoBox and electric control panel

ControlDesk is the dSPACE's experimental software, suitable for seamless electronic control unit (ECU) development, while MicroAutoBox (see Fig. 7.7) is a real-time platform for the applications of rapid control prototyping (RCP), and it can be used for dynamics, motion, and position control, etc [158–160].

The control model is designed using Simulink and the dSPACE Real-Time Interface (RTI), as shown in Fig. 7.8. Then this Simulink model is compiled into code that can run on the dSPACE MicroAutoBox for real-time implementation [158, 159].

For the convenience of acquiring and displaying testing data and modifying control parameters, an interface is designed in ControlDesk, as shown in Fig. 7.9.

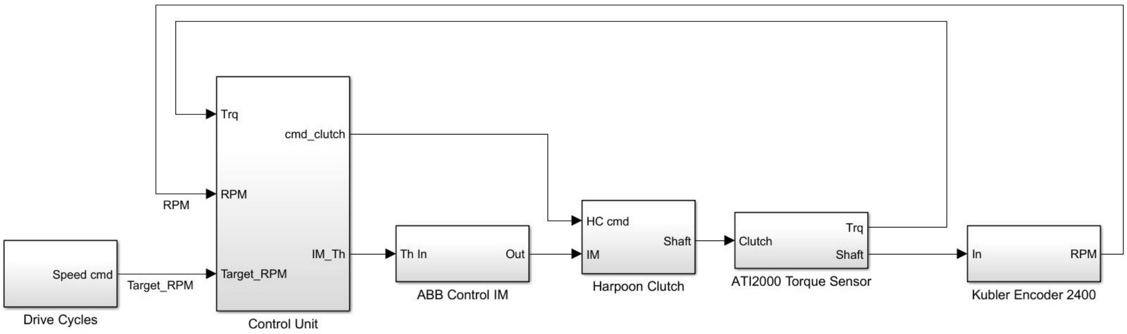

Figure 7.8 : Control model of Harpoon shift

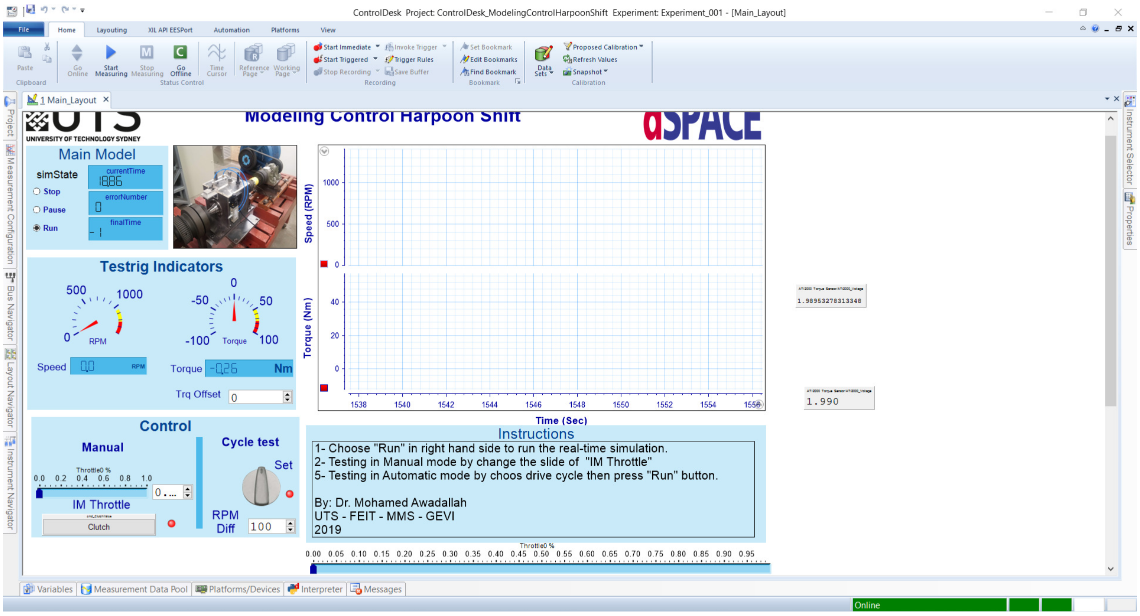

Instructions

1- Choose "Run" in right hand side to run the real-time simulation.
2- Testing in Manual mode by change the slide of "IM Throttle"
5- Testing in Automatic mode by choos drive cycle then press "Run" button.

By: Dr. Mohamed Awadallah
UTS - FEIT - MMS - GEVI
2019

Figure 7.9 : Interface of Harpoon-shift engagement control in ControlDesk

7.3 Experimental Results and Analysis of Unilateral Harpoon Shift Synchronizer

The torque responses of Harpoon shift under the same speed discrepancy ($\varDelta\dot{\theta}$=35 rpm) but different rotating speeds (i.e., 200 and 300 rpm) are displayed in Fig. 7.10. It can be found that there is no significant difference in the torque peaks of the two cases. Thus, a conclusion can be drawn that the rotating speed has no significant effect on the engaging performance of unilateral Harpoon shift.

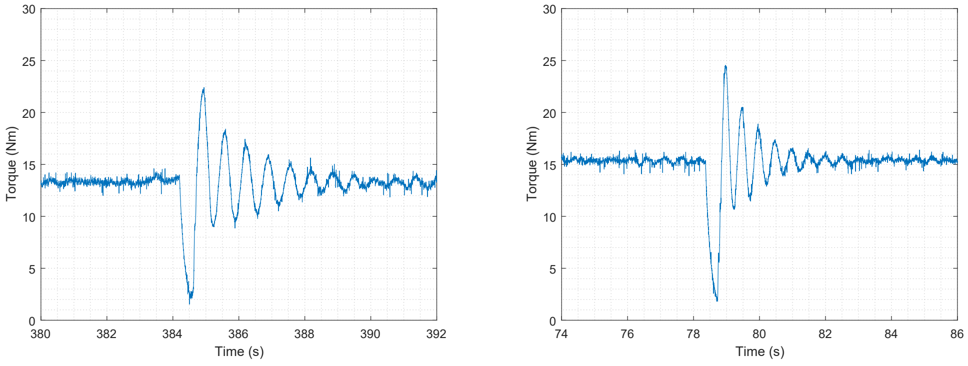

(a) Speed: 200 rpm

(b) Speed: 300 rpm

Figure 7.10 : Torque responses under different rotating speeds

Fig. 7.11 presents the torque responses of Harpoon-shift output shaft during engagement under various speed differences ($\varDelta\dot{\theta}$) from 10 rpm to 55 rpm. The motor speed is 500 rpm. It can be found that as the speed difference increases, the torque peak during engagement increase from 16.5 ($\varDelta\dot{\theta}$=10 rpm) Nm to 33.8 Nm ($\varDelta\dot{\theta}$=55 rpm) . This indicates that the speed difference has a significant influence on the engaging performance of the unilateral Harpoon-shift synchronizer. This conclusion is consistent with that based on the numerical simulation results in the previous chapter.

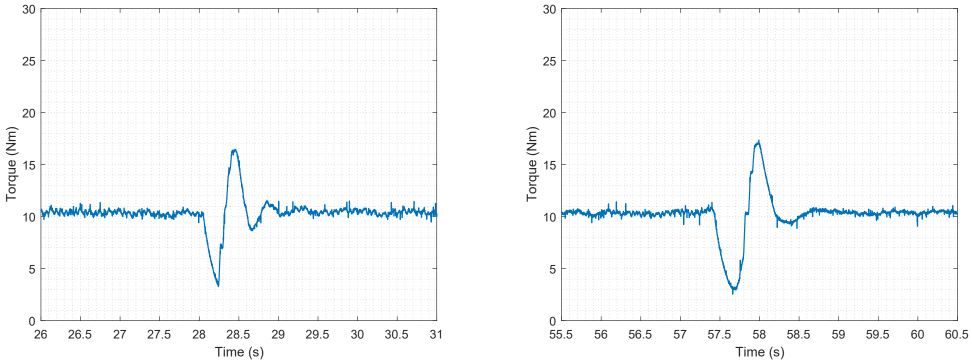

(a) Speed difference: 10 rpm

(b) Speed difference: 20 rpm

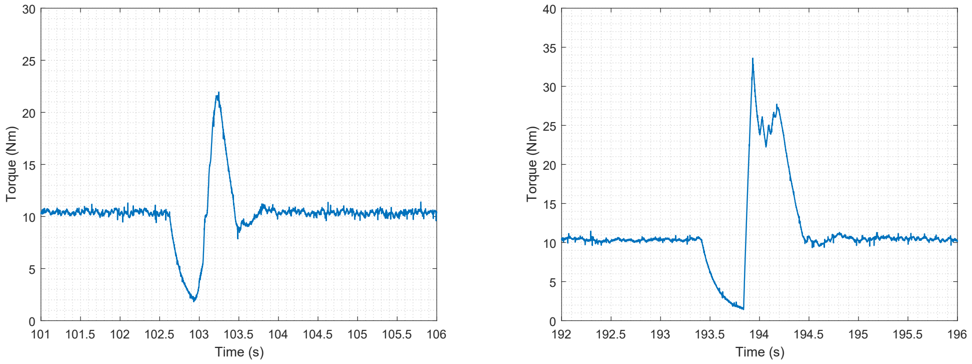

(c) Speed difference: 30 rpm

(d) Speed difference: 55 rpm

Figure 7.11 : Torque responses under various speed differences

7.4 Summary

In this chapter, a testing bench is set up to study the engaging performance of the unilateral Harpoon shift synchronizer. The experiment includes the establishment of the mechanical system, torque sensor calibration, control system, and interface design. The tests under various engaging conditions validate the effectiveness of the established dynamic model of the unilateral Harpoon shift.

Chapter 8

Concept of Bilateral Harpoon-Shift Synchronizer

8.1 Introduction

Traditional synchronizers utilize the friction elements to eliminate speed difference. Consequently, energy losses and frictional wears are inevitable. For these reasons, Zhang and Fang et al. [139] firstly proposed the concept of unilateral Harpoon-shift synchronizer which applies the speed difference to complete engagement rather than the friction torque. However, there are still two drawbacks in this type of synchronizing mechanism. Firstly, it cannot accomplish engagement successfully when the speed difference is small. Secondly, the sleeve rotating speed must be faster than the dog gear, otherwise, the engagement will be failed [23].

This chapter presents a concept of bilateral Harpoon-shift synchronizer for EVs equipped with multi-speed CLAMT, with the purpose of reducing the shifting shocks, simplifying the gearshift control strategy and overcoming one of the biggest shortcomings of the conventional synchronizer, friction losses. Moreover, it avoids the drawbacks of the unilateral Harpoon shift.

8.2 Concept of Bilateral Harpoon-Shift Synchronizer

A new bilateral Harpoon-shift synchronizer (see Fig. 8.1) is proposed in this study as an alternative to traditional synchronizer equipped in the multi-gear transmission of EVs, since there are several serious issues in conventional synchronizer, listed as follows:

- Friction losses and heat dissipation of traditional synchronizers can influence the efficient performance of transmission [4, 144].
- Frictional wear significantly affects the service life and shifting performance of conventional synchronizers [138].
- Under certain circumstances, the guide ring fails to lock out the sleeve and serious tooth hitting will happen if the sleeve collide with the clutch gear before the speed synchronization completes [109, 161].
- In order to separate the guide ring from clutch gear when they are coupled together due to the static frictional torque acting on the cone surfaces, the axial shifting force needs to dramatically increase during engagement, leading to the second bump [22, 119], which has a significant impact on the shifting quality. Thus, the shifting force control during engagement is complicated.

However, for the EVs, the driving motor is able to eliminate most of speed difference through active speed control during gear shift process, due to its high dynamic response characteristics compared to internal combustion engine (ICE), which significantly reduces the need for the friction clutch. Taking into account the issues of the traditional synchronizer mentioned above, a new bilateral Harpoon-shift synchronizer is put forward for the EVs to shorten the torque gap, simplify the control and improve the shift quality and efficiency in this study. The configuration of the bilateral Harpoon-shift synchronizer is simple, consisting of dog gear, guide ring, torque springs, sleeve and hub as shown in Fig. 8.1 and Fig. 8.2(a). The springs are installed in internal grooves on the dog gear, with two sides connecting the guide ring and dog gear respectively, as shown schematically in Fig 8.2(b). The sleeve connects with the output shaft via a splined hub (see Fig. 8.1), and it can only slide axially from the neutral position to the engaged position [1, 109].

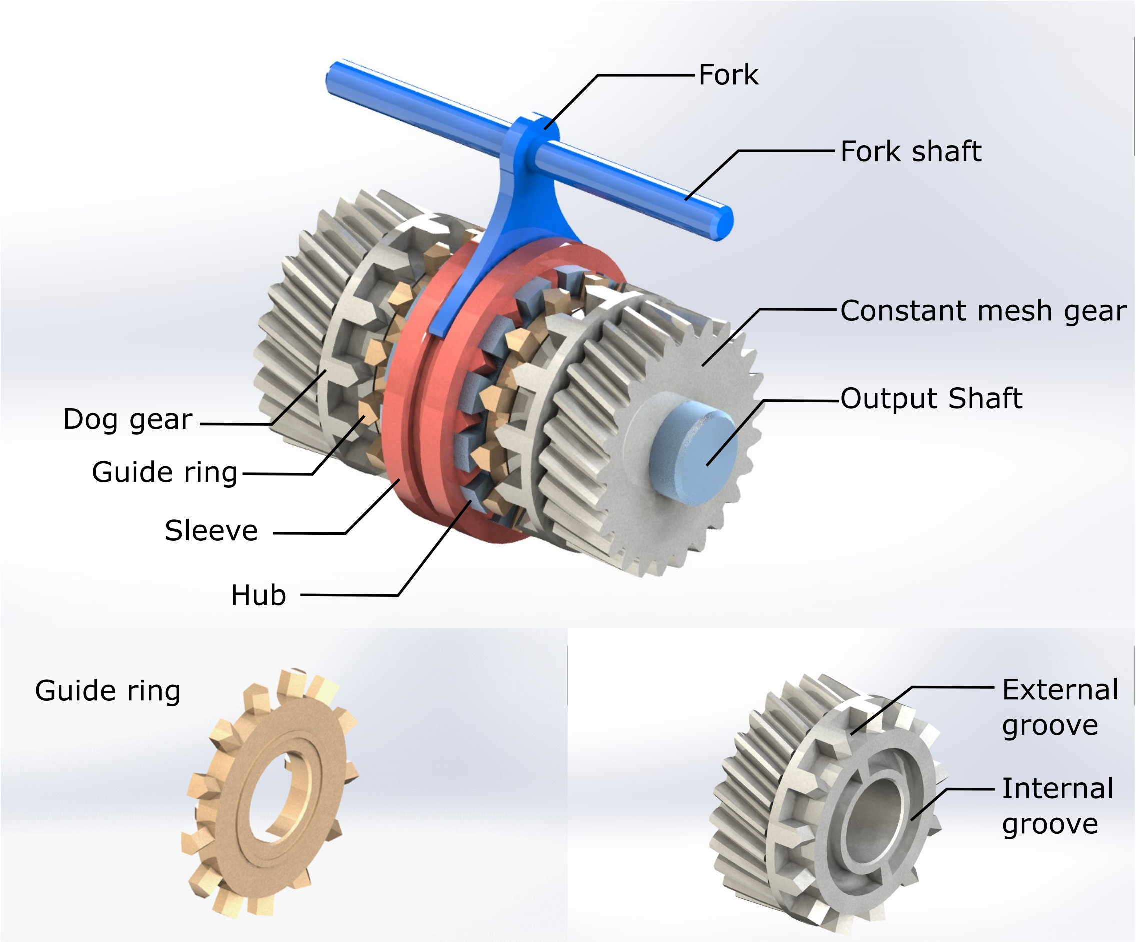

Figure 8.1 : Concept of bilateral Harpoon-shift synchronizer

It should be noted that the sleeve prong, guide ring, and dog gear has a round corner. During the engagement, there is face contact between these components, to

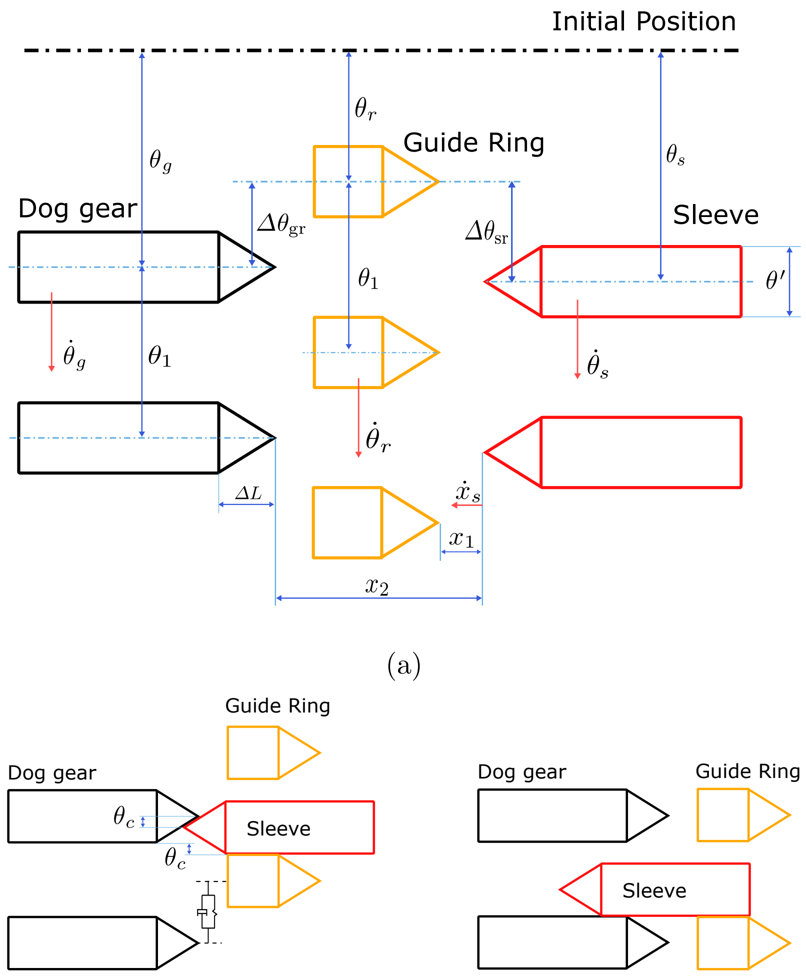

(a)

(b)

Figure 8.2 : Configuration and parameters of bilateral Harpoon-shift synchronizer

avoids excessive wear. Some special characteristics of the proposed bilateral Harpoon shift are listed as follows:

- There are no friction losses during shifting since no frictional elements are used in the new synchronizer. Instead, the dog gear is flexibly connected with the guide ring by springs as shown in Fig 8.2(b). When the sleeve rotates guide ring, the springs are compressed, which helps to absorb the shifting shock and eliminate the speed difference. Therefore, it avoids the influence of the second bump of the traditional synchronizer, because the dog gear and guide ring are not coupled together and not a large shifting force is required to separate the guide ring. Additionally, the bilateral Harpoon shift avoids the failure of locking the sleeve due to the existence of the springs.

- There is a limiting mechanism which allows guide ring rotating certain angular displacement relative to the dog gear, which is slightly more than half of θ_1, i.e. $|\mathit{\Delta}\theta_{rg}|_{\max} = \theta_1/2 + \theta_{gap}$, where θ_{gap} is a constant coefficient with a small value, to guarantee that the sleeve and dog gear are into contact after engagement and the driving torque can be transmitted from the sleeve to the dog gear.

- Compared to the traditional synchronizers, the axial shifting force F_a for the bilateral Harpoon shift is constant and very small, which is only 38 N. Thus this will significantly simplify the control logic and remove the needs for the inefficient and complicated subsystems involved in the shifting process.

- The proposed synchronizer can complete engagement smoothly regardless of whether the sleeve speed is greater or less than the dog gear during upshift or downshift. Thus, it is named bilateral Harpoon shift.

- It has fewer components than the conventional synchronizers. As the friction cone is removed from the Harpoon shift, the manufacturing cost of the proposed synchronizer would be less than that of the conventional counterparts.
- There is a small angular difference between the tooth tips of the sleeve and dog gear when there is flank surface contact between sleeve and guide ring, i.e., θ_c displayed in Fig 8.2(b). This design helps the sleeve teeth to smoothly engage in the external groove of dog gear.

8.3 Summary

In this chapter, a new concept of bilateral Harpoon-shift synchronizer is proposed for the EVs equipped with multi-speed CLAMTs, as an alternative to the conventional cone-clutch synchronizer. At the same time, it overcomes the two weak points of unilateral Harpoon-shift synchronizer as mentioned earlier in this chapter. The bilateral Harpoon shift can complete engagement, whether the sleeve is faster or slower than the dog gear or not, which can further simplify the shift control strategy and shorten the shifting duration as well.

Chapter 9

Dynamic Modeling and Analysis of Bilateral Harpoon Shift

9.1 Introduction

To investigate the engaging performance of the bilateral Harpoon-shift synchronizer mechanism proposed in the previous chapter, a detailed and original dynamic model of the synchronizer is developed in this chapter. Then the bilateral Harpoon-shift model is integrated in the powertrain model established in Chapter 4, to figure out its influence on the transient characteristics of the powertrain system.

Besides, to achieve a smooth gear change, both torque and speed profiles are designed based on a modified step function [23] for the motor to track in the shifting process. Furthermore, the influences of the torque springs and the tooth chamfer angle on the vehicle jerks are quantitatively analyzed and then optimized to improve gearshift quality.

The remainder of the chapter is organized as follows. Section 9.2 is concerned with the modeling of the proposed synchronizer. Section 9.3 the interaction ways of sleeve, guide ring and dog gear during the engagement. Section 9.4 describes the shifting control strategies. Then, simulation results are shown in Section 9.5. At last, Section 9.6 presents the summary of the chapter.

9.2 Modeling of Bilateral Harpoon-Shift Synchronizer

The engagement process can be mainly divided into 6 stages (i.e. Stage 1 - 6), according to the axial position of the sleeve and the rotating speeds of the engaging parts, while Stage 0 represents that the synchronizer stays at the neutral gear. Detailed descriptions of each stage are introduced as follows.

Stage 0 ($x_s = 0$):

The synchronizer is disengaged and the sleeve is in the neutral position. The shifting force F_a is 0 in this phase. Thus the sleeve axial velocity is zero, i.e. $\dot{x}_s = 0$. The dynamic equations of the rotating degrees of freedom (DOFs, as shown in Fig 8.2(a)) of this stage are the same as Stage 1.

Stage 1 ($0 < x_s \leqslant x_1$):

During this stage, the sleeve slides axially toward the dog gear under the axial shift force F_a (=38 N). When the sleeve tooth arrives at the guide ring flat head face (i.e. x_1 in Fig 8.2(a)), the engaging process enters the next stage. The motions can be described by the following formulas:

$$J'_s\ddot{\theta}_s = -T_{slout} \tag{9.1}$$

$$J_r\ddot{\theta}_r = -T_{rg} - D \cdot T_{pre} \tag{9.2}$$

$$J'_{gin}\ddot{\theta}_{gin} = T_{gin} + \frac{1}{\gamma_i}(T_{rg} + D \cdot T_{pre}) \tag{9.3}$$

$$m_s\ddot{x}_s = F_a - c_a\dot{x}_s \tag{9.4}$$

where

$$T_{slout} = k_2(\theta_s - i_d\theta_{dout}) + c_2(\dot{\theta}_s - \gamma_d\dot{\theta}_{dout}) \tag{9.5}$$

$$T_{rg} = k_{rg}(\theta_r - \theta_g) + c_{rg}(\dot{\theta}_r - \dot{\theta}_g) \tag{9.6}$$

$$T_{gin} = k_1(\theta_m - \theta_{gin}) + c_1(\dot{\theta}_m - \dot{\theta}_{gin}) \tag{9.7}$$

$$\theta_g = \theta_{gin}/\gamma_i, \ \dot{\theta}_g = \dot{\theta}_{gin}/\gamma_i \tag{9.8}$$

in the equations, θ_g and θ_r represent the angular displacement of current gear and guide ring, while $\dot{\theta}_g$ and $\dot{\theta}_r$ are their angular speed, respectively. T_{pre} stands for the torque generated by the pre-compression of torque springs. D is a variable representing the status of compressed torque springs. Here, D is based on a modified step function [23] to add the spring torque T_{pre} on the guide ring and dog gear smoothly, as follows:

$$D = \begin{cases} Step(|\varDelta\theta_{gr}|, 0, \theta_{q_1}, h_0, h_1) & \theta_r > \theta_g \\ 0 & \theta_r = \theta_g \\ -Step(|\varDelta\theta_{gr}|, 0, \theta_{q_1}, h_0, h_1) & \theta_r < \theta_g \end{cases} \tag{9.9}$$

where $|\varDelta\theta_{gr}|$ is the absolute value of the difference in angular displacement between the dog gear and guide ring (see Fig. 8.2(a)). θ_{q_1} is a constant corresponding to the maximum value of step function, i.e., h_1.

Stage 2 ($x_1 < x_s \leqslant x_1 + 2\varDelta L$):

In this phase, the sleeve tooth contacts with upper or lower teeth chamfer of guide ring or directly pass through the guide ring teeth without chamfer contact. If the chamfer contacts happen, the sleeve starts to rotate the guide ring and compress the torque spring. To model these discrete state transitions, a variable S_1 ($S_1 =$

$-1, 1$ or 0, see Eq. 9.24) is used in the dynamic equations, and its value depends on the interaction ways between the sleeve and guide ring. The dynamic equations are shown as follows:

$$J_s'\ddot{\theta}_s = -T_{slout} - S_1 \cdot F_t R_m \tag{9.10}$$

$$J_r\ddot{\theta}_r = -T_{rg} + S_1 \cdot F_t R_m - D \cdot T_{pre} \tag{9.11}$$

$$J_{gin}'\ddot{\theta}_{gin} = T_{gin} + \frac{1}{\gamma_i}(T_{rg} + D \cdot T_{pre}) \tag{9.12}$$

where F_t is the tangential force (see Appendix B) acting on the chamfer surface. If tooth chamfer contact happens, there is a speed constraint relationship between the sleeve axial movement and relative rotation, i.e. $\dot{x}_s = (\dot{\theta}_s - \dot{\theta}_r)R_{out}\cot\beta$, where R_{out} is the outside radius of the guide ring and dog gear [23], β is the tooth chamfer angle (see Appendix B).

Stage 3 ($x_1 + 2\varDelta L < x_s \leqslant x_2$):

In this phase, the sleeve collides with the upper or lower flank surface of the guide ring or directly passes through it. If the collision occurs, the sleeve turns the guide ring and compress the torque spring. Similar to Stage 1, in order to represent these discrete state transitions, a variable S_2 ($S_2 = -1, 1$ or 0, see Eq. 9.24) is used in the dynamic equations. Besides, in order to model the collision dynamics, the impact function [1, 23, 155] is employed to calculate the contact force. The motion equations regarding this phase are expressed as

$$J'_s\ddot{\theta}_s = -T_{slout} - S_2 \cdot T_{sr} \tag{9.13}$$

$$J_r\ddot{\theta}_r = -T_{rg} + S_2 \cdot T_{sr} - D \cdot T_{pre} \tag{9.14}$$

$$J'_{gin}\ddot{\theta}_{gin} = T_{gin} + \frac{1}{\gamma_i}(T_{rg} + D \cdot T_{pre}) \tag{9.15}$$

$$m_s\ddot{x}_s = F_a - c_a\dot{x}_s \tag{9.16}$$

where T_{sr} is the collision torque, here $T_{sr} = k_{sr}q_{sr}^n + c_{sr}\dot{q}_{sr}$, where q_{sr} and $\dot{q}_{sr}$ represent the relative penetration depth and the relative normal contact speed between the sleeve and guide ring, respectively. n is the nonlinear exponent factor. k_{sr} and c_{sr} are the equivalent stiffness and damping coefficients, respectively [23].

Stage 4 $(x_2 < x_s \leqslant x_2 + 2\mathit{\Delta} L)$:

Sleeve tooth chamfer contacts with the dog gear chamfer, and simultaneously its tooth flank contacts the guide ring tooth flank. When the sleeve rotates the guide ring gradually, the compressed spring, as well as damping, can absorb the torsional shock and slow the sleeve axial motion, which helps to prevent premature engagement. Similarly, a variable S_3 (defined in Eq. 9.24) is used in equations to represent the discrete states of the tooth chamfer contacts, as follows:

$$J'_s\ddot{\theta}_s = -T_{slout} - S_2 \cdot T_{sr} - S_3 \cdot F_tR_m \tag{9.17}$$

$$J_r\ddot{\theta}_r = -T_{rg} + S_2 \cdot T_{sr} - D \cdot T_{pre} \tag{9.18}$$

$$J'_{gin}\ddot{\theta}_{gin} = T_{gin} + \frac{1}{\gamma_i}(T_{rg} + D \cdot T_{pre}) + S_3 \cdot F_tR_m \tag{9.19}$$

Similar to Stage 2, there is also a constraint relationship between the sleeve axial motion and relative rotation if tooth chamfer contact happens, i.e., $\dot{x}_s = (\dot{\theta}_s -$

$\dot{\theta}_g)R_{out}\cot\beta$.

Stage 5 ($x_2 + 2\varDelta L < x_s \leqslant x_{max}$) :

When the sleeve overcomes the spring force and opens the guide ring, it moves through the dog gear. During this phase, the sleeve contacts the upper or lower flank of dog gear or directly engages the gear without contact. A variable S_4 (Eq. 9.24) is applied to represent the state of the flank contacts. The motion equations are the followings:

$$J_s'\ddot{\theta}_s = -T_{slout} - S_2 \cdot T_{sr} - S_4 T_{sg} \tag{9.20}$$

$$J_r\ddot{\theta}_r = -T_{rg} + S_2 \cdot T_{sr} - D \cdot T_{pre} \tag{9.21}$$

$$J_{gin}'\ddot{\theta}_{gin} = T_{gin} + \frac{1}{\gamma_i}(T_{rg} + D \cdot T_{pre}) + S_4 \cdot T_{sg} \tag{9.22}$$

$$m_s\dot{x}_s = F_a - c_a\dot{x}_s - F' \tag{9.23}$$

where F' is the reaction force when the sleeve teeth contact with the groove bottom of dog gear, namely, sleeve arrives to the maximum position x_{max}. T_{sg} is the torque due to the collision between the sleeve and dog gear, here $T_{sg} = k_{sg}q_{sg}^n + c_{sg}\dot{q}_{sg}$, k_{sg} and c_{sg} are the equivalent stiffness and damping coefficients, respectively. q_{sg} and $\dot{q}_{sg}$ represent the relative penetration depth and the relative normal contact speed between the sleeve and dog gear, respectively.

The variables $S_i (i = 1, 2, 3, 4)$ used in Stage 2, 3, 4 and 5 are defined as follows:

$$S_i = \begin{cases} 1 & \text{Upper side contact} \\ 0 & \text{No contact} \\ -1 & \text{Lower side contact} \end{cases} , i = 1, 2, 3, 4 \tag{9.24}$$

where $i = 1$ represents the contact of tooth chamfers between the sleeve and guide ring, $i = 2$ denotes the contact of tooth flank between the sleeve and guide ring, $i = 3$ stands for the contact of tooth chamfers between the sleeve and dog gear, $i = 4$ represent the contact of tooth flank between the sleeve and dog gear. Fig. 9.1 displays the contact states between the engaging parts.

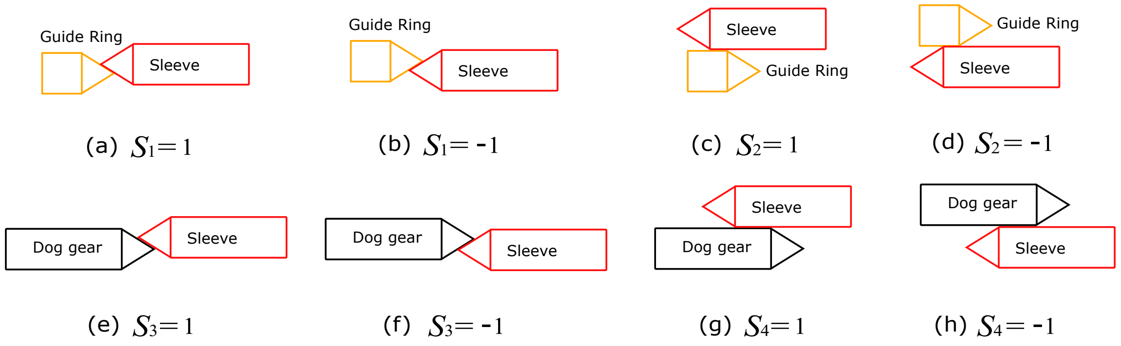

(a) $S_1 = 1$ (b) $S_1 = -1$ (c) $S_2 = 1$ (d) $S_2 = -1$

(e) $S_3 = 1$ (f) $S_3 = -1$ (g) $S_4 = 1$ (h) $S_4 = -1$

Figure 9.1 : Contact states between sleeve, guide ring and dog gear

Stage 6 ($\dot{\theta}_g = \dot{\theta}_s = \dot{\theta}_r \ \wedge \ x_s = x_{max}$) :

In this stage, the sleeve arrives at the maximum displacement x_{max}, where $\dot{x}_s = 0$. And the rotating speeds of the dog gear, guide ring and sleeve are identical, indicating that the engaging process completes. The motion equations are the followings:

$$[J'_{gin} + \frac{1}{\gamma_i^2}(J'_s + Jr)]\ddot{\theta}_{gin} = T_{gin} - \frac{1}{\gamma_i}T_{slout} \tag{9.25}$$

$$\dot{\theta}_r = \dot{\theta}_s = \frac{1}{\gamma_i}\dot{\theta}_{gin} \tag{9.26}$$

9.3 Interaction Ways of Sleeve, Guide Ring and Dog Gear

The interaction ways of the sleeve, guide ring, and dog gear are determined by their relative position and angular speed. Fig. 9.2 shows the transition modes during the engaging process. And the state constraints for each interaction case are described in Table 9.1.

Stage 0: when the speed difference reaches a threshold ($\varDelta\dot{\theta}$) after the active synchronous phase, the transition condition z_0 is triggered, and the engaging state switches from Stage 0 to Stage 1, indicating that the engagement process starts. In this study, a variable $\mathcal{L}$ (=1) is used to represent that the gear change signal is generated.

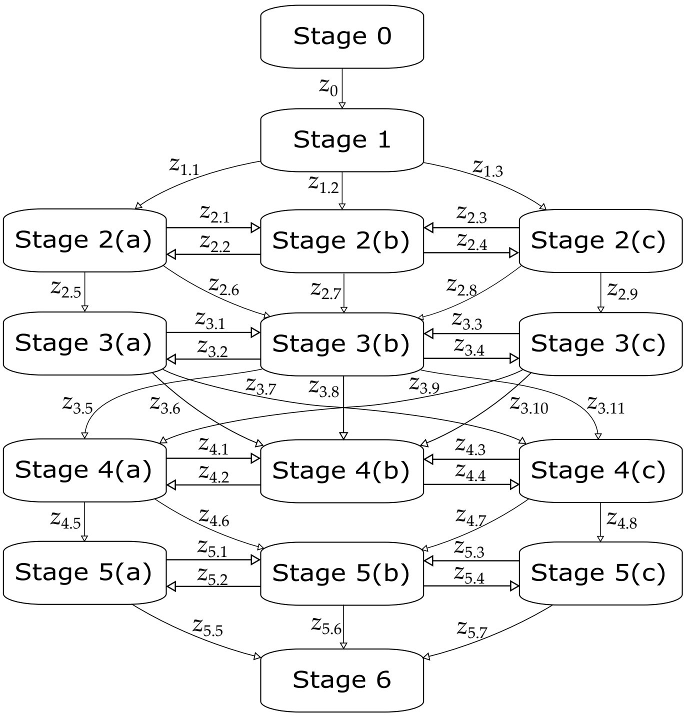

Figure 9.2 : Interaction ways during engagement

Stage 2: if the sleeve teeth contact with the lower or upper tooth chamfers of the guide ring, transition condition $z_{1.1}$ or $z_{1.3}$ is triggered and the engaging state switches from Stage 1 to Stage 2(a) or 2(c). When the sleeve spline aligns the tooth groove of the guide ring exactly, no tooth chamfer contact happens. Then $z_{1.2}$ is triggered, and the state switches to Stage 2(b). If there is no contact on the tooth chamfers, $z_{2.1}$ or $z_{2.3}$ is triggered, and Stage 2(a) or 2(c) switches to Stage 2(b). If sleeve teeth contact with the tooth chamfers of guide ring again, then $z_{2.2}$ or $z_{2.4}$ is triggered.

Stage 3: when the sleeve collides with the lower flank surface of the guide ring, $z_{2.5}$ is triggered and the state switches from Stage 2(a) to Stage 3(a). When the sleeve collides with the upper flank surface, $z_{2.9}$ is triggered and the state switches from Stage 2(c) to Stage 3(c). If no collision happens, $z_{3.1}$ or $z_{3.3}$ is triggered and the state switches to Stage 3(b). If this collision happens again, then the state switches to Stage 3(a) or 3(c) according to the transition conditions $z_{3.2}$ or $z_{3.4}$, respectively.

Stage 4: when the sleeve teeth reach the flat head face of dog gear teeth, i.e. x_2, the interaction ways are the followings: (i) If the sleeve engages the guide ring exactly and contacts with the lower tooth chamfer of dog gear, then $z_{3.5}$ is triggered and the state switches from Stage 3(b) to Stage 4(a). (ii) If the sleeve engages the guide ring exactly and contacts with the upper tooth chamfer of dog gear, $z_{3.11}$ is triggered and the state switches from Stage 3(b) to Stage 4(c). (iii) When the sleeve tooth does not contact with the tooth chamfer of dog gear, but the sleeve flank is still in contact with the lower flank of guide ring, then $z_{3.6}$ is triggered and the state switches from Stage 3(a) to Stage 4(b). (iv) When the sleeve tooth contacts with the upper tooth chamfer of dog gear and simultaneously the sleeve flank contacts with the lower flank of guide ring, $z_{3.7}$ is triggered and the state switches from Stage 3(a) to Stage 4(c). (v) When the sleeve engages the guide ring exactly and there is no contact with the tooth chamfer of dog gear, $z_{3.8}$ is triggered and the state switches from Stage 3(b) to Stage 4(b). (vi) When the sleeve tooth contacts with the lower tooth chamfer of dog gear and simultaneously the sleeve flank contacts with the upper flank of guide ring, $z_{3.9}$ is triggered and the state switches from Stage 3(c) to Stage 4(a). (vii) When the sleeve tooth does not contact with tooth chamfer of dog gear, but the sleeve flank still contacts with the upper flank of guide ring, $z_{3.10}$ is triggered and the state switches from Stage 3(c) to Stage 4(b). (viii) If there is no contact between the tooth chamfers of the sleeve and guide ring, then $z_{4.1}$ (or $z_{4.3}$) is triggered and the state switches from Stage 4(a) (or Stage 4(c)) to 4(b). If this tooth chamfer contact happens again, $z_{4.2}$ (or $z_{4.4}$) is triggered.

Stage 5: the sleeve passes through the dog gear in this phase, the interaction ways are as follows: (i) If the sleeve collides with the lower flank of dog gear, $z_{4.5}$ is triggered and the state switches from Stage 4(a) to Stage 5(a). (ii) If the sleeve collides with the upper flank of dog gear, $z_{4.8}$ is triggered and the state switches from Stage 4(c) to Stage 5(c). (iii) When the sleeve exactly engages the dog gear, no collision happens. Then $z_{4.6}$ or $z_{4.7}$ is triggered, and the state switches from Stage 4(a) or 4(c) to Stage 5(b). When the sleeve flank does not contact the flank of dog gear, $z_{5.1}$ or $z_{5.3}$ is triggered, and the state switches from Stage 5(a) or 5(c) to Stage 5(b). If this flank contact happens again, then $z_{5.2}$ or $z_{5.4}$ is triggered.

Stage 6: when the rotating speed of dog gear, guide ring and sleeve are identical, $z_{5.5}$, $z_{5.6}$ or $z_{5.7}$ is triggered and the state switches from Stage 5(a), 5(b) or 5(c) to Stage 6, indicating that the engaging process completes.

Table 9.1 : Interaction states, state constraints and transition conditions during engagement

Stage	Interaction States	State Constraints	Transition Condition
0	—	$x_s = 0$	$z_0 : \mathcal{L} = 1$
1	—	$0 < x_s < x_1$	$z_{1.1} : x_1 + \Delta x \leqslant x_s \ \wedge \ \Delta\theta_{sr} < \theta'$
	Stage 2(a)	$S_1 = -1, i.e.$ $x_1 + \Delta x \leqslant x_s \leqslant x_1 + 2\Delta L \wedge$ $\Delta\theta_{sr} < \theta'$	$z_{1.2} : x_1 < x_s < x_1 + \Delta x$ $z_{1.3} : x_1 + \Delta x \leqslant x_s \ \wedge \ \theta_1 - \theta' < \Delta\theta_{sr} < \theta_1$
2	Stage 2(b)	$S_1 = 0, i.e. \ x_1 \leqslant x_s \leqslant x_1 + \Delta x$	$z_{2.1} : x_1 \leqslant x_s < x_1 + \Delta x \ \wedge \ \Delta\theta_{sr} < \theta'$ $z_{2.2} : x_s \geqslant x_1 + \Delta x \ \wedge \ \Delta\theta_{sr} < \theta'$
	Stage 2(c)	$S_1 = +1, i.e.$ $x_1 + \Delta x \leqslant x_s \leqslant x_1 + 2\Delta L \wedge$ $\theta_1 - \theta' < \Delta\theta_{sr} < \theta_1$	$z_{2.3} : x_1 \leqslant x_s < x_1 + \Delta x \ \wedge \ \theta_1 - \theta' < \Delta\theta_{sr} < \theta_1$ $z_{2.4} : x_s \geqslant x_1 + \Delta x \ \wedge \ \theta_1 - \theta' < \Delta\theta_{sr} < \theta_1$ $z_{2.5} : S_2 = -1, i.e. \ x_s \geqslant x_1 + 2\Delta L \ \wedge \Delta\theta_{sr} < \theta'$
	Stage 3(a)	$x_1 + 2\Delta L \leqslant x_s < x_2 \wedge$ $\Delta\theta_{sr} < \theta'$	$z_{2.6} = z_{2.7} = z_{2.8} :$ $x_s \geqslant x_1 + 2\Delta L \ \wedge \ \theta' \leqslant \Delta\theta_{sr} \leqslant \theta_1 - \theta'$
3	Stage 3(b)	$x_1 + 2\Delta L \leqslant x_s < x_2 \wedge$ $\theta' < \Delta\theta_{sr} < \theta_1 - \theta'$	$z_{2.9} = z_{3.4} : S_2 = +1, \ i.e.$ $x_s \geqslant x_1 + 2\Delta L \ \wedge \ \theta_1 - \theta' < \Delta\theta_{sr} < \theta_1$
	Stage 3(c)	$x_1 + 2\Delta L \leqslant x_s < x_2 \wedge$ $\theta_1 - \theta' < \Delta\theta_{sr} < \theta_1$	$z_{3.1} = z_{3.3} :$ $x_1 + 2\Delta L \leqslant x_s < x_2 \ \wedge \ \theta' < \Delta\theta_{sr} < \theta_1 - \theta'$ $z_{3.5} = z_{4.2} :$ $x_s \geqslant x_2 + \Delta x_2 \ \wedge \ \Delta\theta_{gr} < \Delta\theta_{sr} < \theta' + \Delta\theta_{gr}$
	Stage 4(a)	$S_3 = -1, i.e.$ $x_2 + \Delta x_2 \leqslant x_s < x_2 + 2\Delta L \wedge$ $\{\Delta\theta_{gr} < \Delta\theta_{sr} < \Delta\theta_{gr} + \theta' \vee$ $\Delta\theta_{gr} - \Delta\theta_{sr} > \theta' + \theta_{clr}\}$	$z_{3.6} = z_{3.8} = z_{3.10} : x_2 \leqslant x_s < x_2 + \Delta x_2$ $z_{3.7} : x_s \geqslant x_2 + \Delta x_2 \ \wedge \ 0 < \Delta\theta_{gr} - \Delta\theta_{sr} < \theta'$ $z_{3.9} : x_s \geqslant x_2 + \Delta x_2 \ \wedge \ \Delta\theta_{gr} < \Delta\theta_{sr} < \Delta\theta_{gr} + \theta'$
4	Stage 4(b)	$S_3 = 0, i.e. \ x_2 \leqslant x_s < x_2 + \Delta x_2$	$z_{4.1} = z_{4.3} : x_s < x_2 + \Delta x_2$
	Stage 4(c)	$S_3 = +1, i.e.$ $x_2 + \Delta x_2 \leqslant x_s < x_2 + 2\Delta L \wedge$ $\{\Delta\theta_{sr} - \Delta\theta_{gr} > \theta' + \theta_{clr} \vee$ $0 < \Delta\theta_{gr} - \Delta\theta_{sr} < \theta'\}$	$z_{4.4} = z_{3.11} :$ $x_s \geqslant x_2 + \Delta x_2 \ \wedge \ \Delta\theta_{sr} < \Delta\theta_{gr} < \theta' + \Delta\theta_{sr}$ $z_{4.5} = z_{5.2} : x_s \geqslant x_2 + 2\Delta L \wedge$ $\{\Delta\theta_{gr} < \Delta\theta_{sr} < \Delta\theta_{gr} + \theta' \vee$ $\Delta\theta_{gr} - \Delta\theta_{sr} > \theta' + \theta_{clr}\}$
	Stage 5(a)	$S_4 = -1, i.e.$ $x_2 + 2\Delta L \leqslant x_s \leqslant x_{max} \wedge$ $\{\Delta\theta_{gr} < \Delta\theta_{sr} < \Delta\theta_{gr} + \theta' \vee$ $\Delta\theta_{gr} - \Delta\theta_{sr} > \theta' + \theta_{clr}\}$	$z_{4.6} = z_{4.7} = z_{5.1} :$ $x_s \geqslant x_2 + 2\Delta L \wedge$ $\theta' < \lvert\Delta\theta_{gr} - \Delta\theta_{sr}\rvert < \theta' + \theta_{clr}$ $z_{4.8} = z_{5.4} :$ $x_s \geqslant x_2 + 2\Delta L \ \wedge \ \Delta\theta_{sr} - \Delta\theta_{gr} \geqslant \theta' + \theta_{clr}$
5			$z_{5.5} = z_{5.6} = z_{5.7} : \ \dot{\theta}_g = \dot{\theta}_s = \dot{\theta}_r \wedge x_s = x_{max}$

Continuation of Table 9.1

Stage	Interaction States	State Constraints	Transition Condition
	Stage 5(b)	$S_4 = 0, i.e.$ $x_2 + 2\Delta L \leqslant x_s \leqslant x_{max} \wedge$ $\theta' < \lvert\Delta\theta_{gr} - \Delta\theta_{sr}\rvert < \theta' + \theta_{clr}$	
	Stage 5(c)	$S_4 = +1, i.e.$ $x_2 + 2\Delta L \leqslant x_s \leqslant x_{max} \wedge$ $\{0 < \Delta\theta_{gr} - \Delta\theta_{sr} < \theta' \vee$ $\Delta\theta_{sr} - \Delta\theta_{gr} > \theta' + \theta_{clr}\}$	
6	—	$\dot{\theta}_g = \dot{\theta}_s = \dot{\theta}_r \ \wedge \ x_s = x_{max}$	

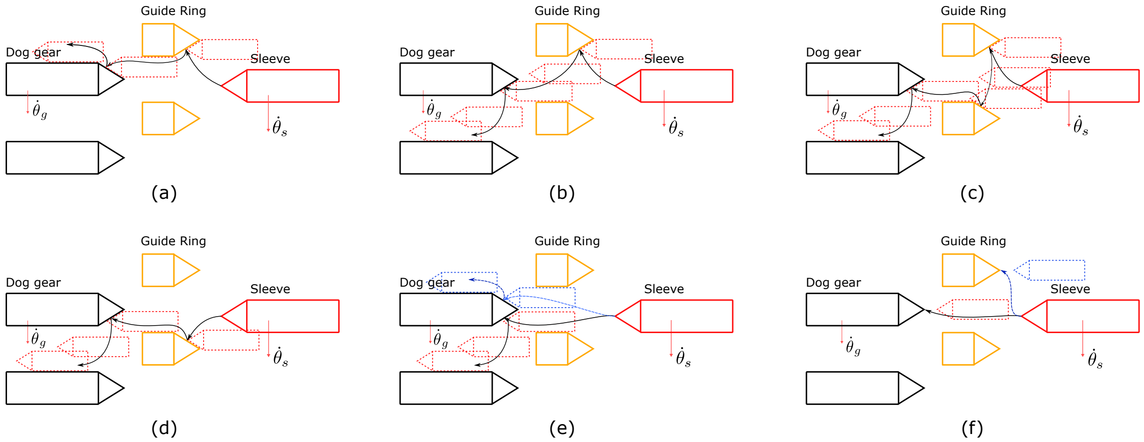

Figure 9.3 : Typical cases during engagement

Fig. 9.3 shows several typical interaction ways of the proposed bilateral Harpoon-shift synchronizer. For the case in Fig. 9.3(a), the speed of the sleeve is greater than the dog gear, and the speed difference is within the threshold, i.e., $|\dot{\theta}_s - \dot{\theta}_g| \leqslant \Delta\dot{\theta}$. The sleeve tooth contacts with the lower tooth chamfer in Stage 2 and then the flank of the guide ring in Stage 3. Next, the sleeve contacts with the upper tooth chamfer of dog gear in Stage 4 and its upper flank in Stage 5. Thus, $S_1 = -1, S_2 = -1, S_3 = +1$ and $S_4 = +1$, and the state transition path is: $z_0 \rightarrow z_{1.1} \rightarrow z_{2.5} \rightarrow z_{3.6} \rightarrow z_{4.4} \rightarrow z_{4.8} \rightarrow z_{5.7}$.

Fig. 9.3(e) displays the transition path with the shortest engaging time. The sleeve passes through the guide ring exactly, without contact with the tooth chamfers and the flank of the guide ring in the Stage 2 and 3. In Stage 4, the sleeve contacts with the tooth chamfers of the dog gear and the flank of the guide ring at the same time. Both the axial sliding speed and rotating speed are slow down due to the torque spring and damping. This, as described before, can prevent premature locking. When the sleeve overcomes the spring force with the help of the tangential force F_t acting on the chamfer surface, mainly determined by the axial force F_a, the sleeve opens the guide ring successfully. During this phase, the speed difference gradually reduces to zero and the shifting jerk also decreases significantly.

Fig. 9.3(f) presents a special case of head-on-head collision. For the traditional synchronizer, the sleeve needs to move backward and engages for the second time or several times. This will extend the engaging duration or sometimes result in fail engagement. However, in the EVs, because of the distinguished low-speed control characteristic of the EM, it can quickly rotate the dog gear with a small angular displacement to avoid the head-on-head alignment, assisting the sleeve to engage successfully.

9.4 Shifting Control Design

For the EVs with clutchless AMT, the shifting logic mainly consists of 5 phases, as shown in Fig. 9.4: (I) Motor torque reduction. In this phase, the motor output torque T_m gradually declines to zero. (II) Release synchronizer. The sleeve is separated from the current gear and move backward to the neutral position.

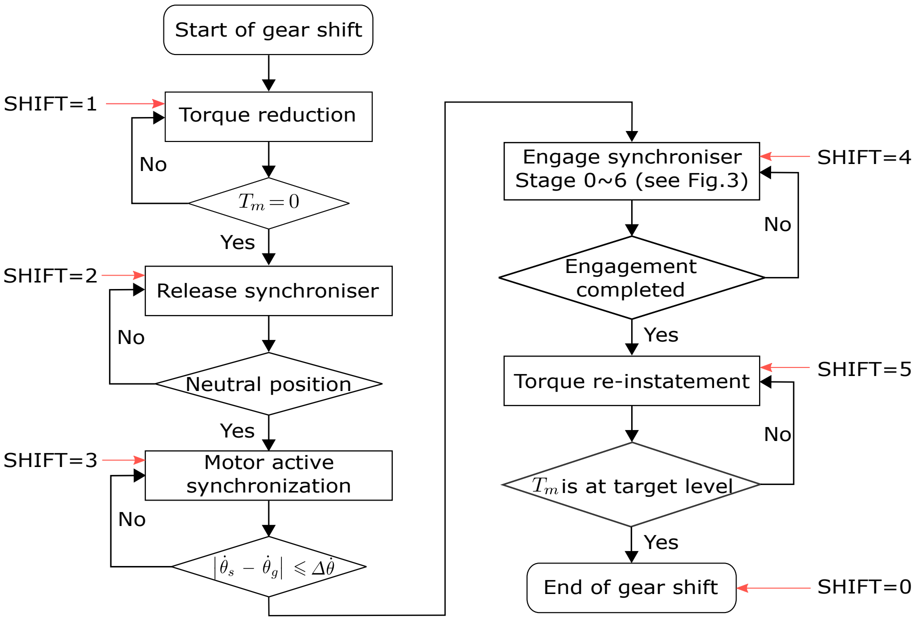

Figure 9.4 : Shifting control logic

(III) Motor active synchronization. After synchronizer disengagement, the power is disconnected, the motor will be in speed mode to actively adjust the target gear (connected with the motor through a gear set) speed to the target value which is determined by the sleeve rotating speed (i.e. the speed of transmission output shaft). When the speed difference between the target gear and output shaft is within the set threshold ($\Delta\dot{\theta}$), the output torque of the motor is zero. (IV) Engage synchronizer. The sleeve moves towards the target gear, under the action of the axial shifting force F_a. Especially, for the AMT equipped with the proposed bilateral Harpoon-shift synchronizer, this phase can be divided into 6 stages as described in Section 9.2. (V) Motor torque restoration. After the engagement, the power is connected again and the motor torque gradually recovers to the demanded level. In this study, a variable SHIFT (=1, 2, ..., 5) is used to represent these five phases, while SHIFT=0 means the shifting process completes.

9.4.1 Motor torque profiles

Considering that the motor torque control can significantly affect the torsional vibrations during shifting, two different torque profiles are used for the torque control phase. One torque profile is based on the modified bump function applied in [17, 18], and the other one is designed using a modified step function proposed in this study. Then their effects are compared to demonstrate the superiority of the proposed torque profile over the one using a modified bump function.

(a) Torque profiles based on modified bump function. In [17], torque profiles (T'_m) are designed for the torque preparation and reinstatement, which are based on a modified bump function, as follows:

$$T'_m = \begin{cases} Ae^{\frac{-1}{1-x^2}}, & \text{Torque reduction phase} \\ T - Ae^{\frac{-1}{1-x^2}}, & \text{Torque recovery phase} \end{cases} \tag{9.27}$$

where A is a constant coefficient relative to the target torque T, x is a variable relative to the torque phase duration, here $x = (t - t_{q_0})/t_{q_1}$, where t is the time, t_{q_0} is the time at initiation of the motor torque control phase, and t_{q_1} is the desired duration of the phase.

(b) Torque profiles based on modified step function. In this study, in order to reduce the torsional vibration and achieve a smooth gear shifting, a torque profile is designed based on the modified step function (see Appendix A). Here, the desired torque T is set at 80 Nm, and the desired duration of torque reduction or recovery phase is set at 250 ms, i.e., $t_{q_1} = 0.25$ s.

9.4.2 Speed profiles

In order to achieve a smooth gear changing, a speed profile is proposed based on the modified step function, as follows:

$$\dot{\theta}'_g = \begin{cases} \dot{\theta}_{g_0} + (\dot{\theta}_s - \Delta\dot{\theta} - \dot{\theta}_{g_0}) \cdot Step(t, t'_{q_0}, t'_{q_1}, h_0, h_1), & \text{Downshift} \\ \dot{\theta}_{g_0} - (\dot{\theta}_{g_0} - \dot{\theta}_s - \Delta\dot{\theta}) \cdot (1 - Step(t, t'_{q_0}, t'_{q_1}, h_0, h_1)), & \text{Upshift} \end{cases} \tag{9.28}$$

where $\Delta\dot{\theta}$ is the speed threshold for the Harpoon shift to start the engagement process [23]. t'_{q_0} is the time when the motor speed control begins, and t'_{q_1} is the desired duration of the phase. Here, t'_{q_1} is set to 0.10 s. $\dot{\theta}_{g_0}$ is the target gear speed when the active synchronous phase starts. The PI-based control logic (see Fig. 5.2) is utilized during the torque phase and active synchronous phase of motor.

9.5 Simulation and Analysis

The simulation model is set up in Simulink and the numerical solver ODE45 is used to solve the dynamic equations of each stage, with the maximum step size 5×10^{-5}.

9.5.1 Upshift simulation

To prove the effectiveness of the proposed power-train model and the control model, a typical 1^{st} to 2^{nd} upshift simulation is conducted in the Simulink environment. The rotating speed of the motor is about 1800 rpm and the speed difference is 10 rpm. Fig. 9.5(a) shows the speed responses of DoFs of the engaging-related parts, while the motor torque response, the shifting control phases, and the stages of engagement and disengagement are shown in Fig. 9.5(b). The total shifting process mainly consists of five phases, as described in Section 5. The motor torque begins to reduce in the reduction phase (I) (SHIFT=1). When this phase completes, the motor goes into the free mode and its output torque is zero. Then the sleeve starts to disengage from the current gear in the phase (II). During this phase, the synchronizer state changes from Stage 6 to 0. It is worth pointing out that there is a sudden change in the speed of the 1st gear guide ring as shown in Fig. 9.5 (a), because when the sleeve teeth is separated from the guide ring, the latter quickly rotates backward to the equilibrium position under the restoring force of the compressed torque spring [1], i.e., the guide ring teeth is in the middle of external grooves of dog gear (see Fig. 8.2), to prevent premature lock if this gear is chosen again. Next, the active synchronization phase (III) begins when the sleeve arrives at the neutral position. In this phase, most of the speed difference between the dog gear 2 and the shaft (i.e. sleeve) is eliminated by the motor. As the speed discrepancy reaches a designed threshold ($\varDelta\dot{\theta}$), the engaging process goes into phase (IV). In this phase, the sleeve axially moves from the neutral position towards the dog gear 2. It is worth noting that in Stage 4 and 5, as the sleeve overcomes the spring force and opens the guide ring, the residual speed discrepancy is eliminated gradually, which is helpful in alleviating the shift shock. When sleeve successfully engages the target gear, the dog gear 2, guide ring 2 and the sleeve rotate at the same angular velocity. Due to the acceleration discrepancy between the driveline upstream components from the motor to the target gear and the downstream components from the sleeve to the vehicle, the shifting shocks still exists in the powertrain system, leading to the speed fluctuation on the output shaft after engagement, i.e., in the beginning of Phase

(V), as shown in Fig. 9.5(a). Then the motor torque recovers to the designed level in Phase V. Here, SHIFT=0 denotes that the shift process completes and no gear change signal is triggered. It should be noted that as the engagement completes, the spring elastic energy will be stored until sleeve disengages from this gear in the next shifting event. From Fig. 9.5(b), it can be seen that the shifting time is 0.85 s, which is less than 1 s.

9.5.2 Comparison of modified step function and bump function

To prove the improvements of the proposed torque control method (based on the modified step function), comparisons are performed with a torque profile based on the modified bump function presented in [17, 18]. To accurately evaluate the effects of these two profiles, the durations of the torque control phase for these two cases are set at the same value, here $t_{q_1} = 250$ ms. A 1^{st}-2^{nd} upshift simulation is carried out, and the motor rotating speed is 3000 rpm and the threshold of speed difference is 10 rpm.

Fig. 9.6(a) displays the motor torque change during gear shifting. Particularly, the torque profile using modified step function (defined as Case A) changes slowly at the beginning of the reduction phase. Then, the torque profile drops dramatically to the target level. At last, the profile comes to the desired level slowly. While the torque curve based on the bump function (defined as Case B) also changes slowly at the beginning and the end of the torque reduction phase and declines significantly during this phase. However, the most differences between the two profiles lie in two aspects: a) the change rate of the torque profile in Case A is less than that in

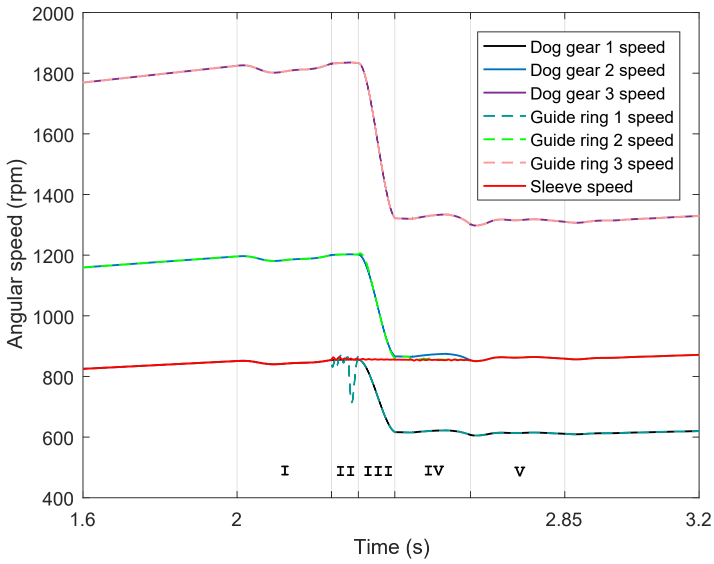

(a) Speed responses

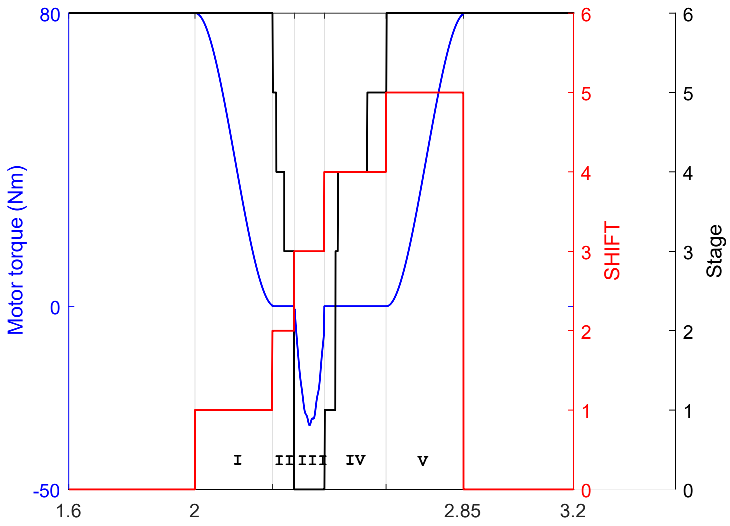

(b) Motor torque, control strategy and stage of engagement and disengagement

Figure 9.5 : Speed responses, motor torque, shifting control phases, and engagement & disengagement stages

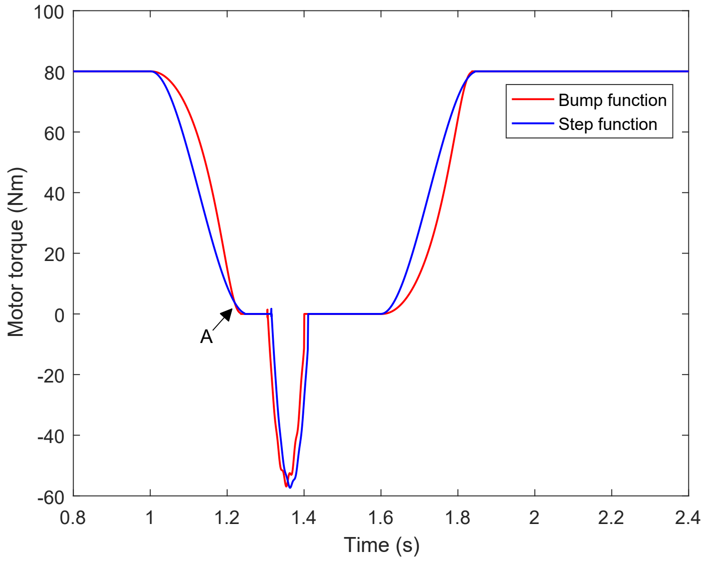

(a) Motor output torque

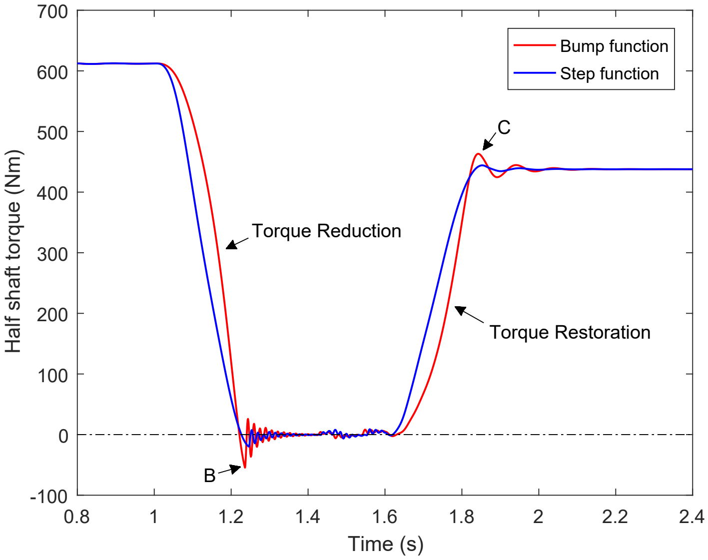

(b) Torque responses of half shaft

Figure 9.6 : Comparison of the torque control based on modified step function and bump function

Case B, indicating that the former generates less jerk than the latter since the jerk is proportional to the torque change rate [16, 77]. b) the torque profile in Case A changes more slowly from point A to the end of the reduction phase than that in Case B, which is helpful in reducing the torsional shock.

Fig. 9.6(b) shows the comparison of the torque responses on the half shaft. As respected, for the profile in Case A, the torque peaks are only 19.9 Nm (see Table 9.2) in torque reduction phase and 6.5 Nm in the reinstatement phase, much less than those of Case B, which are 54.6 and 25.5 Nm, respectively. And the absolute value of the max jerk reduces from 10.4 to 3.94 m/s^3 in the torque reduction phase and from 6.77 to 4.45 m/s^3 in the torque recovery phase. Therefore, according to the analysis of the numerical simulation results, a conclusion can be drawn that the proposed torque profile using the modified step function is superior to that based on the bump function.

Table 9.2 : Comparison of torque peaks and maximum jerks between two different torque profiles

Function	Torque peak caused by torque reduction (Nm)	Torque peak caused by torque recover (Nm)	Max jerk caused by torque reduction (m/s^3)	Max jerk caused by torque recover (m/s^3)
Modified Bump	54.6	25.5	10.4	6.77
Modified Step	19.9	6.5	3.94	4.45

9.5.3 Impact of spring stiffness

The torque springs of bilateral Harpoon-shift synchronizer play an important role in absorbing the torsional vibrations during the engagement. In this section, gear shift simulations are conducted to figure out the effect of spring stiffness on the shifting jerk. In the simulation, the motor rotating speed is 1500 rpm and the speed difference is 10 rpm. In addition, considering that the torque reinstatement will also generate jerk, the motor output torque is set to zero after engagement in the simulation. Therefore, the spring stiffness effect on the jerk can be more clearly analyzed. Fig. 9.7 displays the influences of the spring stiffness (k_{rg}) on the jerk of each gear. And the absolute value of the maximum jerk, torque peak and engaging time of each gear under different spring stiffness are listed in Table 9.3.

Fig. 9.7(a) shows the jerks of downshift from 2$^{\text{nd}}$ to 1$^{\text{st}}$ gear, under five different spring stiffnesses. Particularly, the jerk at point A is generated by the tooth chamfer contact between the sleeve and guide ring in Stage 2 of the engaging process. The jerk at point B is caused when the sleeve tooth contacts with the tooth chamfers of dog gear in Stage 4. While the jerk at point C is caused when the sleeve begins to collide with the flank of the dog gear. The max jerk (at point D) happens when the sleeve engages with the dog gear in Stage 6, due to the acceleration discrepancy between the two engaging components. Taking the jerk and engaging time into consideration, $k_{rg} = 2500$ N/m is chosen as the optimized spring stiffness for the 1$^{\text{st}}$ gear.

It is worth noting that the jerks in 1$^{\text{st}}$ gear under various spring stiffness are

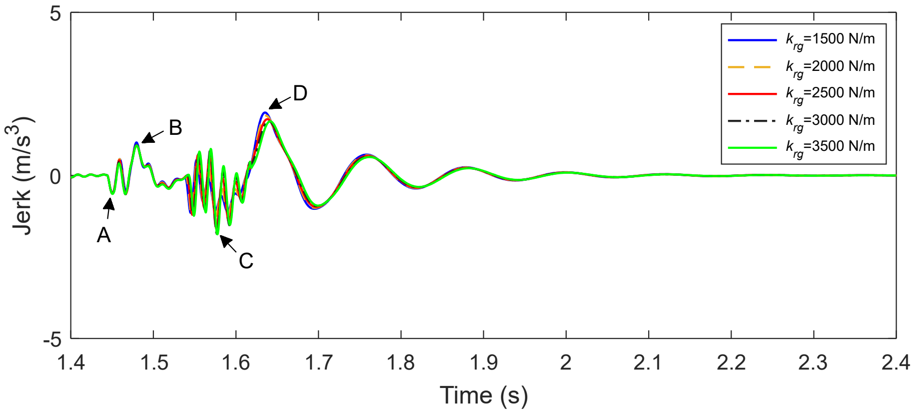

(a) Jerks of 1st gear

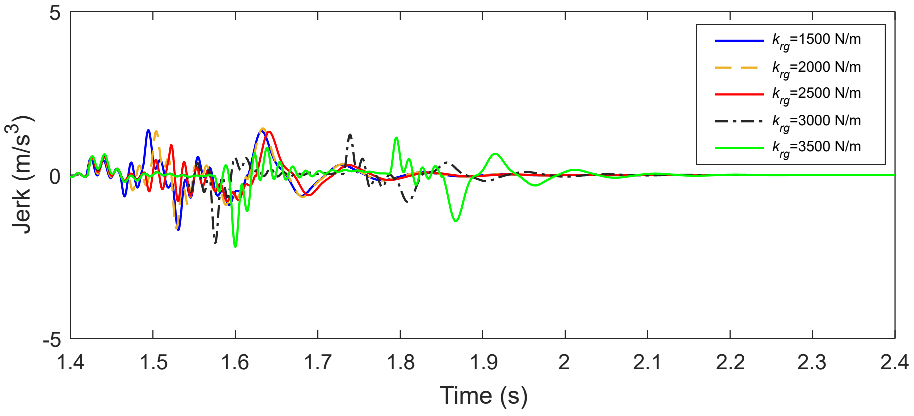

(b) Jerks of 2nd gear

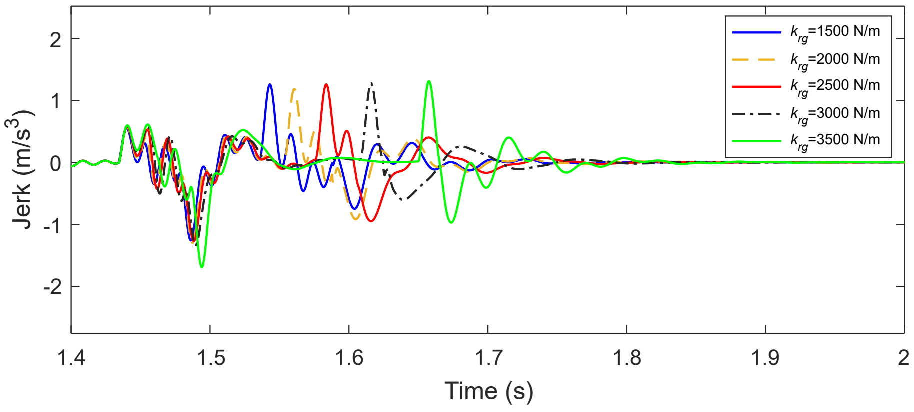

(c) Jerks of 3rd gear

Figure 9.7 : Effects of spring stiffness on the jerk of each gear

Table 9.3 : Maximum jerk, torque peak and engaging time for each gear under various spring stiffness

Gear	k_{rg} N/m	Maximum jerk (m/s^3)	Torque peak (Nm)	Engaging time (s)
1st	1500	1.93	22.20	0.1972
	2000	1.84	22.34	0.1985
	2500	1.73	23.08	0.1997
	3000	1.67	23.43	0.2007
	3500	1.66	23.30	0.2015
2nd	1500	1.68	12.69	0.1985
	2000	1.63	13.26	0.2023
	2500	1.32	11.13	0.2129
	3000	2.08	11.81	0.3817
	3500	2.19	12.40	0.4391
3rd	1500	1.26	7.47	0.1764
	2000	1.30	7.22	0.1765
	2500	1.27	7.57	0.1936
	3000	1.34	8.49	0.2131
	3500	1.70	9.29	0.2519

almost the same, obviously different from the jerks of the other gears. The reason lies in that the equivalent inertia of the 1^{st} gear, i.e. the powertrain upstream, is larger than those of the gear 2^{nd} and 3^{rd} as the value of 1^{st} gear ratio γ_1 is larger than γ_2 and γ_3.

The spring stiffness effects on the jerks of the 2^{nd} and 3^{rd} gear are shown in Fig. 9.7(b) and 9.7(c), respectively. As the stiffness increases, the engagement duration of the 2^{nd} gear significantly extends from 0.1985 s (k_{rg} = 1500 N/m) to 0.4391 s (k_{rg} = 3500 N/m), as shown in Table 9.3. It can also be found that k_{rg} = 2500 N/m generates the minimum jerk in the 2^{nd} and 3^{rd} gear, which are 1.32 and 1.27 m/s^3 respectively. This indicates that 2500 N/m is the optimized spring stiffness for these two gears with the bilateral Harpoon-shift synchronizer.

Table 9.4 displays the optimized torque spring stiffness of each gear for the unilateral Harpoon shift [23] and the proposed bilateral version. It is obvious that for the unilateral Harpoon shift, the spring stiffness changes dramatically from 2500 to 10000 N/m, whereas the optimized stiffnesses for the proposed bilateral Harpoon shift in these gears are the same (only 2500 N/m), indicating that the bilateral version is less sensitive to the spring stiffness.

9.5.4 Verification of torque spring functions

Dong et al. [162] made an effort to accomplish the synchronization process without the synchronizer. In their study, they utilized the motor control strategies in the active synchronization phase to reduce the speed difference. However, the speed discrepancy was not completely eliminated in this phase. Actually, they conducted

Table 9.4 : Comparison of optimized torque spring stiffness between unilateral and bilateral Harpoon shift

Gear	Spring Stiffness k_{rg} (N/m)		Shifting Force (N)
	Unilateral Harpoon Shift	Improved Bilateral Harpoon shift	
1st	10000	2500	38
2nd	4000	2500	
3rd	2500	2500	

engagement within the speed difference of 30 rpm, without the conventional synchronizer being involved. Nevertheless, no shifting jerks were discussed in the literature. Thus, it is hard to evaluate the actual effects of their control strategies.

To our best knowledge, it is difficult to completely align the two engaging components when rotating at high speed, since this requires accurate motor control as well as high-precision measuring sensors. If the sleeve engages the dog gear when there is a large speed discrepancy due to the sensor precision or fault [70], then a tooth crash will happen, leading to a greater jerk or even damage to the teeth. However, the torque spring installed in the proposed bilateral Harpoon-shift synchronizer is capable of eliminating the residual speed difference and absorbing torsional shock during the engagement, even if there were a large speed discrepancy.

In this section, the effects of torque spring on the shifting jerk is quantitatively analyzed. Fig. 9.8 displays the comparisons of half shaft torque responses and jerks between an extremely soft spring ($k_{rg} = 100$ N/m) and the optimized spring

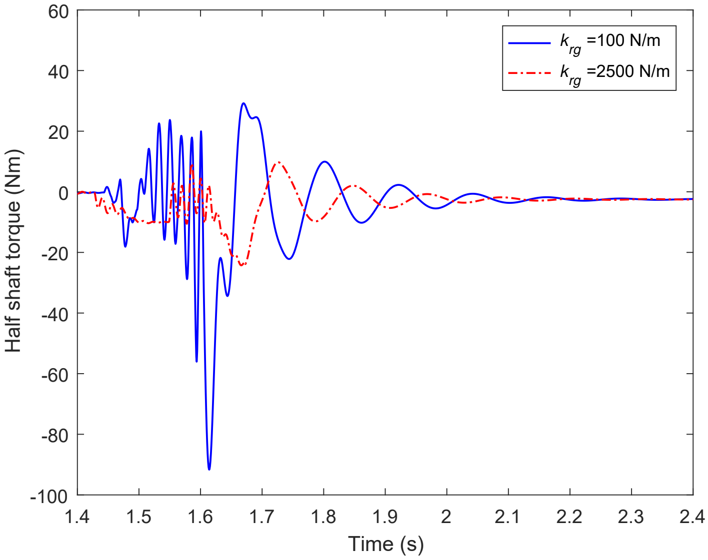

(a) Torque response of half shaft

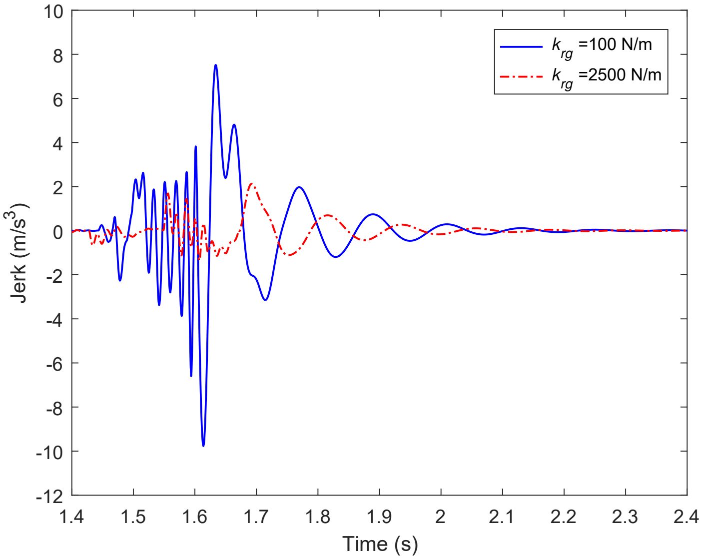

(b) Vehicle jerk

Figure 9.8 : Comparison of shifting shocks between soft spring and optimized spring

($k_{rg} = 2500$ N/m) during 2nd-1st downshift. The motor speed is approximately 2000 rpm and the speed difference is 30 rpm. For the first case, the spring is too soft for the guide ring to have the function of blocking the external groove of the dog gear and preventing a premature lock. As expected, the collision between the dog gear and sleeve during engagement of the first case is more serious than the second case, despite engaging at the same speed difference. The torque peak and maximum jerk of the first case are 91.66 Nm and 9.77 m/s^3 (see Table 9.5), which are significantly greater than those of the second case (only 24.27 Nm and 2.13 m/s^3). This indicates that the optimized springs have the ability to absorb the shifting shock and achieving a more smooth engagement, but compromising at a longer engagement duration. As shown in Table 9.5, the duration extends from 188.3 to 256.1 ms. The results show that the optimized torque spring is a guarantee to achieve a high-quality shifting when there is a large speed discrepancy during the engaging phase.

Table 9.5 : Comparison of shifting shocks and duration between two torque spring stiffness

k_{rg} N/m	Maximum jerk (m/s^3)	Torque peak (Nm)	Engaging time (s)
100	9.77	91.66	0.1883
2500	2.13	24.27	0.2561

In addition, comparing Table 9.3 and Table 9.5, it can be found that there is no great difference in the jerks of 1st gear using the optimized spring ($k_{rg} = 2500$ N/m) between the speed difference of 30 rpm and 10 rpm, which are 2.13 and 1.73 m/s^3

respectively. This means that a smooth engagement can also be achieved even if the speed discrepancy is 30 rpm after active speed adjusting, which can reduce the needs for high accuracy of motor speed control.

9.5.5 Impact of chamfer angle

This section mainly focuses on investigating the effects of different chamfer angles on the torque responses and vehicle jerks, rather than the optimization process. Thus, a range of values of the chamfer angle from 40° to 64° is chosen to investigate their impacts on the shifting shock. Then, the optimized chamfer angle is obtained through quantitative analysis according to the torque peak, jerk, and engaging duration based on simulations.

For a conventional synchronizer, the synchro ring is coupled with the clutch gear after the speed synchronization completes, because of the static frictional torque acting on the cone surfaces. When the sleeve and gear splines are into contact, the axial shift force increases dramatically to separate the synchro ring from the gear, allowing the sleeve to engage in the gear. This leads to the so-called second bump [98], significantly affecting the riding comfort and the service life of synchronizer.

Different from the traditional counterparts, the proposed bilateral Harpoon shift does not rely on the frictional torque to accomplish the speed alignment. Hence, these two parts are not coupled together. Instead, they are flexibly linked through the torque spring. An index torque is also required to compress the spring and finally open the guide ring. Eq. 10.3 shows that the tooth chamfer angle has a significant effect on the tangential force F_t and consequently on the index torque. Thus, in this section, a quantitative analysis based on the simulation results is performed to investigate the impacts of the chamfer angle of the bilateral Harpoon shift on the shifting quality.

Upshift simulations from $1^{\text{st}} - 2^{\text{nd}}$ gear are conducted in Simulink based on the integrated powertrain model developed previously. The motor rotating speed is approximately 3000 rpm when the gearshift starts and the speed difference is 10 rpm. Based on the same consideration that the torque restoration has an influence on the jerk as described early, the motor output torque is kept at zero after the engagement.

Fig. 9.9 shows the sleeve axial displacement during the engagement. It is obvious that as the chamfer angle increases from 40° to 60°, the time duration when the sleeve reaches the engaged position increases significantly. However, there is no significant increment of the duration when the chamfer angle increases from 60° to 64°.

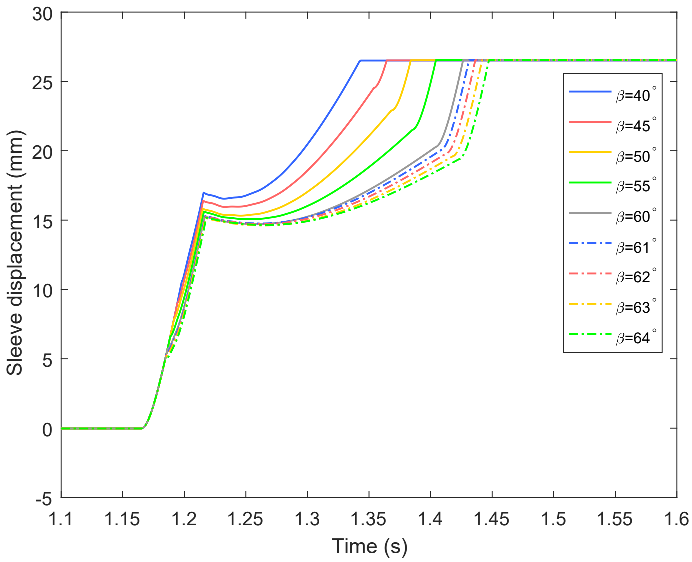

Figure 9.9 : Sleeve axial displacement

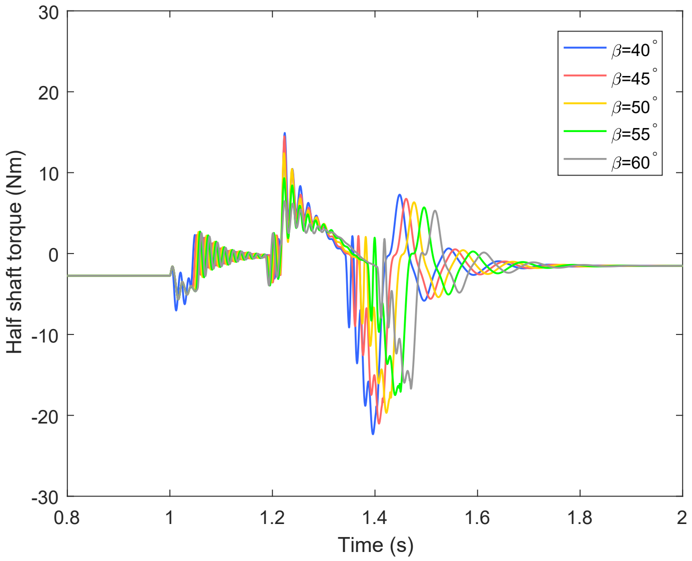

(a) Torque responses of half shaft: $\beta \in [40°, 60°]$

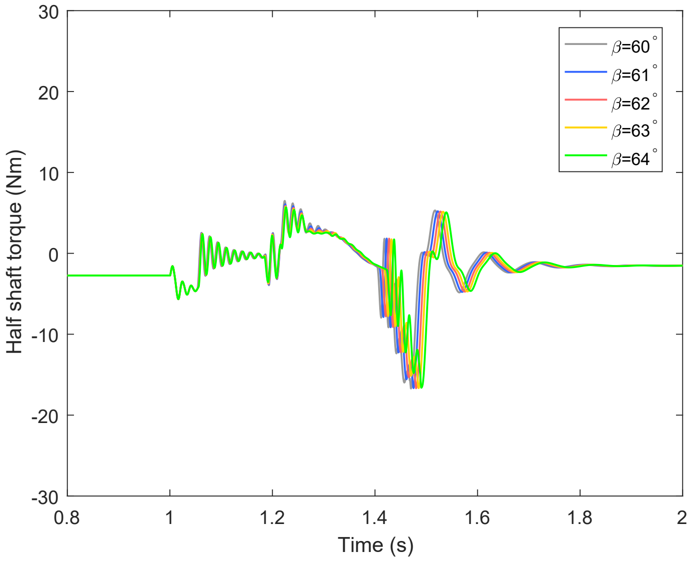

(b) Torque responses of half shaft: $\beta \in [60°, 64°]$

Figure 9.10 : Effects of chamfer angle on the torque response of half shaft

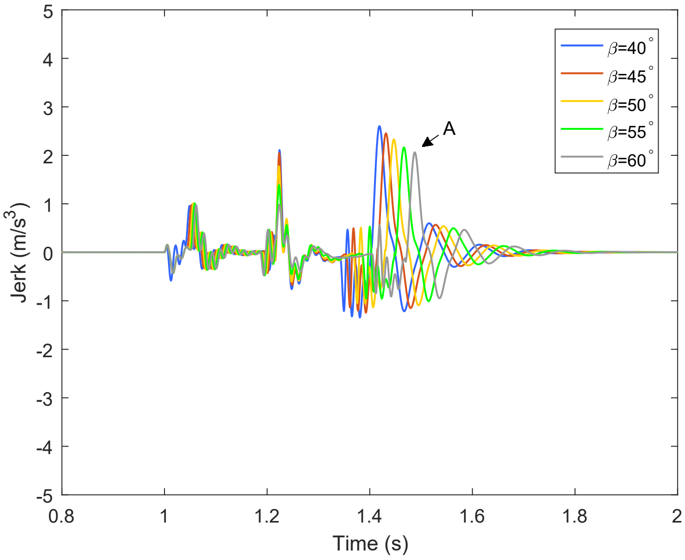

(a) Vehicle jerks: $\beta \in [40°, 60°]$

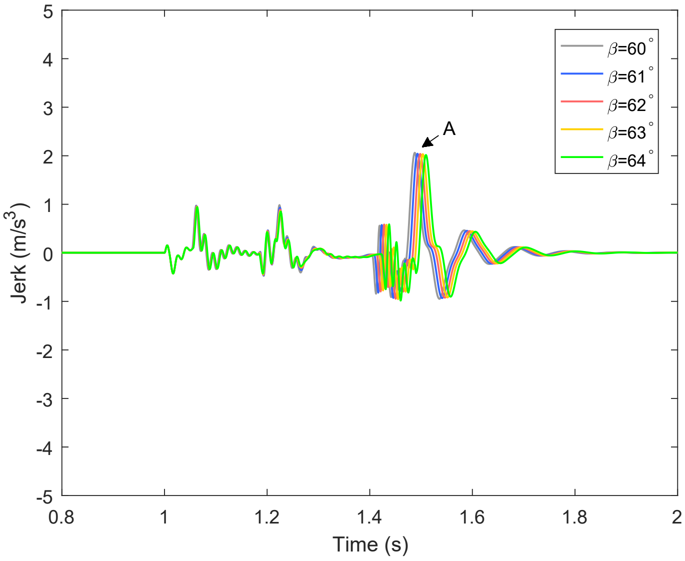

(b) Vehicle jerks: $\beta \in [60°, 64°]$

Figure 9.11 : Effects of chamfer angle on the vehicle jerk

Fig. 9.10 shows the half shaft torque responses under various chamfer angles, from 40° to 60° and from 60° to 64°, respectively. While Fig. 9.11 displays their responding vehicle jerks. As the chamfer angle increases from 40° to 60°, the torque peak reduces from 22.33 to 16.71 Nm (Fig. 9.10(a)), and the max jerk decreases from 2.60 to 2.06 m/s^3 (see point A in Fig. 9.11(a) and Table 9.6). Nevertheless, the engaging time increases significantly from 237.0 to 302.8 ms. When the chamfer angle increases from 60° to 64°, there is no significant difference in terms of the torque peak (Fig. 9.10(b)) and maximum jerk (Fig. 9.11(b)), but the engaging duration increases from 302.8 to 323.7 ms. From the analysis of the simulation results, a conclusion can be drawn that the optimized tooth chamfer angle for the dog gear of the bilateral Harpoon shift is 60°.

Table 9.6 : Simulation results under different chamfer angle

$\beta(°)$	Maximum jerk (m/s^3)	Torque peak (Nm)	Engaging time (s)
40	2.60	22.33	0.2370
45	2.45	21.02	0.2492
50	2.33	19.70	0.2640
55	2.16	17.50	0.2826
60	2.06	16.71	0.3028
61	2.04	16.67	0.3076
62	2.04	16.68	0.3127
63	2.03	16.66	0.3175
64	2.01	16.62	0.3237

9.6 Summary

In this chapter, multi-body dynamics is applied to establish the model of an EV powertrain system with clutchless AMT integrating an original and detailed model of the proposed synchronizer. The gearshift process is divided into five phases. Particularly, for the phase IV, the engaging process of the synchronizer is defined as six stages. The integrated multi-body model can cover the interaction cases between the sleeve, guide ring and dog gear. In addition, to improve the riding comfort, the torque and speed profiles are designed based on the modified step function for the motor to track during gear shift process. Simulations based on the integrated model are carried out to study the transient vibrations of the powertrain system, which helps to investigate the performance of the proposed bilateral Harpoon shift in terms of jerk, torque peak, and engaging duration. The results verify the effectiveness of the model and the motor control strategy. Furthermore, comparisons are performed to demonstrate the superiority of the proposed torque profiles over its counterpart based on the modified bump function. Then the impacts of spring stiffness and tooth chamfer angle are quantitatively analyzed and then these two important parameters are optimized to alleviate the jerk during shifting.

Results show that the torque springs of the bilateral Harpoon-shift synchronizer can adsorb the torsional shocks during the engaging process. Besides, the shifting force is constant and small (only 38 N) throughout the shifting process. Thus, an open-loop control rather than a closed-loop control can be used to complete engagement, which significantly simplifies the control system. Due to its special engaging principle, the proposed synchronizing mechanism avoids the friction loss and overcomes the issue of wear. Hence, the proposed bilateral Harpoon-shift synchronizer is able to improve the efficiency of transmission and the gearshift quality for EVs.

Chapter 10

Thesis Conclusions and Future Works

10.1 Summary of Thesis

This thesis introduces the concepts of two types of Harpoon-shift synchronizer, i.e., unilateral and bilateral Harpoon shift, aiming to improve shifting quality and the transmission performance for EVs and simultaneously, overcome some of the biggest drawbacks of traditional cone-clutch synchronizers, including energy losses due to friction, heat dissipation, and wear. The structure and operating principles of these two Harpoon shift synchronizers are illustrated in detail.

An original dynamic model of EV powertrain system equipped with a 3-speed CLAMT is developed. And A detailed dynamic model of the unilateral Harpoon-shift synchronizer mechanism is built and integrated into the powertrain model. Gear shift simulations are conducted to investigate the synchronizer transient characteristics and their influences on the system vibrations during gear shifting. This helps to evaluate the engaging performance of the unilateral Harpoon shift.

Also, a shift control logic based on a modified step function is proposed to improve driving comfort. Up- and down-shift simulations are performed using Simulink and Matlab, and the simulation results verify the effectiveness of the dynamic model and control strategy. Besides, to alleviate the shift shocks, the Harpoon shift's torque spring stiffness of each gear is optimized. Also, quantitative analysis is carried out to figure out the impacts of speed difference as well as rotational inertia on the vehicle jerk. Simulation results show that the jerk substantially declines using the optimized torque springs. This demonstrates the incomparable merits of the unilateral Harpoon shift over conventional counterparts.

A testing bench is also developed to investigate the transients during engagement of the unilateral Harpoon-shift synchronizer mechanism. Experimental results verify the effectiveness of the synchronizer model, indicating that the unilateral Harpoon-shift model can capture the synchronizer's transient vibrations. However, the unilateral Harpoon shift still has two shortcomings. It cannot complete engagement successfully when the speed difference is too small. Furthermore, the sleeve angular speed must be faster than the dog gear, Otherwise, the engagement will be failed since it is unilateral.

In order to overcome these drawbacks of unilateral Harpoon shift and improve the shifting quality for EVs, a novel concept of bilateral Harpoon-shift synchronizer is presented in this thesis.

An original and detailed multi-body dynamic model of the bilateral Harpoon shift is developed to capture the synchronizer transient dynamics during engagement. In the model, the whole engaging process is divided into six stages, and it is able to cover the interacting cases between the guide ring, sleeve, and dog gear. The synchronizer model is then integrated into the established EV powertrain model with multi-speed CLAMT to study the system transient responses. In addition, to guarantee a smooth gear shift, both the speed and torque profiles are designed according to the modified step function for the motor torque control and active speed adjusting. The gearshift simulation results verify the effectiveness of the dynamic model of the bilateral Harpoon shift and the motor control strategies. Also, comparisons are performed to prove the superiority of the torque profiles proposed over those based on the modified bump function. Then, the effects of the torque springs and the tooth chamfer angle on the shifting jerk are comprehensively analyzed and then optimized to improve gearshift quality.

In summary, the bilateral Harpoon-shift synchronizer with optimized torque springs can adsorb the shifting shocks and consequently improve the gear-shift quality for multi-speed EVs. Besides, only a constant and small axial shifting force is required for the engagement. Therefore, open loop control can be utilized during gear change, which greatly simplifies the control system. This is desirable for EVs in terms of saving energy and improving efficiency.

10.2 Summary of Contributions

The knowledge contributions of the thesis are listed as follows:

(1) Detailed and original models of two types of Harpoon-shift synchronizer are developed in this study.

(2) An original dynamic model of an EV powertrain system equipped with multi-gear CLAMT is established. It integrates the model of Harpoon-shift synchronizer to investigate this subsystem's influence on the transient characteristics powertrain system.

(3) Experiment is developed to investigate the Harpoon shift transient dynamics

and evaluate engaging performance.

(4) The important design parameters of Harpoon shift, including the torque spring stiffness and chamfer angle of spline teeth, are optimized in terms of shifting jerks through the numerical simulations, to improve the shifting quality.

10.3 Future Works

Further investigation can be conducted on the basis of the research work in this thesis, as follows:

(I) Improvement of Harpoon-shift design. Synchronizer design plays a crucial role in improving the shifting quality and transmission performance.

(II) Advanced coordinated shifting control of the electric motor and actuator mechanism. Gearshift control also has a significant influence on the gear change quality.

(III) More detailed model of powertrain system, synchronizer and actuator mechanism will facilitate a comprehensive understanding of the influences of these subsystems on the powertrain system during shifting.

Appendices

Appendix A

Impact Function and Step Function

The impact function and step function [1, 23, 155] are defined as follows:

$$F = \begin{cases} -kq^n - c_{max}\dot{q} \cdot Step(q, q_0, q_1, h_0, h_1) & (q_0 < q) \\ 0 & (q \leqslant q_0) \end{cases} \tag{10.1}$$

$$Step(q, q_0, q_1, h_0, h_1) = \begin{cases} h_0 & (q \leqslant q_0) \\ h_0 + (h_1 - h_0)\mathit{\Delta}^2(3 - 2\mathit{\Delta}) & (q_0 < q < q_1) \\ h_1 & (q \geqslant q_1) \end{cases} \tag{10.2}$$

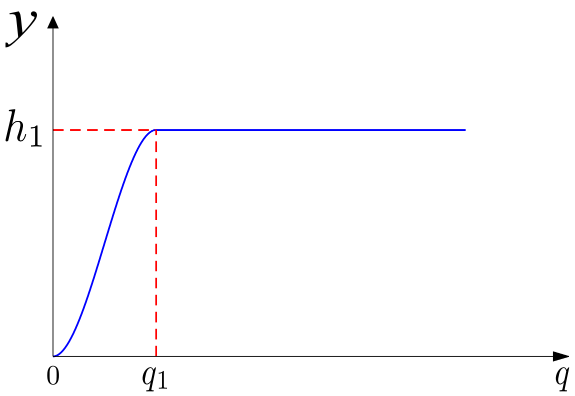

Figure 10.1 : Characteristic of Step function

where $q_0 = 0$, $h_0 = 0$, $h_1 = 1$, $\mathit{\Delta} = (q - q_0)/(q_1 - q_0)$, where q_1 is the maximum penetration depth, which corresponds to the maximum damping coefficient c_{max}, as shown in Fig. 10.1 [1, 155].

Appendix B

The tangential force F_t acting on the chamfer is shown as follows

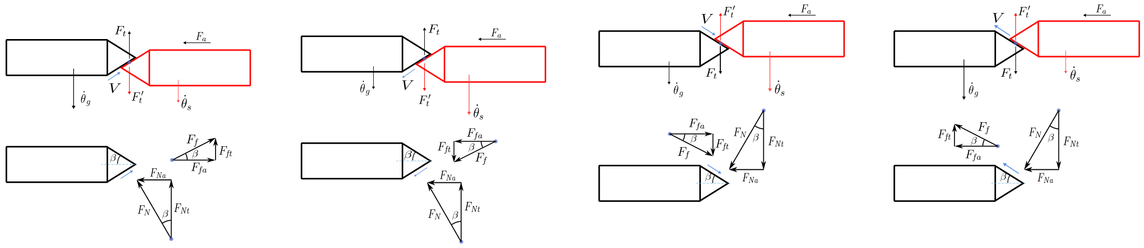

(a) (b) (c) (d)

Figure 10.2 : Spline chamfer contact

In the above figure, V represents the sliding velocity of sleeve tooth chamfer with respective to guide ring or dog gear chamfer. F_t can be calculated by

$$F_t = \begin{cases} (F_a - c_a\dot{x}_s)\dfrac{1+\mu\tan\beta}{\tan\beta-\mu} & V \neq 0\text{: cases of (a) and (c)} \\ F_a\cot\beta & V = 0 \\ (F_a - c_a\dot{x}_s)\dfrac{1-\mu\tan\beta}{\tan\beta+\mu} & V \neq 0\text{: cases of (b) and (d)} \end{cases} \tag{10.3}$$

where μ is the friction coefficient of spline chamfer surface [22]. It should be noted that the Eq. 10.3 can be applied to calculate the tangential force acting on the chamfer of guide ring or dog gear.

Appendix C

Powertrain Parameters [23]

Table 10.1 : Powertrain parameters

Parameter	Description	Value
J_m	Motor	0.04 kg m^2
J_{dout}	Final drive	0.039 kg m^2
J_h	Wheel hubs	1.398 kg m^2
J_v	Vehicle and tires	135.120 kg m^2
J'_s	Sleeve and hub	0.011372 kg m^2
J'_{gin}	Input shaft	0.000675 kg m^2
J'_{r_i}	Guide ring	0.000314 kg m^2
m_v	Vehicle mass	1300 kg
m_s	Sleeve mass	0.8054 kg
γ_1	The 1st gear ratio	2.08
γ_2	The 2nd gear ratio	1.48
γ_3	The 3rd gear ratio	0.97
γ_d	Final ratio	3.73
r_w	Tire radius	0.32 m
N	The number of sleeve prongs	8
k_1	Output shaft of motor	10000 Nm/rad
k_2	Output shaft of transmission	15000 Nm/rad
k_3	Half shafts	30000 Nm/rad
k_4	Tires	13600 Nm/rad

Continuation of Table 10.1

Parameter	Description	Value
c_1	Damping 1	10 Nm s/rad
c_2	Damping 2	10 Nm s/rad
c_3	Damping 3	10 Nm s/rad
c_4	Tire damping	100 Nm s/rad
c_m	Viscous damping	0.0015 Nm s/rad
c_t	Viscous damping	0.01 Nm s/rad
$c_{x_i}, (i = 1, 2, 3)$	Viscous damping	85 N s/m
c_{sr}	Equivalent damping coefficient	0.9604 Nm s/rad
c_{sg}	Equivalent damping coefficient	0.9604 Nm s/rad
c_{rg}	Viscous damping	0.003 Nm s/rad
n	Nonlinear exponent factor	1.5
μ_s, μ_s'	Chamfer friction	0.05
μ_{sg}	Dynamic friction	0.05

Bibliography

[1] W. Mo, P. D. Walker, Y. Fang, J. Wu, J. Ruan, and N. Zhang, “A novel shift control concept for multi-speed electric vehicles,” *Mechanical Systems and Signal Processing*, vol. 112, pp. 171–193, 2018.

[2] F. Di Nicola, A. Sorniotti, T. Holdstock, F. Viotto, and S. Bertolotto, “Optimization of a multiple-speed transmission for downsizing the motor of a fully electric vehicle,” *SAE International Journal of Alternative Powertrains*, vol. 1, no. 1, pp. 134–143, Apr. 2012.

[3] A. Sorniotti, “A novel clutchless multiple-speed transmission for electric axles,” *International Journal of Powertrains*, vol. 2, no. 2/3, pp. 103–131, 2013.

[4] C. Changenet, X. Oviedo-Marlot, and P. Velex, “Power Loss Predictions in Geared Transmissions Using Thermal Networks-Applications to a Six-Speed Manual Gearbox,” *Journal of Mechanical Design*, vol. 128, no. 3, pp. 618–625, Aug. 2005.

[5] B. Paffoni, R. Progri, R. Gras, and J. Blouët, “The hydrodynamic phase of gearbox synchromesh operation: The influence of radial and circumferential grooves,” *Proceedings of the Institution of Mechanical Engineers, Part J: Journal of Engineering Tribology*, vol. 211, no. 2, pp. 107–116, 1997.

[6] R. J. Socin and L. K. Walters, “Manual transmission synchronizers,” in *1968 Automotive Engineering Congress and Exposition.* SAE International, Feb. 1968.

[7] H. Son, Y.-S. Yoon, K.-S. Kim, S. J. Kim, and C. Song, “Economic hybrid transmission system using clutchless geared manual transmission,” in *28th Electric Vehicle Symposium and Exhibition, Goyang, South Korea, May*, 2015, pp. 3–6.

[8] C.-Y. Tseng and C.-H. Yu, “Advanced shifting control of synchronizer mechanisms for clutchless automatic manual transmission in an electric vehicle,” *Mechanism and Machine Theory*, vol. 84, pp. 37–56, 2015.

[9] C. Yu and S. Goh, “Study of seamless gear-shift strategy for a clutchless automated manual transmission,” in *2017 IEEE/SICE International Symposium on System Integration (SII)*, Dec 2017, pp. 417–422.

[10] S. J. Kim, K. Kim, and D. Kum, “Feasibility assessment and design optimization of a clutchless multimode parallel hybrid electric powertrain,” *IEEE/ASME Transactions on Mechatronics*, vol. 21, no. 2, pp. 774–786, April 2016.

[11] Y. B. Bang and M. Yoon, “3-speed transmission using dual motors and one-way clutches,” *IEEE/ASME Transactions on Mechatronics*, vol. 21, no. 1, pp. 412–418, Feb. 2016.

[12] A. Sorniotti, T. Holdstock, M. Everitt, M. Fracchia, F. Viotto, C. Cavallino, and S. Bertolotto, “A novel clutchless multiple-speed transmission for electric axles,” *International Journal of Powertrains*, vol. 2, no. 2-3, pp. 103–131, 2013.

[13] K. Zhao, Y. Liu, X. Huang, R. Yang, and J. Wei, “Uninterrupted shift transmission and its shift characteristics,” *IEEE/ASME Transactions on Mechatronics*, vol. 19, no. 1, pp. 374–383, Feb. 2014.

[14] Z. Lei, D. Sun, Y. Liu, D. Qin, Y. Zhang, Y. Yang, and L. Chen, “Analysis and coordinated control of mode transition and shifting for a full hybrid electric vehicle

based on dual clutch transmissions," *Mechanism and Machine Theory*, vol. 114, pp. 125 – 140, 2017.

[15] M. S. R. Mousavi, A. Pakniyat, T. Wang, and B. Boulet, "Seamless dual brake transmission for electric vehicles: Design, control and experiment," *Mechanism and Machine Theory*, vol. 94, pp. 96 – 118, 2015.

[16] P. Walker, B. Zhu, and N. Zhang, "Powertrain dynamics and control of a two speed dual clutch transmission for electric vehicles," *Mechanical Systems and Signal Processing*, vol. 85, pp. 1–15, 2017.

[17] J. Liang, H. Yang, J. Wu, N. Zhang, and P. D. Walker, "Shifting and power sharing control of a novel dual input clutchless transmission for electric vehicles," *Mechanical Systems and Signal Processing*, vol. 104, pp. 725 – 743, 2018.

[18] J. Liang, H. Yang, J. Wu, N. Zhang, and P. Walker, "Power-on shifting in dual input clutchless power-shifting transmission for electric vehicles," *Mechanism and Machine Theory*, vol. 121, pp. 487 – 501, 2018.

[19] X. Zhou, P. Walker, N. Zhang, B. Zhu, and J. Ruan, "Numerical and experimental investigation of drag torque in a two-speed dual clutch transmission," *Mechanism and Machine Theory*, vol. 79, pp. 46–63, 2014.

[20] P. D. Walker, S. Abdul Rahman, B. Zhu, and N. Zhang, "Modelling, simulations, and optimisation of electric vehicles for analysis of transmission ratio selection," *Advances in Mechanical Engineering*, vol. 5, pp. 340 435–340 435, 2015.

[21] S. T. Razzacki, "Synchronizer design: A mathematical and dimensional treatise," in *SAE 2004 World Congress & Exhibition*. SAE International, Mar. 2004.

[22] L. Lovas, D. Play, J. Marialigeti, and J. F. Rigal, “Mechanical behaviour simulation for synchromesh mechanism improvements,” *Proceedings of the Institution of Mechanical Engineers, Part D: Journal of Automobile Engineering*, vol. 220, no. 7, pp. 919–945, 2006.

[23] W. Mo, P. D. Walker, and N. Zhang, “Dynamic analysis and control for an electric vehicle with harpoon-shift synchronizer,” *Mechanism and Machine Theory*, vol. 133, pp. 750–766, 2019.

[24] H. Naunheimer, B. Bertsche, J. Ryborz, and W. Novak, *Automotive transmissions: fundamentals, selection, design and application.* Springer Science & Business Media, 2010.

[25] Y. Shen, Z. Liu, and S. Rinderknecht, “Modelling of power losses of transmission synchronizers in neutral position,” in *WCX World Congress Experience.* SAE International, Apr. 2018.

[26] H. Yan, Z. Xu, J. Yuan, M. Liu, and W. Ge, “Friction coefficient compensation control in synchronizer synchronization process for transmission,” *Applied Sciences*, vol. 9, no. 15, p. 3096, 2019.

[27] H. V. Alizadeh, M. K. Helwa, and B. Boulet, “Constrained control of the synchromesh operating state in an electric vehicle’s clutchless automated manual transmission,” in *2014 IEEE Conference on Control Applications (CCA)*, Juan Les Antibes, France, Oct. 2014, pp. 623–628.

[28] M. Ehsani, Y. Gao, and A. Emadi, *Modern Electric, Hybrid Electric, and Fuel Cell Vehicles: Fundamentals, Theory, and Design, Second Edition*, ser. Power Electronics and Applications Series. CRC Press, 2017.

[29] A. Affanni, A. Bellini, G. Franceschini, P. Guglielmi, and C. Tassoni, “Battery choice and management for new-generation electric vehicles,” *IEEE Transactions on Industrial Electronics*, vol. 52, no. 5, pp. 1343–1349, Oct. 2005.

[30] A. Khaligh and Z. Li, “Battery, ultracapacitor, fuel cell, and hybrid energy storage systems for electric, hybrid electric, fuel cell, and plug-in hybrid electric vehicles: State of the art,” *IEEE Transactions on Vehicular Technology*, vol. 59, no. 6, pp. 2806–2814, July 2010.

[31] F. Vasca, L. Iannelli, A. Senatore, and M. T. Scafati, “Modeling torque transmissibility for automotive dry clutch engagement,” in *2008 American Control Conference*, June 2008, pp. 306–311.

[32] A. Serrarens, M. Dassen, and M. Steinbuch, “Simulation and control of an automotive dry clutch,” in *Proceedings of the 2004 American Control Conference*, vol. 5, June 2004, pp. 4078–4083 vol.5.

[33] Y. Dong, X. Jiao, and D. Chen, “Adaptive control for clutch engagement on starting up of vehicle,” in *Proceedings of the 10th World Congress on Intelligent Control and Automation*, July 2012, pp. 1230–1234.

[34] A. Senatore, D. Hochlenert, V. D’Agostino, and U. von Wagner, “Driveline Dynamics Simulation and Analysis of the Dry Clutch Friction-Induced Vibrations in the Eek Frequency Range,” ser. ASME International Mechanical Engineering Congress and Exposition, vol. Volume 13: Transportation Systems, 11 2013.

[35] F. Garofalo, L. Glielmo, L. Iannelli, and F. Vasca, “Smooth engagement for automotive dry clutch,” in *Proceedings of the 40th IEEE Conference on Decision and Control (Cat. No.01CH37228)*, vol. 1, Dec. 2001, pp. 529–534 vol.1.

[36] C. Yu, C. Tseng, and C. Wang, “Smooth gear-change control for EV clutchless automatic manual transmission,” in *2012 IEEE/ASME International Conference on Advanced Intelligent Mechatronics (AIM)*, July 2012, pp. 971–976.

[37] C. Yu, C. Tseng, and C. Wang, “Smooth gear-change control for ev clutchless automatic manual transmission,” in *2012 IEEE/ASME International Conference on Advanced Intelligent Mechatronics (AIM)*, July 2012, pp. 971–976.

[38] L. Glielmo, L. Iannelli, V. Vacca, and F. Vasca, “Gearshift control for automated manual transmissions,” *IEEE/ASME Transactions on Mechatronics*, vol. 11, no. 1, pp. 17–26, Feb. 2006.

[39] C.-H. Yu and C.-Y. Tseng, “Research on gear-change control technology for the clutchless automatic–manual transmission of an electric vehicle,” *Proceedings of the Institution of Mechanical Engineers, Part D: Journal of Automobile Engineering*, vol. 227, no. 10, pp. 1446–1458, 2013.

[40] V. Ivanović, J. Deur, Z. Herold, M. Hancock, and F. Assadian, “Modelling of electromechanically actuated active differential wet-clutch dynamics,” *Proceedings of the Institution of Mechanical Engineers, Part D: Journal of Automobile Engineering*, vol. 226, no. 4, pp. 433–456, 2012.

[41] J. Deur, J. Petric, J. Asgari, and D. Hrovat, “Modeling of wet clutch engagement including a thorough experimental validation,” in *SAE 2005 World Congress Exhibition*. SAE International, Apr. 2005.

[42] Liying Miao, Xiusheng Cheng, Xuesong Li, and Hanyu Jin, “Research on shift strategy for amt based on drag torque of wet clutch,” in *2017 3rd International Conference on Control, Automation and Robotics (ICCAR)*, April 2017, pp. 643–646.

[43] W. Yong-hai, "Multi-objective optimization design of vehicle clutch diaphragm spring," in *2009 Second International Conference on Intelligent Computation Technology and Automation*, vol. 3, Oct. 2009, pp. 194–197.

[44] N. Cappetti, M. Pisaturo, and A. Senatore, "Modelling the cushion spring characteristic to enhance the automated dry-clutch performance: The temperature effect," *Proceedings of the Institution of Mechanical Engineers, Part D: Journal of Automobile Engineering*, vol. 226, no. 11, pp. 1472–1482, 2012.

[45] M. Hoic, N. Kranjcevic, Z. Herold, J. Deur, and V. Ivanovic, "Experimental characterization and modeling of dry dual clutch wear," Apr. 2014.

[46] A. Della Gatta, L. Iannelli, M. Pisaturo, A. Senatore, and F. Vasca, "A survey on modeling and engagement control for automotive dry clutch," *Mechatronics*, vol. 55, pp. 63 – 75, 2018.

[47] J. Deur, V. Ivanović, Z. Herold, M. Kostelac, and H. E. Tseng, "Dry clutch control based on electromechanical actuator position feedback loop," *International journal of vehicle design*, vol. 60, no. 3/4, pp. 305–326, 2012.

[48] C. C. Bostwick and A. Szadkowski, "Self-excited vibrations during engagements of dry friction clutches," in *International Truck Bus Meeting Exposition*. SAE International, Nov. 1998.

[49] O. I. Abdullah and J. Schlattmann, "Contact analysis of a dry friction clutch system," *ISRN Mechanical Engineering*, vol. 2013, 2013.

[50] S. Ahn and S. Hong, "Clamping force control for dry-type dual clutch transmission using kissing point estimation," *SAE Int. J. Passeng. Cars - Mech. Syst.*, vol. 6, pp. 1505–1509, Oct. 2013.

[51] F. Vasca, L. Iannelli, A. Senatore, and G. Reale, “Torque transmissibility assessment for automotive dry-clutch engagement,” *IEEE/ASME Transactions on Mechatronics*, vol. 16, no. 3, pp. 564–573, June 2011.

[52] K. Han and Y. Yoon, “Clutch transmissible torque estimation for dry dual clutch transmission control,” in *Proceedings of the FISITA 2012 world automotive congress.* Springer, 2013, pp. 449–456.

[53] L. Li, X. Wang, X. Qi, X. Li, D. Cao, and Z. Zhu, “Automatic clutch control based on estimation of resistance torque for amt,” *IEEE/ASME Transactions on Mechatronics*, vol. 21, no. 6, pp. 2682–2693, Dec. 2016.

[54] G. Mattiazzo, S. Mauro, M. Velardocchia, F. Amisano, G. Serra, and G. Ercole, “Measurement of torque transmissibility in diaphragm spring clutch,” in *SAE 2002 World Congress Exhibition.* SAE International, Mar. 2002.

[55] T. Dutta and L. Baruah, “Engagement model of dry friction clutch with diaphragm spring,” *International Journal of Engineering Research*, vol. 3, no. 11, pp. 704–710, 2014.

[56] P. J. Dolcini, C. Canudas-de Wit, and H. Béchart, *Dry clutch control for automotive applications.* Springer Science & Business Media, 2010.

[57] E. Galvagno, M. Velardocchia, and A. Vigliani, “Analysis and simulation of a torque assist automated manual transmission,” *Mechanical Systems and Signal Processing*, vol. 25, no. 6, pp. 1877 – 1886, 2011.

[58] N. Cavina, D. Olivi, E. Corti, L. Poggio, and F. Marcigliano, “Development of a dual clutch transmission model for real-time applications,” in *IFAC Proceedings Volumes*, vol. 45, no. 30, 2012, pp. 440–447.

[59] Zongxuan Sun and K. Hebbale, "Challenges and opportunities in automotive transmission control," in *Proceedings of the 2005, American Control Conference, 2005*, vol. 5, June 2005, pp. 3284–3289.

[60] B. Mashadi, A. Kazemkhani, and R. B. Lakeh, "An automatic gear-shifting strategy for manual transmissions," in *Proceedings of the Institution of Mechanical Engineers, Part I: Journal of Systems and Control Engineering*, vol. 221, no. 5. SAGE Publications Sage UK: London, England, 2007, pp. 757–768.

[61] M. Kulkarni, T. Shim, and Y. Zhang, "Shift dynamics and control of dual-clutch transmissions," *Mechanism and Machine Theory*, vol. 42, no. 2, pp. 168 – 182, 2007.

[62] R. P. G. Heath and A. J. Child, "Zeroshift. a seamless automated manual transmission (AMT)with no torque interrupt," in *SAE World Congress Exhibition.* SAE International, Apr. 2007.

[63] K.-L. Kuo, "Simulation and analysis of the shift process for an automatic transmission," *World Academy of Science, Engineering and Technology*, vol. 52, pp. 341–347, 2011.

[64] Y. Zhang, Z. Zou, X. Chen, X. Zhang, and W. Tobler, "Simulation and analysis of transmission shift dynamics," *International Journal of Vehicle Design*, vol. 32, no. 3-4, pp. 273–289, 2003.

[65] C. H. F. Amendola and M. A. L. Alves, "Gear shift strategies analysis of the automatic transmission in comparison with the double clutch transmission," in *2006 SAE Brasil Congress and Exhibit.* SAE International, Nov. 2006.

[66] M. Bauer and O. Sawodny, "Modeling of a hybrid powertrain with a stepped automatic transmission," *IFAC-PapersOnLine*, vol. 51, no. 31, pp. 213 – 218, 2018.

[67] H.-S. Jo, W.-S. Lim, Y.-I. Park, and J.-M. Lee, “A study of the shifting transients of a torque converter equipped vehicle,” *International Journal of Heavy Vehicle Systems*, vol. 7, no. 4, pp. 264–280, 2000.

[68] P. Samanuhut and A. Dogan, “Dynamics equations of planetary gear sets for shift quality by lagrange method,” in *ASME 2008 Dynamic Systems and Control Conference.* American Society of Mechanical Engineers, 2008, pp. 353–360.

[69] Y. Wang, J. Song, and X. Li, “Simulation of amt autoshift process based on matlab/simulink/stateflow,” in *SAE 2004 Automotive Dynamics, Stability Controls Conference and Exhibition.* SAE International, May 2004.

[70] L. Li, K. He, X. Wang, and Y. Liu, “Sensor fault-tolerant control for gear-shifting engaging process of automated manual transmission,” *Mechanical Systems and Signal Processing*, vol. 99, pp. 790 – 804, 2018.

[71] Z. Zhong, G. Kong, Z. Yu, X. Xin, and X. Chen, “Shifting control of an automated mechanical transmission without using the clutch,” *International Journal of Automotive Technology*, vol. 13, no. 3, pp. 487 – 496, 2012.

[72] G. Lucente, M. Montanari, and C. Rossi, “Modelling of an automated manual transmission system,” *Mechatronics*, vol. 17, no. 2, pp. 73 – 91, 2007.

[73] A. Sorniotti, E. Galvagno, A. Morgando, M. Velardocchia, and F. Amisano, “An objective evaluation of the comfort during the gear change process,” *SAE Technical Paper 2007-01-1584*, 2007.

[74] X. Wang, L. Li, K. He, and C. Liu, “Dual-loop self-learning fuzzy control for AMT gear engagement: Design and experiment,” *IEEE Transactions on Fuzzy Systems*, vol. 26, no. 4, pp. 1813–1822, Aug. 2018.

[75] X. Wang, L. Li, K. He, Y. Liu, and C. Liu, "Position and force switching control for gear engagement of automated manual transmission gear-shift process," *Journal of Dynamic Systems, Measurement, and Control*, vol. 140, no. 8, p. 081010, 2018.

[76] H. Yue, C. Zhu, and B. Gao, "Fork-less two-speed I-AMT with overrunning clutch for light electric vehicle," *Mechanism and Machine Theory*, vol. 130, pp. 157 – 169, 2018.

[77] Y. Tian, J. Ruan, N. Zhang, J. Wu, and P. Walker, "Modelling and control of a novel two-speed transmission for electric vehicles," *Mechanism and Machine Theory*, vol. 127, pp. 13 – 32, 2018.

[78] M. Montanari, F. Ronchi, C. Rossi, A. Tilli, and A. Tonielli, "Control and performance evaluation of a clutch servo system with hydraulic actuation," *Control Engineering Practice*, vol. 12, no. 11, pp. 1369 – 1379, 2004.

[79] A. Myklebust and L. Eriksson, "Modeling, observability, and estimation of thermal effects and aging on transmitted torque in a heavy duty truck with a dry clutch," *IEEE/ASME Transactions on Mechatronics*, vol. 20, no. 1, pp. 61–72, Feb. 2015.

[80] A. C. V. D. Heijden, A. F. A. Serrarens, M. K. Camlibel, and H. Nijmeijer, "Hybrid optimal control of dry clutch engagement," *International Journal of Control*, vol. 80, no. 11, pp. 1717–1728, 2007.

[81] J. Horn, J. Bamberger, P. Michau, and S. Pindl, "Flatness-based clutch control for automated manual transmissions," *Control Engineering Practice*, vol. 11, no. 12, pp. 1353 – 1359, 2003.

[82] Q. Liang, N. Tang, B. Gao, and H. Chen, "The seamless gear shifting control for pure

electric vehicle with 2-speed Inverse-AMT," in *IFAC Proceedings Volumes*, vol. 46, no. 21, 2013, pp. 507–511.

[83] V. D'Agostino, N. Cappetti, M. Pisaturo, and A. Senatore, "Improving the Engagement Smoothness Through Multi-Variable Frictional Map in Automated Dry Clutch Control," ser. ASME 2012 International Mechanical Engineering Congress and Exposition, vol. Volume 11: Transportation Systems, 11 2012, pp. 9–19.

[84] M. Pisaturo and A. Senatore, "High order dynamic model and control strategy of automotive powertrain system with electro-hydraulic driven dry-clutch," *Hidraulica*, no. 1, pp. 7–18, 2015.

[85] S. Kim, J. Oh, and S. Choi, "Gear shift control of a dual-clutch transmission using optimal control allocation," *Mechanism and Machine Theory*, vol. 113, pp. 109 – 125, 2017.

[86] K. van Berkel, T. Hofman, A. Serrarens, and M. Steinbuch, "Fast and smooth clutch engagement control for dual-clutch transmissions," *Control Engineering Practice*, vol. 22, pp. 57 – 68, 2014.

[87] B. Matthes, "Dual clutch transmissions–lessons learned and future potential," *SAE transactions*, pp. 941–952, 2005.

[88] K. Hebbale, F. Samie, and J. Kish, "Dry dual clutch transmission (DCT) thermal model," in *SAE 2015 World Congress Exhibition*. SAE International, Apr. 2015.

[89] T. Deng, F. Hu, and R. Lu, "Research on DCT shifting torque control and a benchmark test," *Journal of Mechanical Science and Technology*, vol. 29, no. 9, pp. 3581–3589, 2015.

[90] Z. Zhao, L. He, Y. Yang, C. Wu, X. Li, and J. K. Hedrick, “Estimation of torque transmitted by clutch during shifting process for dry dual clutch transmission,” *Mechanical Systems and Signal Processing*, vol. 75, pp. 413 – 433, 2016.

[91] M. Goetz, M. C. Levesley, and D. A. Crolla, “Dynamics and control of gearshifts on twin-clutch transmissions,” *Proceedings of the Institution of Mechanical Engineers, Part D: Journal of Automobile Engineering*, vol. 219, no. 8, pp. 951–963, 2005.

[92] Wonoh Kim and G. Vachtsevanos, “Fuzzy logic ratio control for a cvt hydraulic module,” in *Proceedings of the 2000 IEEE International Symposium on Intelligent Control. Held jointly with the 8th IEEE Mediterranean Conference on Control and Automation (Cat. No.00CH37147)*, July 2000, pp. 151–156.

[93] P. Setlur, J. R. Wagner, D. M. Dawson, and B. Samuels, “Nonlinear control of a continuously variable transmission (CVT),” *IEEE Transactions on Control Systems Technology*, vol. 11, no. 1, pp. 101–108, Jan. 2003.

[94] K. Abo and M. Kobayashi, “Development of a New Metal Belt CVT for High Torque Engines,” in *SAE 2000 World Congress.* SAE International, Mar. 2000.

[95] M. A. Kluger and D. M. Long, “An overview of current automatic, manual and continuously variable transmission efficiencies and their projected future improvements,” in *International Congress Exposition.* SAE International, Mar. 1999.

[96] S. M. Felton, D. Lee, K. Cho, and R. J. Wood, “A passive, origami-inspired, continuously variable transmission,” in *2014 IEEE International Conference on Robotics and Automation (ICRA)*, May 2014, pp. 2913–2918.

[97] M. Adhitya, R. Mustafa, A. Plötner, and F. Küçükay, “A New Control Strategy of

Wet Dual Clutch Transmission (DCT) Clutch and Synchronizer for Seamless Gear Preselect," *SAE Int. J. Passeng. Cars - Mech. Syst.*, vol. 6, pp. 535–551, Apr. 2013.

[98] A. Sandooja, "Double indexing synchronizer - to amplify the synchronizer capacity," in *SAE 2012 Commercial Vehicle Engineering Congress*. SAE International, 2012.

[99] X. Xin and Z. Zhong, "The influence of parallel hybrid vehicle on synchronizer performance," in *2011 International Conference on Mechatronic Science, Electric Engineering and Computer (MEC)*. IEEE, 2011, pp. 721–724.

[100] A. Pingale, "Development of compact synchronizer technology for manual and automated transmissions," in *SAE 2014 World Congress Exhibition*. SAE International, Apr. 2014.

[101] X. Li, W. Zhang, J. Li, M. Jiang, and Y. Zhang, "Analysis on synchronizer of manual transmission using finite element analysis," SAE Technical Paper, Tech. Rep., 2015.

[102] H. Hoshino, "Analysis on synchronization mechanism of transmission," in *International Congress Exposition*. SAE International, Mar. 1999.

[103] H. V. Alizadeh, M. S. R. Mousavi, and B. Boulet, "Synchromesh torque estimation in an electric vehicle's clutchless automated manual transmission using unknown input observer," in *2015 IEEE Vehicle Power and Propulsion Conference (VPPC)*, Oct. 2015, pp. 1–5.

[104] A. Sandooja and R. Kunal, "Automotive synchronizer with asymetric toothing," in *SAE 2011 World Congress Exhibition*. SAE International, Apr. 2011.

[105] A. Blokhin, E. Denisenko, A. Kropp, and A. Nedialkov, "The study of the synchro-

nization process in the gearbox with automatic control," in *Applied Mechanics and Materials*, vol. 763. Trans Tech Publ, 2015, pp. 71–77.

[106] T. Lu, H. Li, J. Zhang, and H. Hao, "Supervisor control strategy of synchronizer for wet dct based on online estimation of clutch drag torque," *Mechanical Systems and Signal Processing*, vol. 66-67, pp. 840 – 861, 2016.

[107] G. Lanzerath and H. Patzer, "Synchronizer blocker ring with organic lining," in *SAE International Congress and Exposition.* SAE International, Mar. 1986.

[108] M. P. Singh, P. Singh, K. Kumar, and V. Rawla, "Development of test method to validate synchronizer ring design for torsional fluctuations in manual transmission," SAE Technical Paper, Tech. Rep., 2016.

[109] H. Chen and G. Tian, "Modeling and analysis of engaging process of automated mechanical transmissions," *Multibody System Dynamics*, vol. 37, no. 4, pp. 345–369, Aug. 2016.

[110] M. Irfan, V. Berbyuk, and H. Johansson, "Dynamics and pareto optimization of a generic synchronizer mechanism," in *Rotating Machinery, Hybrid Test Methods, Vibro-Acoustics & Laser Vibrometry, Volume 8.* Springer, 2016, pp. 417–425.

[111] X. Wanli, Z. Wei, S. Bin, and X. Ximeng, "Investigation of manual transmission synchronizer failure mechanism induced by interface material/lubricant combinations," *Wear*, vol. 328-329, pp. 475 – 479, 2015.

[112] A. Penta, R. Gaidhani, S. K. Sathiaseelan, and P. Warule, "Improvement in shift quality in a multi speed gearbox of an electric vehicle through synchronizer location optimization," in *WCX™ 17: SAE World Congress Experience.* SAE International, Mar. 2017.

[113] Y. V. Dhanal and Y. M. Jadhav, "Simulation of clutch inertial effects on gear shifting, synchronizer capacity and accelerated testing of synchronizers," in *8th SAEINDIA International Mobility Conference Exposition and Commercial Vehicle Engineering Congress 2013 (SIMCOMVEC).* SAE International, Nov. 2013.

[114] K. Barathiraja, G. Devaradjane, J. Paul, S. Rakesh, and G. Jamadade, "Analysis of automotive transmission gearbox synchronizer wear due to torsional vibration and the parameters influencing wear reduction," *Engineering Failure Analysis*, vol. 105, pp. 427 – 443, 2019.

[115] D. Häggström, P. Nyman, U. Sellgren, and S. Björklund, "Predicting friction in synchronizer systems," *Tribology International*, vol. 97, pp. 89 – 96, 2016.

[116] K. Parmee, "Challenges for transmission engineering (past and future)," in *1988 Conference and Exposition on Future Transportation Technology.* SAE International, Aug. 1988.

[117] T. Kinugasa, H. Ishii, H. Shozaki, and K. Takami, "Thermal analysis of the synchronizer friction surface and its application to the synchronizer durability improvement," *JSAE Review*, vol. 20, no. 2, pp. 217 – 222, 1999.

[118] H. Zhang, Z. Yu, Z. Zhong, B. Wu, and X. Chen, "Modelica based modeling of automotive transmission," in *2014 IEEE Conference and Expo Transportation Electrification Asia-Pacific (ITEC Asia-Pacific)*, Beijing, China, 2014, pp. 1–5.

[119] H.-L. Yu, J.-Q. Xi, F.-q. Zhang, and Y.-h. Hu, "Research on gear shifting process without disengaging clutch for a parallel hybrid electric vehicle equipped with AMT," *Mathematical Problems in Engineering*, vol. 2014, 2014.

[120] P. WALKER, N. ZHANG, R. TAMBA, and S. FITZGERALD, “Synchroniser modeling with application specific to the dual clutch transmission,” in *Asia Pacific Vibration Conference*, University of Canterbury, Christchurch, New Zealand, 2009, pp. 1–10.

[121] S. Lin, S. Chang, and B. Li, “Improving the gearshifts events in automated manual transmission by using an electromagnetic actuator,” in *Proceedings of the Institution of Mechanical Engineers, Part C: Journal of Mechanical Engineering Science*, vol. 229, no. 9, 2015, pp. 1548–1561.

[122] J. Li, F. Luo, Y. Luo, Y. Zhang, and M. Jiang, “Sensitivity analysis on a synchronization mechanism for manual transmission gearbox,” in *SAE Technical Paper*. Michigan, USA: SAE International, Apr. 2014.

[123] Y. Wang, E. Lü, H. Lu, N. Zhang, and X. Zhou, “Comprehensive design and optimization of an electric vehicle powertrain equipped with a two-speed dual-clutch transmission,” *Advances in Mechanical Engineering*, vol. 9, no. 1, pp. 1–13, 2017.

[124] W. Cao, Y. Wu, Y. Chang, Z. Liu, C. Lin, Q. Song, and A. Szumanowski, “Speed synchronization control for integrated automotive motor-transmission powertrains over can through a co-design methodology,” *IEEE Access*, vol. 6, pp. 14 106–14 117, 2018.

[125] X. Zhu, H. Zhang, J. Xi, J. Wang, and Z. Fang, “Optimal speed synchronization control for clutchless amt systems in electric vehicles with preview actions,” in *2014 American Control Conference*, June 2014, pp. 4611–4616.

[126] J.-q. Xi, G.-m. Xiong, and Y. Zhang, “Application of automatic manual transmis-

sion technology in pure electric bus," in *2008 IEEE Vehicle Power and Propulsion Conference*, Sep. 2008, pp. 1–4.

[127] A. Sorniotti, G. Loro Pilone, F. Viotto, S. Bertolotto, M. Everitt, R. Barnes, and I. Morrish, "A novel seamless 2-speed transmission system for electric vehicles: Principles and simulation results," *SAE International Journal of Engines*, vol. 4, no. 2, pp. 2671–2685, 2011.

[128] H.-D. Lee, S.-K. Sul, H.-S. Cho, and J.-M. Lee, "Advanced gear-shifting and clutching strategy for a parallel-hybrid vehicle," *IEEE Industry Applications Magazine*, vol. 6, no. 6, pp. 26–32, Nov. 2000.

[129] J. Wu, J. Liang, J. Ruan, N. Zhang, and P. D. Walker, "A robust energy management strategy for evs with dual input power-split transmission," *Mechanical Systems and Signal Processing*, vol. 111, pp. 442 – 455, 2018.

[130] C. H. Yu, C. Y. Tseng, and C. P. Wang, "Smooth gear-change control for EV clutchless automatic manual transmission," in *2012 IEEE/ASME International Conference on Advanced Intelligent Mechatronics (AIM)*, July 2012, pp. 971–976.

[131] F. Bottiglione, S. De Pinto, G. Mantriota, and A. Sorniotti, "Energy consumption of a battery electric vehicle with infinitely variable transmission," *Energies*, vol. 7, no. 12, pp. 8317–8337, 2014.

[132] L. Li, X. Wang, and J. Song, "Fuel consumption optimization for smart hybrid electric vehicle during a car-following process," *Mechanical Systems and Signal Processing*, vol. 87, pp. 17–29, 2017.

[133] B. Zhu, N. Zhang, P. Walker, W. Zhan, X. Zhou, and J. Ruan, "Two-speed DCT

electric powertrain shifting control and rig testing," *Advances in Mechanical Engineering*, vol. 5, p. 323917, 2015.

[134] X. Zhu, H. Zhang, J. Xi, J. Wang, and Z. Fang, "Robust speed synchronization control for clutchless automated manual transmission systems in electric vehicles," in *Proceedings of the Institution of Mechanical Engineers, Part D: Journal of Automobile Engineering*, vol. 229, no. 4, 2015, pp. 424–436.

[135] H. Kuroiwa, N. Ozaki, T. Okada, and M. Yamasaki, "Next-generation fuel-efficient automated manual transmission," *Hitachi Review*, vol. 53, pp. 205–209, 2004.

[136] H. V. Alizadeh and B. Boulet, "Robust control of synchromesh friction in an electric vehicle's clutchless automated manual transmission," in *2014 IEEE Conference on Control Applications (CCA)*, Juan Les Antibes, France, Oct. 2014, pp. 611–616.

[137] X. Xin and Z. Zhong, "The influence of parallel hybrid vehicle on synchronizer performance," in *2011 International Conference on Mechatronic Science, Electric Engineering and Computer (MEC)*, Aug. 2011, pp. 721–724.

[138] H. Yan, Z. Xu, J. Yuan, L. Liu, C. Tan, and W. Ge, "Friction characteristics of synchronization process based on tribo-thermodynamics," *Advances in Materials Science and Engineering*, vol. 2018, 2018.

[139] Y. Fang, N. Zhang, and P. D. Walker, "Harpoon-shift a new conception to implement gearshift in transmission," in *Proceedings of 2015 SAE-China Congress (Volume1)*, Shanghai, China, 2015.

[140] Y. Fang, N. Zhang, and L. Wang, "Insertion occlusion type gear shifting device and method," patent CN104 500 725B.

[141] “Bidirectional inserting and engaging type gear shifting device,” patent CN104 500 725B.

[142] Y. Fang, “A dual input and 3-speed transmission for electric vehicles,” Ph.D. dissertation, University of Technology Sydney, 2017.

[143] P. D. Walker and N. Zhang, “Engagement and control of synchroniser mechanisms in dual clutch transmissions,” *Mechanical Systems and Signal Processing*, vol. 26, pp. 320–332, 2012.

[144] S. T. Razzacki and J. E. Hottenstein, “Synchronizer design and development for dual clutch transmission (DCT),” in *SAE Technical Paper.* SAE International, Apr. 2007.

[145] X. Li, W. Zhang, J. Li, M. Jiang, and Y. Zhang, “Analysis on synchronizer of manual transmission using finite element analysis,” in *SAE 2015 World Congress Exhibition.* SAE International, Apr. 2015.

[146] T. Iwata, K. Mori, T. Maruyama, S. Nakamura, Y. Yoshida, and T. Yamanaka, “Development of the synchronizer-less system for hv-amt,” SAE Technical Paper, Tech. Rep., 2016.

[147] M. S. R. Mousavi, H. V. Alizadeh, and B. Boulet, “Estimation of synchromesh frictional torque and output torque in a clutchless automated manual transmission of a parallel hybrid electric vehicle,” *IEEE Transactions on Vehicular Technology*, vol. 66, no. 7, pp. 5531–5539, July 2017.

[148] J. Kim, D. Sung, C. Seok, H. Kim, H. Song, C. Lim, and J. Kim, “Development of shift feeling simulator for a manual transmission,” SAE Technical Paper, Tech. Rep., 2002.

[149] A. Kuchle, H. Naunheimer, B. Bertsche, J. Ryborz, W. Novak, and P. Fietkau, *Automotive Transmissions: Fundamentals, Selection, Design and Application.* Springer Berlin Heidelberg, 2010.

[150] P. D. Walker, Y. Fang, and N. Zhang, "Dynamics and control of clutchless automated manual transmissions for electric vehicles," *Journal of Vibration and Acoustics*, vol. 139, p. 061005, 2017.

[151] M. Bartram, G. Mavros, and S. Biggs, "A study on the effect of road friction on driveline vibrations," *Proceedings of the Institution of Mechanical Engineers, Part K: Journal of Multi-body Dynamics*, vol. 224, no. 4, pp. 321–340, Dec. 2010.

[152] J. Kim and S. B. Choi, "Control of dry clutch engagement for vehicle launches via a shaft torque observer," in *Proceedings of the 2010 American Control Conference*, June 2010, pp. 676–681.

[153] H. Naderpour, R. Barros, and S. Khatami, "A study of pounding to simulate impact and determine the impact damping ratio," in *Proceedings of the Fifteenth International Conference on Civil, Structural and Environmental Engineering Computing, Prague, Czech Republic.* Stirlingshire, Scotland: Civil-Comp Press, 2015.

[154] P. Flores and H. Lankarani, *Contact Force Models for Multibody Dynamics*, ser. Solid Mechanics and Its Applications. Springer International Publishing, 2016.

[155] X.-b. AN and S.-f. PAN, "Analysis of contact model in multi-body system dynamic simulation," *Computer Simulation*, vol. 25, 2008.

[156] ATi. (2017, May) ATi Industrial & Manufacturing Applications. [Online]. Available: https://www.atitelemetry.com/applications/industrial-manufacturing

[157] J. Ruan, "Design and verification of novel powertrain management for multi-geared battery electric vehicles," Ph.D. dissertation, University of Technology Sydney, May 2016.

[158] DSPACE. (2020, April) MicroAutoBox II. [Online]. Available: https://www.dspace.com/en/pub/home/products/hw/micautob/microautobox2.cfm

[159] M. Ieluzzi, P. Turco, and M. Montiglio, "Development of an heavy truck semi-active suspension control," *IFAC Proceedings Volumes*, vol. 37, no. 22, pp. 547 – 552, 2004.

[160] B. Fijalkowski, *Automotive Mechatronics: Operational and Practical Issues: Volume I*, ser. Intelligent Systems, Control and Automation: Science and Engineering. Springer Netherlands, 2010.

[161] S. Krishnan, "Gear shift quality benchmarking for manual transmissions," in *SAE Technical Paper*. The Automotive Research Association of India, Jan. 1999.

[162] X. Dong and J. Xi, "The study of shift strategy for pure electric bus without synchronizer," in *Proceedings of 2011 International Conference on Electronic Mechanical Engineering and Information Technology*, vol. 5, Aug. 2011, pp. 2557–2562.